SYNTHESIS OF NITROGEN-DOPED METAL OXIDES AND THEIR APPLICATION IN PHOTOCATALYTIC DEGRADATION OF DYES

BY

HANGGARA SUDRAJAT

A DISSERTATION SUBMITTED IN PARTIAL FULFILLMENT OF
THE REQUIREMENTS FOR THE DEGREE OF DOCTOR OF
PHILOSOPHY (ENGINEERING AND TECHNOLOGY)
SIRINDHORN INTERNATIONAL INSTITUTE OF TECHNOLOGY
THAMMASAT UNIVERSITY
ACADEMIC YEAR 2015

SYNTHESIS OF NITROGEN-DOPED METAL OXIDES AND THEIR APPLICATION IN PHOTOCATALYTIC DEGRADATION OF DYES

BY

HANGGARA SUDRAJAT

A DISSERTATION SUBMITTED IN PARTIAL FULFILLMENT OF
THE REQUIREMENTS FOR THE DEGREE OF DOCTOR OF
PHILOSOPHY (ENGINEERING AND TECHNOLOGY)
SIRINDHORN INTERNATIONAL INSTITUTE OF TECHNOLOGY
THAMMASAT UNIVERSITY
ACADEMIC YEAR 2015

SYNTHESIS OF NITROGEN-DOPED METAL OXIDES AND THEIR APPLICATION IN PHOTOCATALYTIC DEGRADATION OF DYES

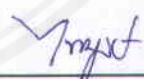A Dissertation Presented

By

HANGGARA SUDRAJAT

Submitted to

Sirindhorn International Institute of Technology

Thammasat University

In partial fulfillment of the requirements for the degree of

DOCTOR OF PHILOSOPHY (ENGINEERING AND TECHNOLOGY)

Approved as to style and content by

Advisor and Chairperson of Thesis Committee _____

(Assoc. Prof. Sandhya Babel, D. Tech. Sc.)

Co-Advisor _____

(Assoc. Prof. Alice Sharp, Ph.D.)

Committee Member and
Chairperson of Examination Committee _____

(Asst. Prof. Paiboon Sreearunothai, Ph.D.)

Committee Member _____

(Assoc. Prof. Nurak Grisdanurak, Ph.D.)

Committee Member _____

(Pongtanawat Khemthong, Ph.D.)

External Examiner: Prof. Hirofumi Hinode, Ph.D.

MAY 2016

1

Abstract

SYNTHESIS OF NITROGEN-DOPED METAL OXIDES AND THEIR APPLICATION IN PHOTOCATALYTIC DEGRADATION OF DYES

by

HANGGARA SUDRAJAT

B.S. in Chemistry, Universitas Gadjah Mada, 2008

M.E. in Chemical Engineering, Universitas Gadjah Mada, 2011

Photocatalysis with metal oxides, a clean, solar-driven process, is promising for the treatment of dye wastewater. However, most metal oxides show poor visible light activity, although some of them are able to absorb visible light. Therefore, their practical applications are limited. This study aims to develop a series of nitrogen-doped metal oxide catalysts namely N-ZnO, N-ZrO$_2$, and N-WO$_3$ with visible light activity and to investigate their photocatalytic activities for dye degradation in batch slurry system and continuous flow system. The catalysts are synthesized by mechanochemically assisted thermal decomposition method. Their properties are characterized using XRD, FTIR, TGA, SEM, TEM, DRS, XPS, XANES, BET, and zeta potentiometry. The results show that the primary particle size of the N-doped catalysts is around 50 nm with good crystallinity. N doping occurs in both interstitial and substitutional sites and significantly enhances the spectral response up to near-infrared (NIR) region. The N-doped catalysts show higher surface area and lower crystalline size compared to the pristine counterparts, and are stable upon irradiation. No significant reduction of the photocatalytic activity in repeated runs is observed. For the degradation of amaranth in batch slurry system, the order of photocatalytic activity is found to be N-WO$_3$ > N-ZnO > N-ZrO$_2$. The light source and the catalyst determine the reactive species produced during the dye degradation. Less oxidative species such as superoxide radical and singlet oxygen play a critical role in the rhodamine 6G degradation by N-ZnO and N-ZrO$_2$ under visible light, while hydroxyl

radicals are predominant under UV light. On the contrary, hydroxyl radicals and holes play a role in the degradation of amaranth by N-WO$_3$ under both visible and UV light. The photocatalytically treated solution of amaranth and that of methylene blue are nontoxic against *Bacillus cereus*, an important microorganism in agricultural soil.

To deal with the issue of catalyst particle separation and to improve their applicability in a real setting, two selected catalysts namely N-WO$_3$ and N-ZnO are immobilized on polyester fabric (PF), forming photoactive systems N-WO$_3$@PF and N-ZnO@PF, respectively. Their properties are characterized by XRD, ATR-FTIR, SEM, and DRS. The results show that the catalyst particles are evenly coated on the PF surface. Both N-WO$_3$@PF and N-ZnO@PF possess remarkable absorbance in the UV, visible, and NIR regions. The photoactive systems can be successfully used for the degradation of amaranth in a thin-film fixed-bed reactor (TFFBR) under solar, visible, and UV light. Under solar light, the photocatalytic activity of N-WO$_3$@PF is higher than that of N-ZnO@PF. After repeated runs, reduced photocatalytic activity is observed, likely due to decreased stability of the catalyst particles on the PF surface. On the basis of figures-of-merit recommended by IUPAC, N-WO$_3$@PF with a TFFBR shows a better performance compared to some existing solar photoactive systems, while N-ZnO@PF exhibits a comparable performance.

Keywords: photocatalysis, nitrogen doping, visible light active, mechanochemical synthesis, catalyst immobilization, dye degradation

Acknowledgements

Table of Contents

List of Figures

List of Tables

Chapter 1

Introduction

1.1 Overview

Dyes are widely employed in textile industry. During dyeing process, dyes can be released into the water bodies due to low process efficiency and improper treatment of effluents (Garcia et al., 2007). These lead to serious environmental problems and aesthetic issues. Because of their effectiveness for dye removal, coagulation, filtration, and adsorption with activated carbon are extensively used (Lee et al., 2006). However, they merely involve transfer the dyes from one phase to another. Biological treatment is a cost-effective method. But, majority of dyes are resistant to biological process (Behnajady et al., 2008). Therefore, finding effective, yet sustainable method for dye wastewater treatment is of important concern.

Semiconductor photocatalysis is a promising method since it offers clean, solar-driven process for dye wastewater treatment. Among semiconductor materials, metal oxides are the best choice due to their distinctive properties, high stability, and cost effectiveness. For degradation of organic compounds, the VB potential of metal oxide should be as low as possible to allow the generation of hole with strong oxidation power. Hole with strong oxidation power can effectively degrade the surface-adsorbed organic pollutant and is also able to make the oxidation of surface hydroxyl group or water into hydroxyl radical thermodynamically favorable. Therefore, the VB features of a metal oxide play a critical role.

Of the metal oxides, zinc oxide (ZnO), zirconium dioxide (ZrO_2), and tungsten trioxide (WO_3) seem promising for environmental photocatalysis due to their low VB potentials (Figure 1.1). However, ZnO and ZrO_2 only absorb UV light because of their large band gaps. On the other hand, WO_3 is not visible light active although it can absorb visible light. This is because of unsuitable CB potential of WO_3 for O_2 reduction, resulting in fast recombination of charge carriers. As a result, their practical applications in a real setting under solar light are limited.

Doping of metal oxides with N would be an effective strategy to extend the spectral responses of those metal oxides as the electronegativity of N is lower than that of O (Liu et al., 2010). Therefore, a new energy level within the band gap can be formed by N. During the doping process, additional energy levels may also be introduced because of the formation of structural defects (Wang et al., 2011a). These new energy levels allow multiple electron excitations leading to extended spectral response and can act as electron traps resulting in enhanced photocatalytic activity.
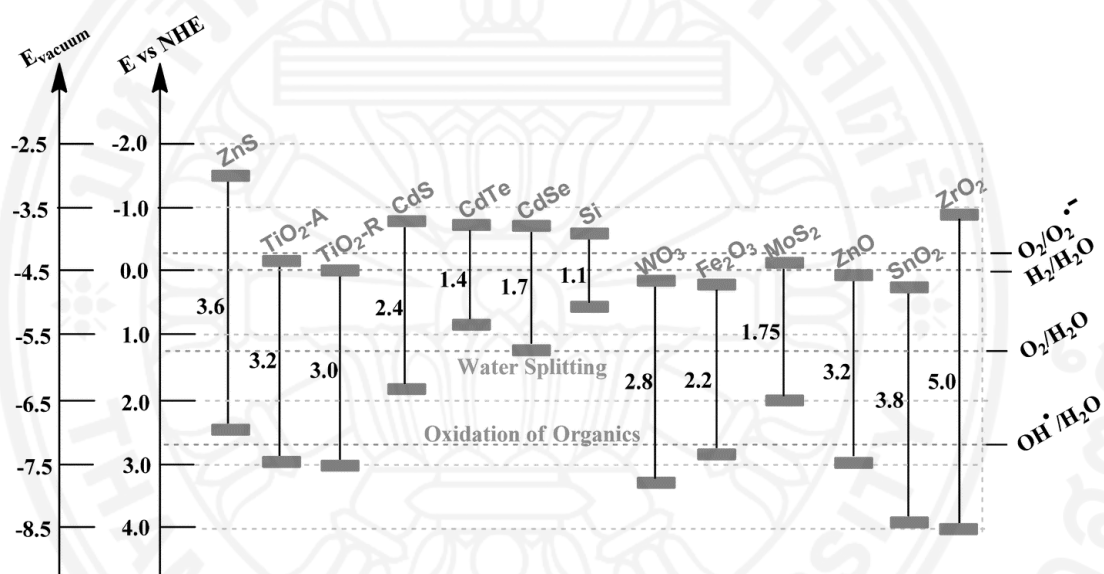
Figure 1.1 Band structures of some inorganic semiconductors (Wu et al., 2015).

For environmental photocatalysis, either pristine metal oxides or those which are doped with N are generally used in slurry system. Therefore, the catalyst particles must be separated from the system after use. Separation of the catalyst particles can be time-consuming for sedimentation and costly for filtration. More capital is required for the separation process. Light scattering by catalyst particles is also another challenge.

With the aim to avoid catalyst particle separation, immobilization of catalyst particles on stationary, solid surface can be adopted. One of the materials which shows promising potential for catalyst support is textile fabric. A variety of textile fabrics have been explored as catalyst supports due to their flexibility, relative

stability, and low-cost (Mejía et al., 2011; Mejia et al., 2009; Mejia et al., 2010; Rahal et al., 2011). Immobilization of catalyst particles on textile fabric is shown to be a good choice for overcoming the notorious problem of separating and recycling the catalyst particles in slurry system.

Among different types of fabrics, polyester fabrics appear suitable due to their strength, combined with their resistant to UV, chemicals, abrasion, stretching, shrinking, and wrinkling (Donelli et al., 2010). However, due to the hydrophobic nature of polyester fabrics and lack of surface functional groups, the stability of the immobilized catalyst particles is relatively low (Hashemizad et al., 2012). To increase hydrophilicity of fabric surface, simple pretreatment with alkali has been shown to be promising (Donelli et al., 2010; Haghighatkish & Yousefi, 1992; Zeronian & Collins, 1989). The alkali treatment can change the chemical, physical, and morphological properties of the fabric by increasing the amount of surface functional groups, improving the accessibility of functional groups on the newly exposed surfaces, and increasing roughness and porosity of the surface, respectively (Donelli et al., 2010). Due to increased hydrophilicity of the surface, more catalyst can be coated through bonding with the functional groups on the fabric surface. Moreover, fabric treatment with UVC light has also been reported to induce the formation of chelating agents to bind the catalyst particles on the fabric surface (Mejia et al., 2009; Yuranova et al., 2007). As a result, high stability of the catalyst particles on the surface can be obtained.

Summing up, photocatalysis with metal oxide catalysts has shown pronounced potential for the treatment of dye wastewater. Nonetheless, the photocatalytic processes have encountered some limitations, including inactivity of the catalyst under visible light and separation of catalyst particles. To overcome these two major limitations, in this research, metal oxide catalysts, namely, ZnO, ZrO_2, and WO_3, are made visible light active by doping with N. The N doping is achieved through a solid state process with mechanochemically assisted thermal decomposition of urea-metal precursor complexes. This simple protocol involves mild reaction condition with no reagent concentration limitation, enabling high synthesis yield. Also, special and costly equipment, complicated reaction controls, and stringent reaction conditions are not required. The photocatalytic activity of N-doped ZnO (N-ZnO), N-doped ZrO_2

(N-ZrO$_2$), and N-doped WO$_3$ (N-WO$_3$) are evaluated for the degradation of three commonly used dyes, methylene blue (MB), amaranth (AM), and rhodamine 6G (R6G). To deal with the problem of catalyst particle separation, the selected catalysts are immobilized on polyester fabric (PF). Their performances are evaluated for the degradation of AM in a thin-film fixed-bed reactor (TFFBR).

1.2 Objectives

- To synthesize a series of nitrogen-doped metal oxides namely N-ZnO, N-ZrO$_2$, and N-WO$_3$ with visible light activity for degradation of dyes in batch slurry system.
- To immobilize N-WO$_3$ and N-ZnO on polyester fabric forming two photoactive systems N-WO$_3$@PF and N-ZnO@PF for degradation of AM in continuous flow system.

1.3 Scope and limitations

- The N-doped metal oxides were synthesized through mechanochemically assisted thermal decomposition of urea-metal precursor complexes.
- Urea was used as N source for the synthesis of N-doped metal oxides since it is an inexpensive raw material which is widely available and easy to handle.
- The molar ratio of urea/metal precursor (U/Z) is varied (0.25, 0.5, 1 and 2). Only N-ZnO, N-ZrO$_2$, and N-WO$_3$ with U/Z of 2 were characterized and studied further since they generally showed the highest photocatalytic activities.
- In batch slurry system using N-ZnO and N-ZrO$_2$, role of reactive species was only studied for the degradation of R6G.
- The toxicity assessment was only carried out for MB and AM solution treated with N-ZnO and N-ZrO$_2$ under visible light at selected experimental conditions in batch slurry system.
- Only N-ZnO and N-WO$_3$ were immobilized on polyester fabric since they exhibited appreciable photocatalytic activities for the dye degradation in batch slurry system.
- Immobilization of the catalyst particles on polyester fabric was done through heat

attachment method.

- Only AM was used for the photocatalytic activity evaluation of immobilized catalysts since it is the most difficult dye to degrade based on the experiments in batch slurry system.

- Visible and UVA light were only used in some experiments of the AM degradation by N-WO$_3$@PF for comparison.

Chapter 2
Literature Review

2.1 Sources of dye wastewater and its effects on the environment

Textile industry shows significant impact on environmental quality because its operation generates a significant amount of dye wastewater as a result inefficient dyeing process (Robinson et al., 2001). Taking the volume generated and the effluent composition into account, dye wastewater produced from textile industry can be regarded as the most polluting wasewaters. Table 2.1 presents common dyes employed in textile industry.

Table 2.1 Class of dyes used for dyeing (Kim, 2006).

Class	Substrates	Characteristics	Chemical types
Acid	Nylon, wool, silk, paper, and leather	Water-soluble anionic compounds	Azo, anthraquinone, tryphenylmethane
Basic	Paper, polyacrylonitrile, Polyester, and inks	Water-soluble, applied in weakly acidic dyebaths, very bright dyes	Azo, cyanine, hemicyanine, diazahemicyanine, azine, xanthene, oxazine, and anthraquinone
Reactive	Cotton, wool, silk, and nylon	Water-soluble, anionic compounds, largest dye class	Azo and anthraquinone, phthalocyanine, formazan
Direct	Cotton, rayon, paper, leather, and nylon	Water-soluble and anionic compounds	Azo, phthalocyanine, stilbene, and oxazine
Sulfur	Cotton and rayon	Organic compounds containing sulfur	Indeterminate structures
Vat	Cotton, rayon and wool	Water-insoluble, oldest dyes, more chemically complex	Anthraquinone and indigoids

The nature of dye wastewater generated is dependent mainly on the fiber and chemical substances employed. Textile production also involves various types of chemicals other than dyes, such as solubilizing agents, buffer system, electrolyte, and auxiliary chemicals including retarder, levelling agent, defoamer, surfactant, and lubricant (Ren, 2000). Such chemicals are likely present in the dye wastewater. Moreover, many dyes can pass through conventional treatment unaffected due to their high stability to chemicals, thermal, and light. They can also resist to biodegradation.

Dye wastewater leads to serious environment problems, mainly due to two factors. First, dye wastewater is characterized by strong color which can interrupt the

sunlight transmission in water body. This hampers photosynthesis of aquatic organisms due to oxygen deficiency and ultimately affects the food chain. Considering the public perception about water quality, this aesthetic aspect of dye wastewater is also a pivotal concern due to that water quality is influenced by the color of water. Therefore, color removal often attracts more attention than the removal of other organic compounds which are soluble and colorless. Secondly, several classes of dyes and their oxidation and reduction products are known to be toxic, carcinogenic, and mutagenic. To give an instance, acid red 21 is an azo dye which features azo group. In the presence of reducing or oxidizing agent, the azo group can be cleaved, leading to the formation of some aromatic compounds (Figure 2.1) (Kim, 2006).
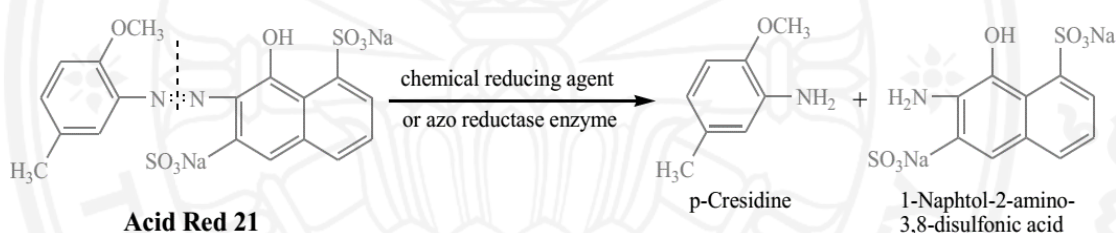
Figure 2.1 Reductive cleavage of Acid Red 21 (Kim, 2006).

2.2 Methods for dye removal

Taking into account the effects of dye wastewater on the environment, finding feasible treatment methods for dye wastewater is pivotal and technological interest. Up until now, various approaches for dye removal have been studied, such as adsorption, coagulation, oxidation processes, and biological processes. These methods are usually effective for dye wastewater. Some findings on the utilization of such methods in laboratory scale are discussed briefly in this section.

2.2.1 Adsorption

Aqueous phase adsorption seems to be the most common technique for dye removal in wastewater. Of many available adsorbents, activated carbon is very popular for wastewater treatment in industrial scale. However, commercial activated carbon is

expensive for medium and small scale industries. This fact triggers the development of low-cost adsorbents from waste-based materials.

Leaves powder of *Azadirachta indica* was evaluated to remove congo red (CR) (Bhattacharyya & Sharma, 2004). At an optimum operating condition, up to 99% removal was attained. In other researches, by using Jujuba seeds, only 40% of CR removal was obtained at pH 12 (Reddy et al., 2012), while 78.12% removal was reached at pH 9.2 by applying pine cone powder as adsorbent (Dawood & Sen, 2012).

The major drawback of such low-cost adsorbents is a high variability in their characteristics, leading to a low reproducibility of the adsorption efficiency. Due to this fact, many researchers have developed various synthetic compounds such as macrocyclic molecules as adsorbent. For instance, carbon nanomaterials such as nanodiamond particles (NDs) and carbon nanotube (CNT) have also been used as adsorbents for aqueous pollutant sequestration. In particular, NDs have high specific surface area and oxygen-containing surface functional groups which are desirable for adsorption applications. The efficacy of nanodiamond to adsorb acid orange 7 was tested. At 30 μM of dye concentration, 98% dye removal was achieved (Wang et al., 2012).

Porous metal oxides have also been explored for dye removal. An excellent work was conducted to evaluate the ability of novel mesoporous MgO nanostructures for removal of congo red (CR) (Li et al., 2012). They showed a satisfactory adsorptive property to CR. The removal of CR rapidly reaches ∼100% at 2 min, when MgO sample (0.064 M AOT) was applied as an adsorbent.

2.2.2 Filtration

Ultrafiltration is the foremost membrane filtration method applied for dye removal. A ceramic membrane was performed to remove reactive black 5 (RB5) (Alventosa-deLara et al., 2012). Results exhibited a significant dye removal with rejection coefficients of 79.8%. The performances of nanofiltration (NF) and reverse osmosis (RO) were compared to remove methyl orange (MO) (Nataraj et al., 2009). The rejection of MO using RO was very high (99.99%) compared to that using NF (90%). It was indicated that nanofiltration and reverse osmosis are exceptionally effective in

dye removal. But, it should be noted that due to very small pores, clogging on RO membrane is likely to occur.

Moreover, UF and NF processes were also evaluated for treatment of aqueous solutions containing various dyes (Aouni et al., 2012). Two nanofiltration membranes (NF 200 and NF 270) and two ultrafiltration membranes (10 kDa and 1 kDa) were tested. Color retention of more than 90% was reached for both NF 200 and NF 270. UF of 1 kDa membrane can also give color retention of around 80%.

2.2.3 Coagulation and flocculation

Removal of dyes from wastewater using a coagulating/flocculating agent is found to be effective. It involves addition of alum, ferric sulfate, lime, and synthetic organic polymers. Natural coagulants, mainly polysaccharides, are environmentally friendly compare to inorganic coagulants.

$FeCl_3$ was used to remove reactive yellow from aqueous solution (Karadag et al., 2006). About 99.67% removal of dye was attained at pH 3.5 and coagulant dose of 0.4 g/L.

A study dealing with utilization of a lignin-base cationic polyelectrolyte (L-DAF) for dye removal was also conducted (Fang et al., 2010). At an optimum dose of flocculant (initial concentration of 100 mg/L, pH of 6.5 and 24 h operation), dye removal efficiency of 97.1, 98.3 and 99.5% can be obtained for acid black, reactive red, and direct red, respectively.

2.2.4 Oxidation using oxidizing agents

Nowadays, many industries involving dyeing operations such as textile industry have also adopted chemical oxidation techniques. Ozonation was used to remove reactive black 5 from aqueous solution in a semi-batch reactor (Wu & Wang, 2001). After 30 min of ozonation, gas flow rate of 0.52 L/min, and gas pressure of 82.73 kPa, a degradation efficiency of 87% was obtained. Ozonation of orange II and acid red 27 was also studied in a bubble column reactor (Silva et al., 2009). More than 98% dyes were removed in 30 min for both cases.

Hydrogen peroxide (H_2O_2) coupled with UV irradiation can also be a good option for dye degradation. A combination of UV radiation and H_2O_2 was evaluated

for acid black 1 degradation (Shu et al., 2004). At an optimum operating condition, 100% dye removal was attained in less than 2 min.

Furthermore, a chemical chlorination process for degradation of disperse blue 291 was assessed (de Oliveira et al., 2012). After 2 h, a dye removal efficiency of 60% was reached. It was indicated that chlorination is not an effective process for complete dye removal and can also form hazardous by-products.

2.2.5 Electrochemical method

Electrochemical method has also been employed for dye wastewater treatment. Both soluble and insoluble dyes are able to be degraded electrochemically. Several findings on use of electrochemical method for dye removal have been reported.

The electrochemical treatment of reactofix red 3 from aqueous solution using an iron cell was undertaken (Gupta et al., 2007). The electrode process was found to be irreversible. It was showed that electrochemical reduction followed first-order kinetics with dye removal efficiency of 90%.

Acid red 29 was degraded by chlorine (Oliveira et al., 2007). The chlorine generator was from $Ti/Sn_{(1-x)}Ir_xO_2$ electrodes. The best conditions for 100% removal were found to be at pH 4 of NaCl, 25 mA/cm^2, and 6 h of electrolysis.

The treatment of disperse blue 106 was carried out by performing continuous electrocoagulation process (Kim et al., 2002). The dye removal was mainly affected by dye concentration and initial pH, which is favored at high pH and high dye concentration. At optimum experimental conditions, 98% dye removal was achieved.

2.2.6 Ultrasound

Ultrasound is able to break down the organic pollutants due to generation of free radicals. Nevertheless, this method does not get much attention, probably due to that ultrasound is energy consuming. Some research findings also showed that dye removal efficiency with ultrasound is low.

Mineralization of reactive black 5 (RB5) was investigated using ultrasonic irradiation (Vajnhandl & Le Marechal, 2007). Result showed that 70% removal was achieved after 1 h irradiation at pH of 2 and 20 mg/L of dye. Dye removal efficiency with ultrasound for RB5 was evaluated (Tauber et al., 2008). Up to 80% removal was

obtained after 3.5 h at 850 kHz, deposited power of 4.1 W/cm^2, and 30 ºC in continuous operation mode.

Efficacy of ultrasound for degradation of direct yellow 9 (DY9) and reactive red 141 (RR141) was also studied (Tauber et al., 2008). After 30 min sonication of 28.75 μM dyes at frequency of 577 kHz and deposited power of 48.9 W, removal efficiencies of 22.58% (DY9) and 45.92% (RR141) were achieved. A similar finding on dye degradation with ultrasound irradiation was also reported. Results showed that only 35% removal of acid orange 7 was attained after 9 h (Ma et al., 2006).

2.2.7 Biological method

Biological method is economically feasible. Fungal decolorization, bioaccumulation, and bioremediation are normally applied for decontamination of industrial wastewater since many microorganisms can accumulate and degrade different types of pollutants. Two microorganism groups commonly utilized for dye wastewater treatment are bacteria and fungi (Ahmed et al., 2007; Kaushik & Malik, 2009). A number of dyes were effectively degraded by the strain *Kurthia* sp. with 92 to 100% removal (Sani & Banerjee, 1999). Pararosaniline was completely decolorized in 53 min due to possessing the simplest structure. Fungal strains capable of degrading various dyes have also been studied by many researchers.

In aerobic conditions, dye can also be degraded with the help of bacterial enzymes (Ahmed et al., 2007). Since the initial rate depends linearly on the enzyme concentration, some researchers have tried to employ the purified enzyme directly for dye removal. For example, a purified manganese peroxidase enzyme from *Trametes versicolor* was used to degrade amaranth (Champagne & Ramsay, 2010). Dye removal efficiency of 100% was achieved within less than 1 h. Laccase purified from the same fungus also effectively degrades amaranth.

11

2.2.8 Comparison of methods

A careful consideration in evaluating the method effectiveness for dye removal is required since method comparison is difficult to perform. Several comparative studies on the removal of dyes with a relatively similar operating condition have been undertaken. This allows an easy comparison.

A comparative study dealing with utilization of three different AOPs for degradation of acid blue 74 (AB74) in aqueous solution was also undertaken (Kasiri et al., 2008). $UV/Fe-ZSM5/H_2O_2$ showed appreciable performance for dye degradation, compared to UV/H_2O_2 and $Fe-ZSM5/H_2O_2$. It was thought that UV radiation can elevate the formation of •OH by photolysis of H_2O_2.

Some researchers commented that membrane filtration technologies have weaknesses of high energy consumption and cost which must be taken into account for large-scale applications (Aouni et al., 2012; Le-Clech et al., 2006). Others consider that membrane filtrations are preferred for dye removal due to that they can produce small disposal volumes; hence minimizing waste disposal costs and only requiring a small foot print for equipment (Cheryan & Rajagopalan, 1998; Robinson et al., 2001; Van der Bruggen et al., 2004). Thus, the preference for choosing a suitable method for dye removal is ultimately dependent on many aspects and different point of views. It can be high cost competitiveness, easy operation, or fast treatment process.

Suitable method for dye removal is ideally a method which can degrade the dye without generating either any harmful substance or any secondary pollutant which will involve complicated procedure. Adsorption, membrane filtration, and coagulation/flocculation are very effective for dye removal. Nonetheless, these methods are basically incapable of degrading the dye (non-destructive process). There is no alteration into their less harmful form. Although by using lignocellulosic-based adsorbents, this issue is resolved, yet additional cost for further treatment is required.

In order to degrade the dye, biological method can be used. Nevertheless, for biological method, sensitivity toward variation of influent characteristics and some toxic chemicals present become the major problems hampering its effective performance. Although several kinds of dyes are degraded, many others are recalcitrant to biodegradation because of their complex molecular structures. For

instance, ponceau 4R, which is considered carcinogenic, is not totally degraded by biological process (Rieger et al., 2002). Due to their stability and xenobiotic nature, acid and reactive azo dyes are also not totally degraded by conventional biological treatments (Azbar et al., 2004). Moreover, at high dye concentrations, reactive dyes with sulfonic acid groups inhibited the growth of microorganisms to a great extent.

Beside biological process, AOPs can also be used for dye removal, which are considered to be more effective than biological process. Fenton process is relatively inexpensive for dye removal. The UV/H_2O_2 process is considered to be the most effective AOP due to its capability of complete dye removal with lack of sludge generation (Attar & Rezaee, 2006). However, it is less effective for high concentration of dispersed and fat dyes. Inefficient use of UV light also adds to its operating cost. Ultrasound can also be used. Nevertheless, ultrasonication of dyes leads to the formation of nitro and nitroso aromatics, which are toxic and carcinogenic (Joseph et al., 2000). By performing electrochemical oxidation, harmful by-products are less likely to form (Oliveira et al., 2007). But, electricity requirement impedes its cost competitiveness and applicability.

2.3 Dye degradation by metal oxide photocatalysts

Heterogeneous photocatalysis with metal oxide catalysts is a promising method for dye degradation offering complete mineralization of the dyes into harmless compounds (Wu et al., 2011). During photocatalytic process, dye molecules are degraded and eventually mineralized. A series of photocatalytic reactions on catalyst surface is illustrated in Figure 2.2. It is initiated by photon absorption (step 1). This leads to a charge separation due to excitation of an electron (e^-_{cb}) from the VB to the CB, leaving a hole or an electron vacancy (h^+_{vb}) in the VB. Both h^+_{vb} and e^-_{cb} can move to the catalyst surface and enter a redox reaction on the catalyst surface. Hydroxyl radical (•OH) is generated when h^+_{vb} reacts with H_2O (step 2), while superoxide radical (•O_2^-) is produced by reaction of e^-_{cb} with O_2 (step 3). Protonation of •O_2^- results in hydroperoxyl radical, •OOH (step 4). Further, h^+_{vb} can also oxidize dye molecule directly to form positively charged dye (dye$^+$) (step 5), while e^-_{cb} can reduce dye molecule to create negatively charged dye (dye$^-$) (step 6). The

photogenerated charge carriers (h^+_{vb} and e^-_{cb}) will not recombine immediately if electron scavengers are present. The possible chain reactions are listed in Table 2.2.
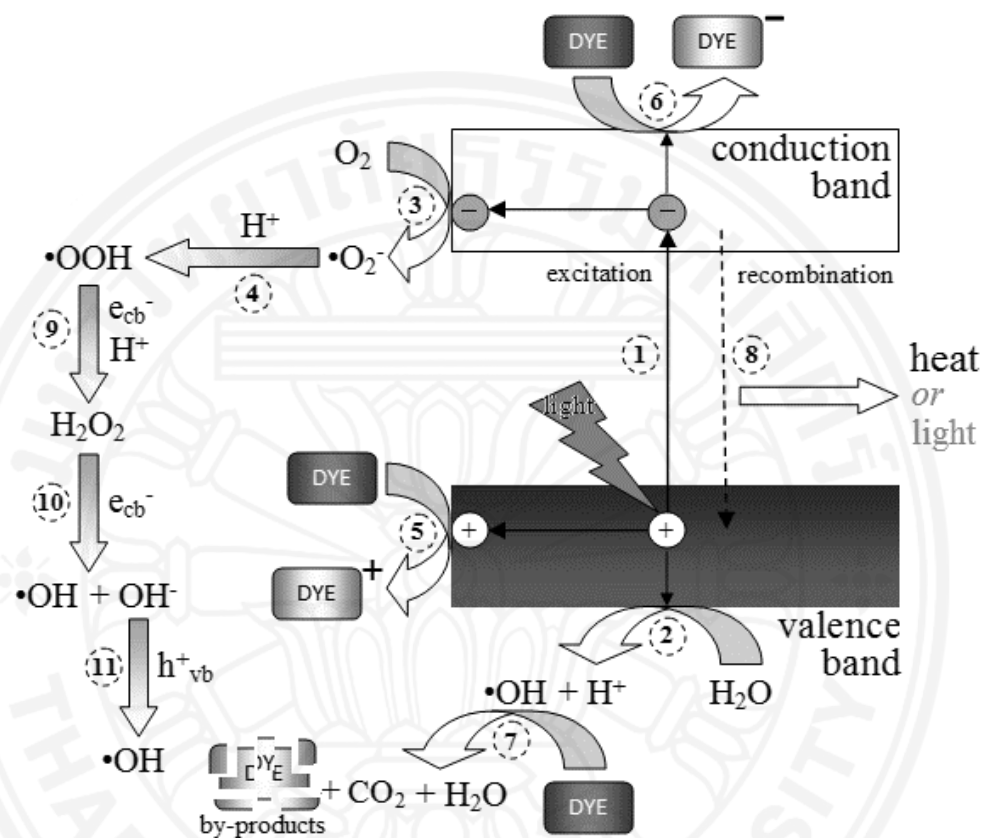
Figure 2.2 Heterogeneous photocatalytic reactions for dye degradation in aqueous suspension: (1) photocatalyst excitation; (2) oxidation of water; (3) reduction of O_2; (4) protonation of $\cdot O_2^-$; (5) dye oxidation; (6) dye reduction; (7) dye degradation by $\cdot OH$; (8) h^+_{vb}-e^-_{cb} recombination; (9) formation of H_2O_2; (10) reduction of H_2O_2; (11) oxidation of OH^-.

Table 2.2 Possible reactions in heterogeneous photocatalysis of dye.

Reaction process	Reaction equation
Photocatalyst excitation	photocatalyst + $hv \rightarrow e^-_{cb} + h^+_{vb}$
Electron-hole recombination	$e^-_{tp} + h^+_{vb}/h^+_{tp} \rightarrow e^-_{cb}$ + heat/light
Reduction of O_2	$O_2 + e^-_{cb} \rightarrow \bullet O_2^-$
Oxidation of H_2O	$H_2O + h^+_{vb} \rightarrow \bullet OH$
Reduction of H_2O_2	$H_2O_2 + e^-_{cb} \rightarrow \bullet OH + OH^-$
Oxidation of OH^-	$OH^- + h^+_{vb} \rightarrow \bullet OH$
Protonation of $\bullet O_2^-$	$\bullet O_2^- + H^+ \rightarrow \bullet OOH$
Formation of H_2O_2	$\bullet OOH + e^-_{cb} + H^+ \rightarrow H_2O_2$
Dye degradation by $\bullet OH$	dye + $\bullet OH \rightarrow \bullet$dye + $H_2O \rightarrow$ dye degradation products + $CO_2 + H_2O$
Dye oxidation by h^+_{vb}	dye + $h^+_{vb} \rightarrow$ dye$^+$
Dye reduction by e^-_{cb}	dye + $e^-_{cb} \rightarrow$ dye$^-$

Without electron acceptor or electron donor, the photogenerated charge carriers may recombine and reduce overall quantum efficiency of photocatalytic process. Recombination occurs when the excited electron turns to the VB dissipating the energy as heat or light (Figure 2.3). To prevent charge carriers from recombination, catalyst modifications by a variety of approaches can be employed.
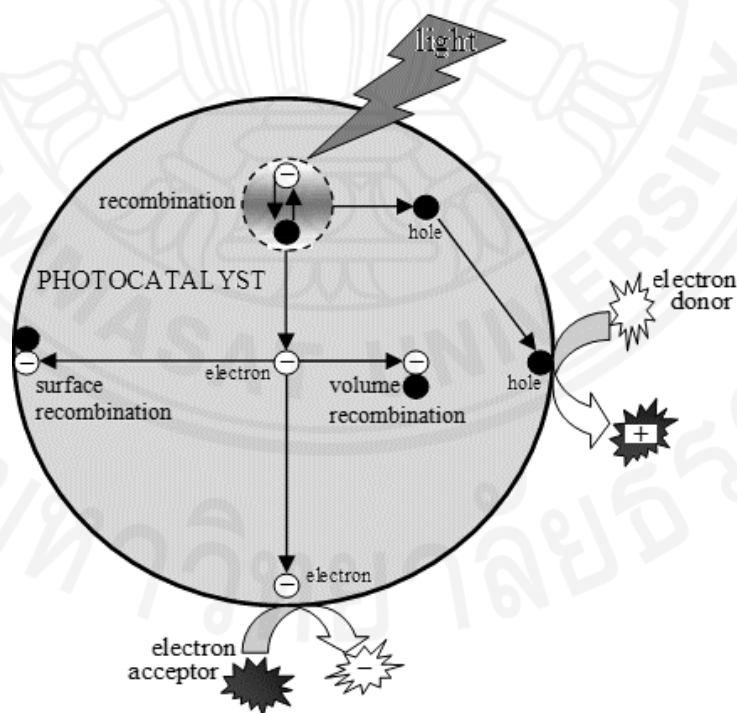
Figure 2.3 Recombination of photogenerated charge carriers.

2.4 Photocatalytic activity improvement

To improve catalyst performance, especially under visible light, different strategies have been employed. The main goals are (i) to narrow the band gap or to introduce a new energy level below the CB or above the VB; thus light with lower energy can be harvested, and (ii) to prolong separation of charge carriers; hence delaying their recombination.

2.4.1 Doping with metal or nonmetal

Catalyst doping by either metal or nonmetal elements has been proven effective to narrow bad gap or to introduce new energy level within the band gap (Figure 2.4). After doping, spectral response of the catalyst is extended to longer wavelength. The extended spectral response usually results in increased photocatalytic activity. Some dopants can also trap photogenerated electron. Thus, electron-hole recombination can be suppressed and the photocatalytic activity of the catalyst is enhanced. Several studies have confirmed effectiveness of catalyst doping in improving photocatalytic activity.

Degradation of acid orange 7 (AO7) was done by employing TiO_2 doped with different amount of Ce (Jaimes-Ramírez et al., 2012). Dye degradation increased as the Ce content increased up to 1% at pH 7. The 1%Ce-TiO_2 can degrade 86% of dye after 3 h, while 3%Ce-TiO_2 was only capable of attaining 59% degradation efficiency. With increasing the amount of Ce, reduced photocatalytic activity is observed.
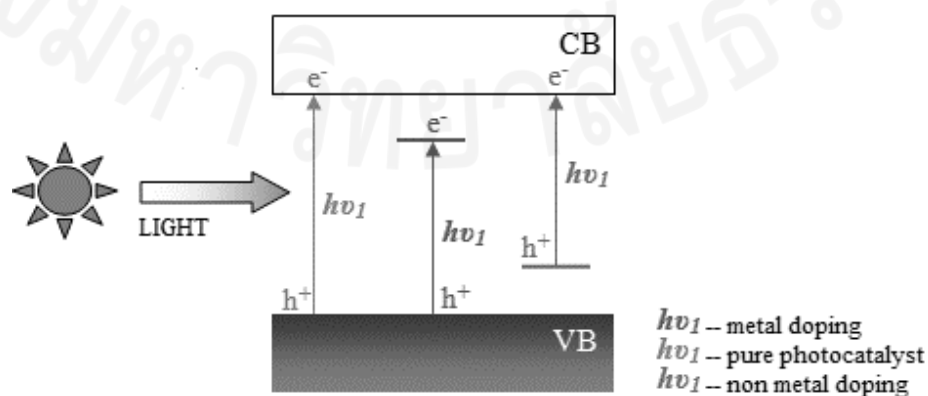
Figure 2.4 Doping effects on the band gap structure.

For degradation of basic green 4, some novel TiO_2 doped with alkaline metals, namely Li, Na and K, were performed (Bessekhouad et al., 2004). It was found that 5%Li-TiO_2 prepared by impregnation method was the best catalyst. The efficiency of the catalyst prepared by impregnation method is better than that of TiO_2.

2.4.2 Catalyst coupling

Coupled catalysts, such as $SiO_2/NiFe_2O_4$, $SnO_2/CdSe$, $TiO_2/ZnFe_2O_4$ and CdS/TiO_2, may exhibit enhanced photocatalytic activity due to decreased recombination rate and prolonged charge separation. A synergistic effect is usually observed. During irradiation of a coupled catalyst, transfer of electron and hole takes place, leading to electron-hole separation (Figure 2.5). The higher the difference of CB and VB potential between two catalysts, the more favorable thermodynamically the transfer of electron and hole. For coupled catalyst, the critical factors are the suitability of band structures between two catalysts, the contact between two different catalyst phases, and the atomic structures in the catalyst interfaces. Also, it is pivotal noting that the redox potential of the transferred charge carriers is lowered after charge carrier transfer. Thus, the reduction power of electron and the oxidation power of hole are reduced.
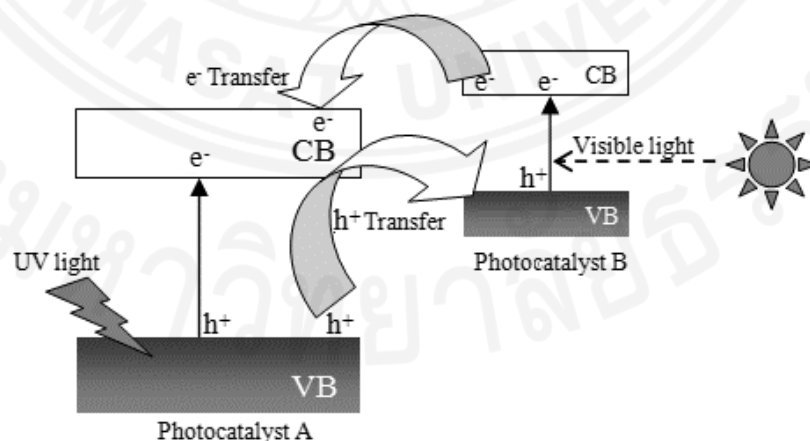
Figure 2.5 Electron and hole transfer in coupled catalyst.

In a research work, ZnO/SnO_2 composite was tested for degradation of basic blue 9 (Lin & Chiang, 2012). For comparison, ZnO and SnO_2 were also employed. It

was indicated that ZnO/SnO_2 showed a much greater photocatalytic activity than either pure ZnO or SnO_2. The efficiency for degrading 30 mg/L of dye using ZnO/SnO_2 was found to be almost 100% in 120 min. It is proposed that ZnO/SnO_2 can reduce recombination rate, resulting in increased photocatalytic activity.

2.4.3 Metal deposition

Metals can be deposited on catalyst surface to trap the photoproduced electrons. This will prevent electrons from recombination with holes; therefore promoting interfacial charge transfer (Figure 2.6). The performance of Au/TiO_2 thin films for methyl orange (MO) degradation was investigated (Arabatzis et al., 2003). The photocatalytic activity of the titania films was improved after surface deposition of Au particles due to charge separation by attracting conduction band electrons. The most optimum concentration of Au particles on the catalyst surface was 0.8 $\mu g/cm^2$. The photocatalytic activity improvement of titania films due to Au deposition was more than 100%.
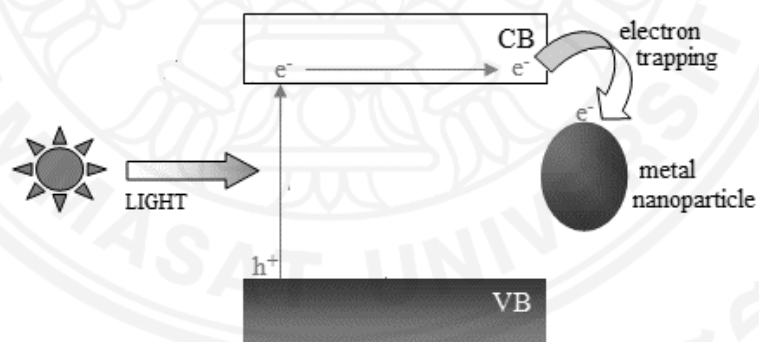
Figure 2.6 Electron trapping by deposited metal.

Similar finding was also reported on Au/TiO_2 for MO degradation. The Au/TiO_2 was obtained through green synthesis method using aqueous extract of *Cinnamomum tamala* leaves as reducing/capping reagent (Naik et al., 2013). The catalyst prepared at pH of 9 taking 2 %wt. Au in TiO_2 and double volume of plant extract as that of $HAuCl_4$ solution showed highest photocatalytic activity.

2.4.4 Surface sensitization

Surface sensitization using dye molecules, polymer, or colorless organic molecules such as toluene 2,4-diisocyanate can also enhance the photocatalytic activity of metal oxide catalyst (Chen et al., 2009; Eskizeybek et al., 2012). Dye sensitization has shown to be a potent way for extending photoresponse of catalyst into the visible region. The dye molecule can absorb visible light for exciting its electron and subsequently transfers the excited electron to the CB of catalyst (Figure 2.7). Nevertheless, it should be noted that the electron transfer is greatly dependent on the adsorption of sensitizer on the catalyst surface. In fact, the adsorption of sensitizer can also be disturbed by other coexisting species. The disadvantages of using sensitizer is that during light irradiation, the adsorbed sensitizer can be attacked by reactive species (Kaur & Singh, 2007).

For polymer sensitization and surface complex sensitization, the processes are generally similar to those in dye sensitization. But, polymers are more stable in water compared to dye molecules due to their low solubility in water (Jiang et al., 2008). Polymer, such as polyaniline, can reduce the electron-hole recombination by trapping the photogenerated electrons. In a surface complex, the colorless organic molecules are chemically bound to the host catalyst and can inject electrons into the CB of the catalyst.
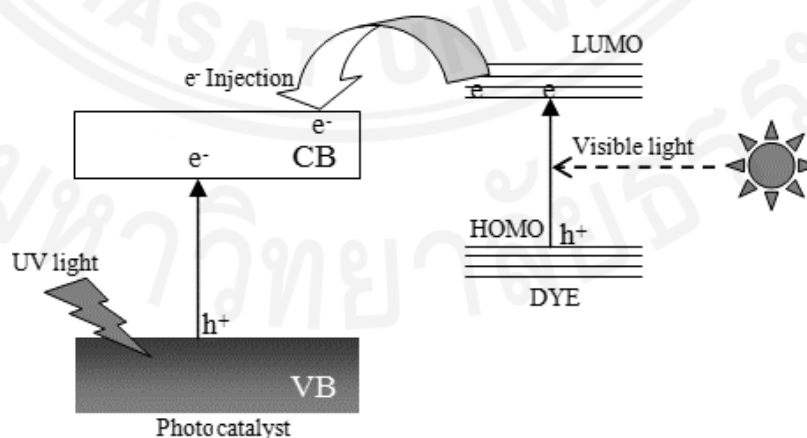
Figure 2.7 Electron transfer from during self-sensitization.

Natural dyes, such as anthocyanin, was also used as sensitizer of TiO_2 for degradation of methyl orange (MO) (Zyoud et al., 2011). With solar simulator light, 13% MO degradation by pristine TiO_2 occurred within 90 min. Using TiO_2/anthocyanin system under identical experimental conditions, 40% MO degradation is achieved. Under solar simulator irradiation, MO degradation occurred via two concurrent routes, namely, TiO_2 photocatalysis using small UV fraction and TiO_2 sensitization using visible light.

TiO$_2$ modified by Poly(3-hexylthiophene) (P3HT) (TiO$_2$/P3HT) were also used to degrade methyl orange (Wang et al., 2009). The dye degradation efficiencies within 10 h were found to be 88.5 and 13.5% using TiO_2/P3HT and TiO_2, respectively. After 10 cycles, 54% efficiency was still achieved by TiO_2/P3HT, implying its superb photocatalytic stability.

2.5 Doping of metal oxides with nitrogen

N doping would be an effective strategy to enhance photocatalytic activity of metal oxides due to extended spectral response and suppressed electron-hole recombination (Asahi et al., 2014). N is easily doped into the lattice structure of metal oxides because of its similar size with that of O (Pelaez et al., 2012). As the electronegativity of N is lower than that of O, a new energy level within the band gap (N_{2p}) can be formed by N. This N_{2p} state is known to be the origin of visible light response (Asahi et al., 2014). During the doping process, additional energy levels may also be introduced because of the formation of structural defects. These new energy levels allow multiple electron excitations, leading to extended spectral response, and can act as electron traps, resulting in enhanced photocatalytic activity.

Speaking about chemical state and location of N species in N-doped metal oxides, these matters are still under debate. The doped N in metal oxides can exist in a variety of chemical states, which are greatly dependent on the synthesis technique used. Different chemical states of N are possible, including substitutional N and interstitial N (in the form of NO_x, NH_x, or other aromatic compounds).

There are a variety of sources for N, such as urea, thiourea, melamine, diethanolamine, triethylamine, ammonia, and ammonium chloride (Di Valentin et al., 2007). By using the same N source, but different synthesis method, a particular N-

doped metal oxide with different structural properties and photocatalytic activities is typically obtained.

It is also observed in some reports that an N containing compound may be suitable as N source for a certain metal oxide, but it may not lead to N doping for another metal oxide. To give an instance, N-doped GeO_2 can be obtained by mixing pristine GeO_2 with thiourea as N source (Charanpahari et al., 2013). However, by using thiourea as N source for ZnO, S-doped ZnO is obtained instead of N-doped ZnO, although similar synthesis technique, namely, solid state synthesis, is applied (Patil et al., 2010).

Moreover, it must be noted that extension of spectral response to longer wavelength does not always end up with photocatalytic activity enhancement, because many factors play a role. For example, in the case of N-ZnO prepared by thermal decomposition of zinc nitrate, the spectral response of N-ZnO was significantly shifted to longer wavelength and its absorption intensity was also increased (Shifu et al., 2009).

In some cases, high concentration of N in the doped matrix is also detrimental to photocatalytic activity. This is because the charge neutrality induces the O vacancies in metal oxides, acting as recombination centers for charge carriers (Asahi et al., 2014). Hence, the concentration of N dopant in the doped matrix should be carefully controlled.

The possible mechanism of dye degradation by an N-doped metal oxide are illustrated in Figure 2.8. The excitation of electron in N-doped metal oxide upon visible light or UV light irradiation takes place through different pathways. In the case of dye degradation under visible light irradiation, the electron in the dye molecule can be excited and subsequently transferred to the CB of the catalyst. After transferring its electrons, the excited dye becomes radical cation and undergoes further degradation. With N-doped metal oxide, the dye can also be directly oxidized by the hole generated in the N_{2p}. It is seen that N doping enables different pathways of electron excitation to occur. As a result, more charge carriers can be generated.
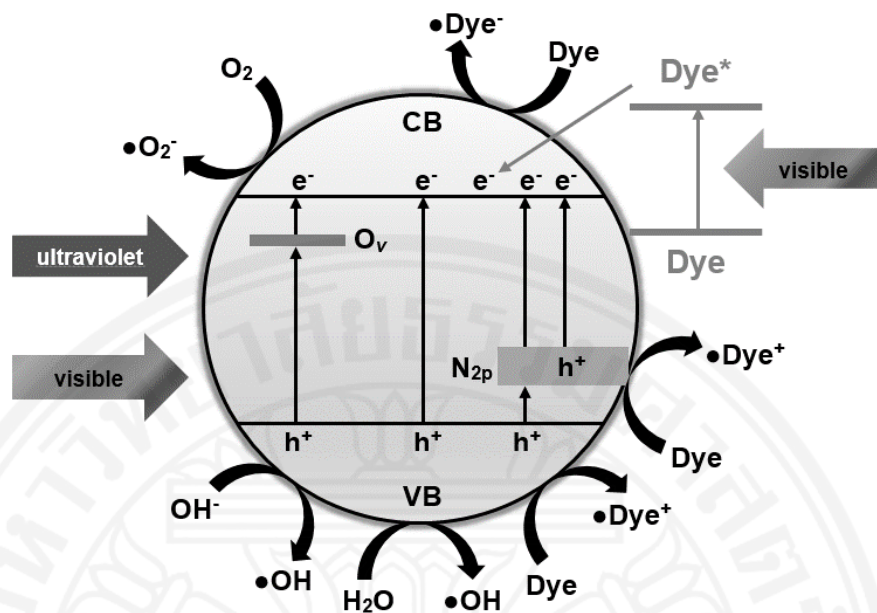
Figure 2.8 Illustration of charge carrier generation in an N-doped metal oxide upon light irradiation during dye degradation.

Overall, N doping can be beneficial for enhancing the photocatalytic activity of metal oxide catalysts, provided that appropriate N source is used and suitable N doping technique and proper concentration of N are applied. However, it should also be understood that after doping with N, the oxidation power of N-doped metal oxide typically decreases due to potential reduction of produced h^+ (Asahi et al., 2014). Consequently, the quantum efficiency decreases, although the photoabsorption efficiency especially in visible light region increases. Thus, the contribution of N doping is basically the compromise between quantum efficiency and photoabsorption efficiency.

2.6 Catalyst immobilization on textile fabrics

Many studies have been reported on use of N-doped metal oxides for photocatalysis of organic pollutants, including dyes, with slurry system. However, from a practical viewpoint, recovering the used catalysts from slurry system is a challenging task as it requires considerably long settling times for sedimentation and can be expensive for filtration. Light scattering by catalyst particles is also another issue.

To avoid the problem of post separation, immobilization of the catalyst on a stationary, solid support would be promising. A variety of supporting materials have

been employed, including stainless steel mesh (Jung & Yong, 2011), polyacrylic film (Noorjahan et al., 2004), glass beads (Karches et al., 2002), Perlite granules (Hosseini et al., 2007), Pumice stones (Rao et al., 2003), pebbles (Rao et al., 2012), Cuddapah stones (Noorjahan et al., 2003), and porous silica (Pucher et al., 2007).

Recently, textile fabrics, made from flax (Dong et al., 2007), cotton (Rahal et al., 2011), nylon (Mejía et al., 2011), wool (Moafi et al., 2010), and polyester (Mejia et al., 2010), have also been proposed as suitable catalyst support due to their flexibility, relative stability, and low-cost. It is reported $N-TiO_2$ coating on cotton fabric ($N-TiO_2$@cotton fabric) for the purpose of methyl orange (MO) degradation was successfully prepared using a dip-coating method. The prepared photoactive system showed good performance for MO degradation. It could degrade 43% of 5 mg/L MO in 120 min under visible light irradiation in batch reactor. Its performance can also be maintained for the cycling experiments.

Cotton fabric was also employed as support for $BiVO_4$ (Wang et al., 2013b). It is simply prepared through a chemical bath deposition method at 100 °C. By using the proposed coating technique, the cotton fabric was not damaged and the surface of the fabric was covered uniformly by $BiVO_4$ particles with size of around 0.2–1 μm. Results showed that TOC reduction of 48% was achieved within 4 h.

Polyester fabric was used as support for TiO_2 nanoparticles for degradation of methanol in gas phase under UV light in continuous flow reactor in single pass mode (Mejia et al., 2010). The flow is tangential to the photoactive system. SiO_2 was added on the polyester surface to bind catalyst particles as well as to protect the polyester from reactive species produced during light irradiation. The TiO_2-SiO_2-polyester system was prepared by immersion, drying and curing process. The photoactive system prepared with an immersion time of 11 h showed appreciable photocatalytic activity, in which almost 20% efficiency for methanol degradation was achieved within 180 min.

In a similar research, polyester fabric was also used as support of TiO_2 for photocatalytic degradation of gaseous formaldehyde on a fix-bed photo-reactor under UV light (Han et al., 2012). To anchor the catalyst particles, colloidal SiO_2 was added in the coating suspension. Two coating techniques, dip coating and spray coating,

were evaluated. The TiO$_2$-SiO$_2$-polyester fabric prepared through spray coating exhibited much higher photocatalytic activity as compared to that prepared by dip coating due to more uniform and stable coating of TiO$_2$ particles. It was able to degrade up to 92.8% of formaldehyde with initial concentration of 24.6 ppm within 105 min.

Polyester fabric was employed for supporting TiO$_2$ nanoparticles for degradation of reactive orange 16 in tubular reactors with recirculation (Marandi et al., 2012). Results showed that the dye degradation rate obeys pseudo first order kinetics. Repeated use of the photoactive system did not significantly reduce its performance.

Nylon fabric was utilized as support for TiO$_2$ nanoparticles of Degussa P-25 (Mejía et al., 2011). SiO$_2$ was added as binder to anchor the TiO$_2$ particles. The TiO$_2$-SiO$_2$-nylon fabric system was evaluated for the degradation of gaseous methanol in plug flow tubular reactor in single pass mode under UV light. The TiO$_2$ particles can be inserted in SiO$_2$ matrix and remains catalytically active during methanol degradation. The photoactive system prepared with immersion time of 11 h could degrade 15% of methanol within 120 min.

2.7 Thin-film fixed-bed reactor for photocatalysis

Reactors for photocatalysis can basically be divided into two types, slurry system and immobilized system. Using slurry system, such as annular reactor with horizontal flow and thin-film slurry photocatalytic reactor (TFS), high catalytic area to reactor volume ratio, high mass transfer, and good mixing of catalyst particles in the suspension are achieved. Therefore, high photocatalytic efficiency is expected. However, working with slurry system is impractical since it requires difficult, costly post-separation of catalyst particles, which are typically in nanometer range. Taking the issue of post-separation of catalyst particles into account, immobilized system would be preferable. Nevertheless, it should be kept in mind that with immobilized system, the utilization efficiency of incoming light is low and mass transfer limitation is quite significant (De Lasa et al., 2005).

Several types of immobilized/fixed catalyst systems have been developed, including Thin-Film Fixed-Bed Reactor (TFFBR) (Khan et al., 2012), Thin-Film

24

Cascade Reactor (Chan et al., 2003), Fiber Photoreactor (FP) (Dijkstra et al., 2003), Optical Fiber Photoreactor (OFP) (Braham & Harris, 2009), Packed Bed Reactor (PBR) (Dijkstra et al., 2001), Rotating Disc Reactor (RDR) (Dionysiou et al., 2000a), and Photocatalytic Membrane Reactors (PMRs) (Mozia, 2010). They can be a light concentrating system or a non-light concentrating system.

Among photocatalytic reactors, TFFBR offers simple operation and maintenance and low cost of investment. Under solar irradiation, it can be used without a light concentrating system, enabling diffuse and direct portions of solar light to be utilized. The sloping plate is the most important part for TFFBR. It can be either coated directly with catalyst particles or the place for placing the support of catalyst particles. It is brought into contact with the solution system containing pollutant to be degraded. The solution falls over the surface of the sloping plate as a thin film. TFFBR has advantages of minimal mass transfer limitation, effective oxygen transfers from the air into the thin film of the solution (Bahnemann, 2004).

(a) (b)
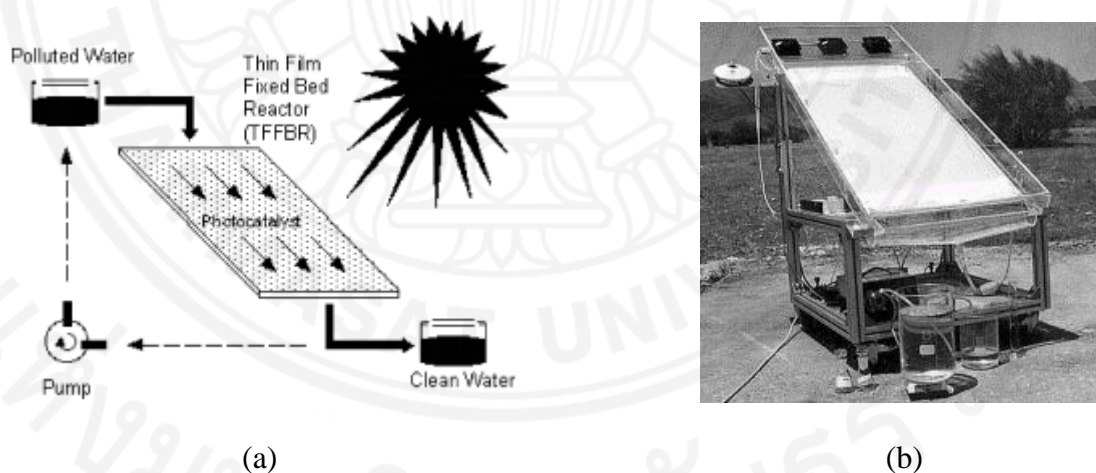
Figure 2.9 Basic configuration of a TFFBR (a) and photograph of a TFFBR (b) (Bahnemann, 2004).

TFFBR can be operated either in single pass or with recirculation. For degradation of organic pollutants in solution system, TFFBR is normally operated in recirculation mode. A TFFBR in recirculation mode was employed for evaluating the TiO_2 nanoparticles coated on glass slides for degradation of dyes under UVA light

(Khataee et al., 2009). The TFFBR photocatalytic system could completely degrade 30 mg/L of acid orange 10 in 130 min.

A novel TFFBR system containing white pebbles as catalyst support was evaluated in recirculation mode for degradation of various dyes under solar light (Rao et al., 2012). The pebbles, which are silica rich, were coated with TiO_2 particles and were put on the sloping plate. The system was found to work efficiently, in which a mineralization efficiency of up to 28% for 25 mg/L dyes could be achieved in 5 h.

In a research work, a pilot plant TFFBR with recirculation mode, consisting of two fixed and adjacent concrete made reactors was employed for degrading Yellow cibacron FN-2R under solar light (Zayani et al., 2009). The sloping plates with an inclination angle of 20° and an irradiated area of 25 m^2 each were coated with TiO_2 Degussa P25 particles. With a catalyst loading of 20 g/m^2, 70 mg/L of dye, recirculation rate of 3 m^3/h, the apparent rate constant were found to be about 13 × 10^3 min^{-1}.

Furthermore, a TFFBR for the purpose of degradation of H-acid was also evaluated in recirculation mode under solar light (Noorjahan et al., 2003). The sloping plate with an irradiated area of 7488 cm^2 was filled with Cuddapah stones as support for TiO_2 Degussa P25 particles. The catalyst coating was simply carried out using spray technique without any heat treatment. At the chosen experimental conditions (initial H-acid concentration of 10^{-4} M, irradiation time of 15 h, flow rate of 750 ml/min), 62% COD reduction was obtained. Based on this research, the proposed solar photocatalytic system with TFFBR is suggested as economical and efficient way of treating effluents at larger scale.

Chapter 3
Materials and Methods

This chapter provides the experimental procedures which consist of two parts, dye degradation in batch slurry system and continuous flow system. The catalyst particles were first synthesized using mechanochemically assisted thermal decomposition method, characterized, and evaluated for the dye degradation in batch slurry system. The characterization of the catalyst particles was done with XRD, FTIR, TGA, SEM, TEM, DRS, XPS, XANES, BET, and zeta potentiometry. Subsequently, two selected catalysts were immobilized in polyester fabric by heat attachment method, characterized, and evaluated for the AM degradation in continuous flow system with a TFFBR. XRD, ATR-FTIR, SEM, and DRS were used for the characterization of the immobilized catalysts. The overall study is summarized in Table 3.1.

Table 3.1 Summary of the study.

	BATCH SLURRY SYSTEM	CONTINUOUS FLOW SYSTEM
SYNTHESIS	**N-ZnO N-ZrO$_2$ N-WO$_3$** • **Synthesis method:** mechanochemically assisted thermal decomposition of urea-metal precursor complex • **Synthesis optimization:** molar ratio of urea/metal precursor (U/Z) is varied (0.25, 0.5, 1 and 2) • **Metal precursors:** zinc acetate for N-ZnO, zirconium hydroxide for N-ZrO$_2$, and peroxotungstic acid for N-WO$_3$	**N-WO$_3$@PF N-ZnO@PF** • **Synthesis method:** heat attachment of catalyst particles onto polyester fabric (PF)
CHARACTERIZATION	• **Catalysts:** pristine catalysts and N-doped catalysts with U/Z of 2 • **Methods:** XRD, FTIR, TGA, DRS, SEM, TEM, XPS, XANES, BET, zeta potentiometry	• **Catalysts:** N-WO$_3$@PF and N-ZnO@PF • **Methods:** XRD, ATR-FTIR, DRS, SEM
EVALUATION	**N-ZnO** • **Dyes:** MB, AM, R6G • **Light sources:** visible, UVC • **Operating parameters:** dye concentration, catalyst concentration, pH, salinity • **Role of reactive species and effect of H$_2$O$_2$ concentration** in R6G degradation **N-ZrO$_2$** • **Dyes:** MB, AM, R6G • **Light sources:** visible, UVC, UVA • **Operating parameters:** dye concentration, catalyst concentration, pH, salinity • **Role of reactive species and effect of H$_2$O$_2$ concentration** in R6G degradation **N-WO$_3$** • **Dye:** AM • **Light sources:** visible, UVA • **Operating parameters:** dye concentration, catalyst concentration, pH, salinity, H$_2$O$_2$ concentration, inorganic ions • **Role of reactive species**	**N-WO$_3$@PF** • **Dye:** AM • **Light sources:** solar, visible, UVA • **Operating parameters:** dye concentration, pH, inclination angle, recirculation rate, salinity, inorganic ions • **IUPAC figures-of-merit** for AM degradation under solar light **N-ZnO@PF** • **Dye:** AM • **Light source:** solar • **Operating parameters:** dye concentration, pH, inclination angle, recirculation rate, salinity, inorganic ions • **IUPAC figures-of-merit**

3.1 Materials

All the chemicals in this study were used as purchased: zinc acetate dihydrate $(Zn(O_2CCH_3)_2 \cdot 2H_2O$, Ajax), tungstic acid $(H_2WO_4$, Aldrich), zirconium oxychloride octahydrate $(ZrOCl_2 \cdot 8H_2O$, Wako), urea $(CO(NH_2)_2$, Merck), commercial zinc oxide (ZnO, Chameleon Reagent), commercial zirconium dioxide $(ZrO_2$, Chameleon Reagent), commercial tungsten trioxide $(WO_3$, Aldrich), hydrogen peroxide $(H_2O_2$, Wako), methylene blue $(C_{16}H_{18}ClN_3S$, Merck), rhodamine 6G $(C_{28}H_{31}N_2O_3Cl$, Aldrich), amaranth $(C_{20}H_{11}N_2Na_3O_{10}S_3$, Aldrich), sodium hydroxide (NaOH, Wako), potassium iodide (KI, Aldrich), isopropanol $((CH_3)_2CHOH$, Aldrich), sodium azide $(NaN_3$, Aldrich), 2-chloroethanol $(Cl(CH_2)_2OH$, Aldrich), p-benzoquinone $(C_6H_4O_2$, Aldrich), sodium chloride (NaCl, Chameleon reagent), sodium nitrate $(NaNO_3$, Aldrich), sodium carbonate $(Na_2CO_3$, Chameleon reagent), sodium sulfate $(Na_2SO_4$, Chameleon reagent), ammonium sulfate $((NH_4)_2SO_4$, Chameleon reagent), and calcium sulfate $(CaSO_4$, Chameleon reagent). An undyed 100% polyester fabric, obtained from a local market, was used.

3.2 Dye degradation in batch slurry system

3.2.1 Synthesis of N-doped metal oxides

3.2.1.1 Synthesis of N-ZnO

The N-ZnO was synthesized by thermal decomposition of zinc acetate-urea complex. Zinc acetate dihydrate (2.19 g) was firstly ground in an agate mortar with required amount of urea for 30 min to form zinc acetate-urea complex. The ground mixture was calcined at 500 ℃ for 3 h in a muffle furnace. The molar ratio of urea/zinc acetate (U/Z) is varied (0.25, 0.5, 1 and 2). The powder obtained was washed with water followed by ethanol prior to drying in an oven at 100 ℃ for 24 h. Furthermore, pristine ZnO was synthesized using the same method in the absence of urea. For comparison, N-ZnO was also synthesized by using a similar method with commercial ZnO (c/ZnO) and urea as starting materials, denoted as c/N-ZnO. The molar ratio of urea/commercial ZnO is 2.

3.2.1.2 Synthesis of N-ZrO$_2$

The N-ZrO$_2$ was synthesized by thermal decomposition of zirconium hydroxide-urea complex. The zirconium hydroxide was obtained through precipitation of zirconium oxychloride. About 3.22 g of zirconium oxychloride was dissolved in 20 mL of water with continuous stirring. NaOH was slowly added to the solution under continuous stirring. The obtained precipitate of zirconium hydroxide was collected by centrifugation, repeatedly washed with water, and ground with required amount of urea in an agate mortar for 30 min. The molar ratio of urea/zirconium hydroxide (U/Z) is varied (0.25, 0.5, 1 and 2). The ground mixture was dried in an oven at 100 °C for 24 h. It was then calcined at 600 °C for 3 h in a muffle furnace to form crystalline N-ZrO$_2$. The as-synthesized N-ZrO$_2$ was washed with water followed by ethanol prior to drying at 100 °C for 24 h. Furthermore, pristine ZrO$_2$ was synthesized by the same method without adding urea. For comparison, the N-ZrO$_2$ was also synthesized using a similar way with commercial ZrO$_2$ (c/ZrO$_2$) and urea as starting materials, denoted as c/N-ZrO$_2$. The molar ratio of urea/commercial ZrO$_2$ is 2.

3.2.1.3 Synthesis of N-WO$_3$

The N-WO$_3$ was synthesized by thermal decomposition of peroxotungstic acid-urea complex. The peroxotungstic acid was obtained through the reaction of H$_2$WO$_4$ with H$_2$O$_2$. About 3.75 g of H$_2$WO$_4$ was dispersed in 75 mL of water with continuous stirring, followed by addition of 25 mL of aqueous H$_2$O$_2$ (35 wt.%) into the dispersion. The reaction mixture was further stirred for 24 h at 40 °C. After drying, the obtained powder was dissolved in 75 mL of hot water with continuous stirring for 1 h at 75 °C. The solid product was collected by centrifugation and subsequently ground with required amount of urea in an agate mortar for 30 min. The molar ratio of urea/peroxotungstic acid (U/Z) is varied (0.25, 0.5, 1 and 2). The ground mixture was calcined at 500 °C for 3 h in a muffle furnace to form crystalline N-WO$_3$. The N-WO$_3$ was washed with water followed by ethanol prior to drying at 100 °C for 24 h. Furthermore, pristine N-WO$_3$ was synthesized by the same method without adding urea. For comparative purpose, N-WO$_3$ was synthesized using a similar method with commercial WO$_3$ (c/WO$_3$) and urea as starting materials, denoted as c/N-WO$_3$. The molar ratio of urea/commercial WO$_3$ is 2.

3.2.2 Characterization

A Fourier transform infrared (FTIR) spectrometer (FT-IR-610, Jasco) was employed for functional group elucidation. Crystallinity and structural properties were evaluated with X-ray diffraction (XRD) on a Bruker D8 diffractometer (Cu Kα radiation, λ = 1.5406 Å). The morphological properties were observed by scanning electron microscopy (SEM) (V88-SI, Keyence) and transmission electron microscopy (TEM) (JEM 2100, Jeol). The textural properties were examined using N_2 adsorption-desorption isotherms at liquid nitrogen temperature of 77 K by an adsorption instrument (Belsorp 28SA, Bel). The diffuse reflectance spectra (DRS) were obtained from a UV-Vis-NIR spectrophotometer (Cary 5000, Agilent). The chemical state of N dopant was verified by X-ray photoelectron spectroscopy (XPS) (Axis Ultra DLD, Kratos Analytical) with Al Kα radiation and X-ray absorption near-edge spectroscopy (XANES) at Beamline 3.2a of the Synchrotron Light Research Institute (Public Organization), Thailand. The photon energy of XANES spectra was calibrated with graphite (HOPG) carbon *K*-edge instead of gaseous N_2 since high pressure of gas in vacuum is harmful for surface sensitive experiments. The thermal properties were investigated by thermogravimetric (TG) analysis (TGA/SDTA 851, Mettler Toledo). The zeta potentials were measured as a function of pH using an electrophonic light scattering spectrophotometer (ELS-8000, Otsuka).

3.2.3 Photocatalytic activity evaluation

The photocatalytic activity of the catalyst particles was evaluated by the degradation of AM, MB, and R6G under visible and UV light in batch slurry system. A suspension (0.1 L) containing known concentrations of the dye and the catalyst was transferred into a batch photoreactor. The reactor configurations are shown in Figure 3.1 and Figure 3.2. The suspension pH was adjusted to a desired level using dilute NaOH and HCl. The suspension was then magnetically stirred for 2 h in the absence of light to attain adsorption-desorption equilibrium. In all the cases, the adsorption of dyes at equilibrium is less than 8% of initial concentration.
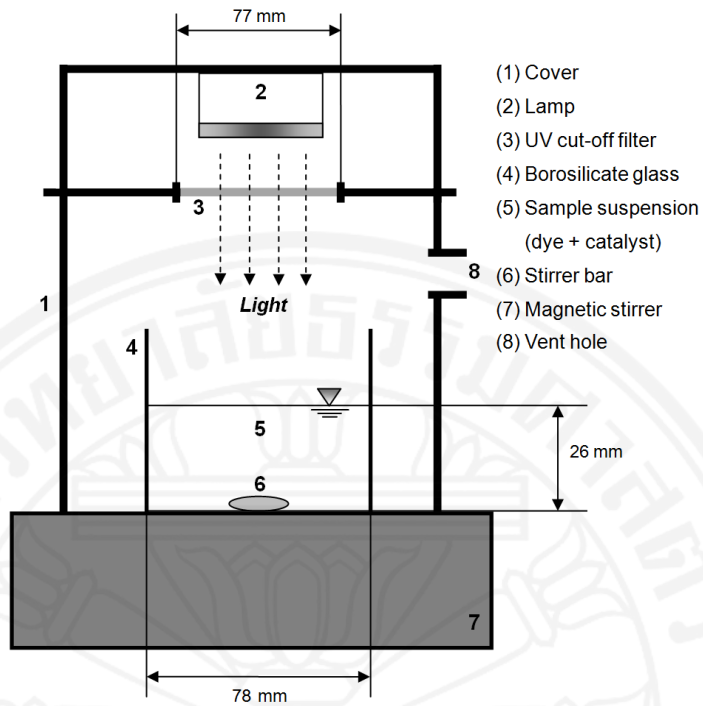
Figure 3.1 Experimental setup for the dye degradation under visible or UVA light. The lamp is a fluorescent lamp, a metal halide lamp, or a blacklight lamp. The cut-off filter ($\lambda > 400$ nm) was not used for the experiments using the blacklight lamp.
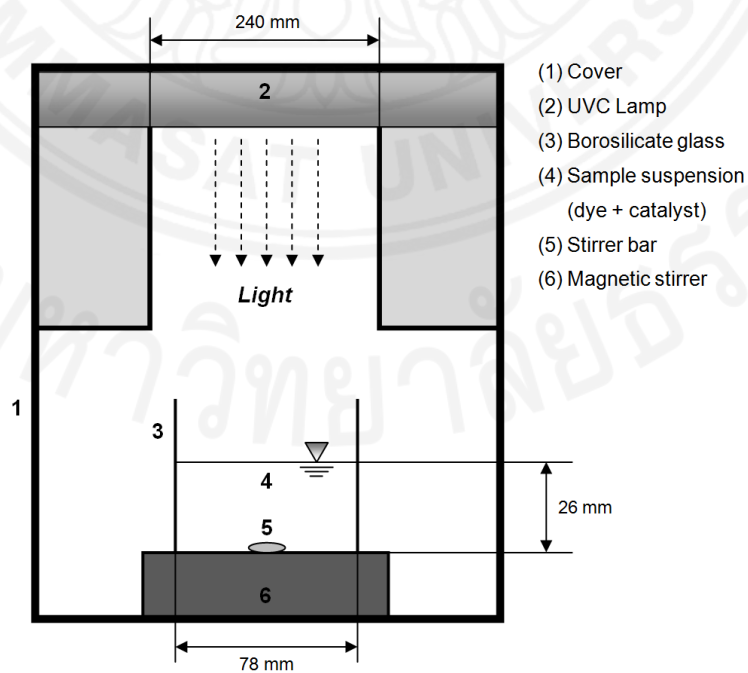
Figure 3.2 Experimental setup for the dye degradation under UVC light. The lamp is a low-pressure mercury lamp.

For evaluating the photocatalytic activity of N-ZnO and N-ZrO$_2$, a fluorescent lamp 24 W (General Electric) and a low-pressure mercury lamp 15 W (Toshiba) were used as visible and UVC light sources, respectively. The average visible light irradiance and UVC light irradiance at the topmost surface of the suspension were 16.5 W/m^2 and 3.5 W/m^2, respectively. For evaluating the photocatalytic activity of N-WO$_3$, a metal halide lamp 160 W (Philips) with an irradiance of 144.7 W/m^2 and a blacklight lamp 13 W (General Electric) with an irradiance of 3.5 W/m^2 were used as visible and UVA light sources, respectively. The metal halide lamp and blacklight lamps were also used in the experiments with N-ZrO$_2$, to study the effect of higher visible light intensity and UVA on the degradation of dyes. After the lamp was switched on for a given irradiation time, the suspension was withdrawn and centrifuged to measure the absorbance of MB solution at λ_{max} of 664 nm, AM solution at λ_{max} of 521 nm, and R6G solution at λ_{max} of 528 nm by using a UV-vis spectrophotometer. The dye concentration was determined based on the calibration plots of the absorbance versus the concentration. The dye degradation efficiency (*DE*) was calculated from the equation:

$$DE(\%) = \left(\frac{C_0 - C}{C_0}\right) \times 100 \tag{3.1}$$

where, C_0 and C are the initial dye concentration and the dye concentration after irradiation (mg/L), respectively.

Control experiments in the absence of catalyst were carried out with continuous stirring for 6 h. The dyes are quite stable upon irradiation under the experimental conditions applied, resulting in photolysis of less than 12%, as shown in Appendix E.

3.2.3.1 Effect of operating parameters

To study the effect of operating parameters on the dye degradation, the experiments were performed by varying key operating parameters, namely dye concentration (5-25 mg/L), catalyst concentration (0.5-2.5 g/L), pH (5-9), and salinity (0.3-9.6 g/L NaCl). The effects of H$_2$O$_2$ concentration (0.1-0.7 g/L) on the R6G degradation by N-ZnO

and N-ZrO$_2$ and the AM degradation by N-WO$_3$ were studied. The effects of anions (CO$_3^{2-}$, Cl$^-$, SO$_4^{2-}$, NO$_3$) and cations (Ca^{2+} and NH$_4^+$) on the AM degradation by N-WO$_3$ was also investigated through addition of sodium salts and sulfate salts, respectively, with a concentration of 0.1 M.

3.2.3.2 Role of reactive species

In order to find out reactive species responsible for the degradation of R6G by N-ZnO and N-ZrO$_2$ and the degradation of AM by N-WO$_3$, a series of quenchers were used to scavenge the reactive species. Different amounts of quenchers were introduced into the dye solution before catalyst addition. KI (0.1 g/L), isopropanol (1 g/L), NaN$_3$ (0.01 g/L), 2-chloroethanol (0.36 g/L), and p-benzoquinone (0.02 g/L) were used to quench h$^+$, •OH, ^{1}O$_2$, e$^-$, and •O$_2^-$, respectively (Antonopoulou et al., 2013). In the presence of quenchers, the dye degradation is suppressed to a certain extent and the decreased apparent pseudo first order kinetic constant (k_{app}) is observed. The more the k_{app} is decreased, the more vital the role of the reactive species. The role (RS) of the reactive species was indicated by:

$$RS(\%) = \left(\frac{k_{app} - k'_{app}}{k_{app}} \right) \times 100 \tag{3.2}$$

where, k'_{app} is the k_{app} in the presence of quencher. k_{app} is obtained based on the apparent pseudo first order kinetic model:

$$r = -\frac{dC}{dt} = k_{app}C \tag{3.3}$$

Integrating Eq. (3.3) yields:

$$ln\left(\frac{C_0}{C}\right) = k_{app}t \tag{3.4}$$

Therefore, k_{app} can be obtained by plotting ln (C_0/C) as a function of t.

3.2.3.3 Catalyst reusability

The catalyst reusability was evaluated by reusing the catalyst five times under identical experimental conditions. After being used for the first time, the catalyst is separated from the slurry system by centrifugation. Catalyst washing with water followed by drying at 100 ºC for 24 h were undertaken and the catalyst was then used for the next run.

3.2.3.4 Toxicity evaluation

The toxicity of the photocatalytically treated dye solution against *Bacillus cereus*, an agriculturally important soil microorganism (Aftab et al., 2011), was evaluated using resazurin microplate assay (REMA) method (Palomino et al., 2002). REMA is a fluorescence-based bioassay employing resazurin for evaluating cell viability. Conversion of resazurin to resorufin by viable cells leads to a fluorescent product, which emits fluorescence at 590 nm and is proportional to the number of viable cells. The evaluation was conducted for MB and AM solutions photocatalytically treated with N-ZnO and $N-ZrO_2$ under visible light at selected experimental conditions. Interference due to autofluorescence of the samples containing MB or AM is not likely to occur since the positions of the fluorescence emissions of those dyes are different than that of resofurin.

3.2.3.5 Leaching of N dopant

To verify the N leaching into the solution, a suspension containing the catalyst particles was irradiated by UV light for 4 h. After catalyst separation by centrifugation, the solution was filtered through a 0.45 μm membrane filter, prior to measurement of total nitrogen (TN) by TOC analyzer equipped with TNM-L TN unit (TOC-L CSH/CSN, Shimadzu). The TN measurement was based on a chemiluminescence method with a detection limit of 5 μg/L. To determine the N concentration, a calibration curve was created using a potassium nitrate solution. All of the experiments were replicated twice under identical conditions. The results were presented as a mean of two experiments.

3.3 Dye degradation in continuous flow system

3.3.1 Immobilization of N-WO$_3$ and N-ZnO on polyester fabric

The N-WO$_3$ and N-ZnO particles were immobilized on polyester fabrics to form photoactive systems, denoted as N-WO$_3$@PF and N-ZnO@PF, respectively. For preparing N-WO$_3$@PF, the fabric with a size of 20 cm × 20 cm was first cleaned with detergent at 80 ºC for 30 min and rinsed with a large amount of water to remove impurities. After being cleaned with acetone at room temperature for 30 min, it was immersed in 1 M of NaOH solution at 80 ºC for 2 h, repeatedly rinsed with water, and dried at 80 ºC for 24 h. Subsequently, the alkali-treated fabric was irradiated with UVC light at room temperature for 5 h, immersed in 16 g/L of N-WO$_3$ suspension at room temperature for 24 h under agitation on a shaking bath at 200 rpm, and dried at 80 ºC for 24 h. Before immersion, the N-WO$_3$ suspension was sonicated in an ultrasonic bath for 2 h to de-agglomerate the N-WO$_3$ particles. Immersion-drying was undertaken five times successively. The coated fabric was further subjected to heating at 200 ºC for 30 min. To remove weakly attached particles, it was rinsed with water followed by drying at 80 ºC for 24 h. The average catalyst loading on the PF surface is found to be 16.4 g/m^2.

The procedure for preparing N-ZnO@PF was the same with that for preparing N-WO$_3$@PF. Using 16 g/L of N-ZnO suspension, the average catalyst loading on the PF surface is found to be 13.5 g/m^2.

3.3.2 Characterization

A Fourier transform infrared (FTIR) spectrometer (Nicolet 6700) in attenuated total reflection (ATR) mode was employed to record the infrared spectra. A Bruker D8 diffractometer (Cu Kα radiation, λ = 1.5406 Å) was used to collect the X-ray diffraction (XRD) patterns. The morphological properties were observed by scanning electron microscopy (SEM) (S-3400N, Hitachi). The diffuse reflectance spectra (DRS) were obtained from a UV-Vis-NIR spectrophotometer (Cary 5000, Agilent).

3.3.3 Photocatalytic activity evaluation

A thin-film fixed-bed reactor, consisting of a covered reservoir, a peristaltic pump, and a sloping plate for collecting light (Figure 3.3), was used. The operation regime during all experiments is continuous flow with recirculation. The photoactive system (N-WO$_3$@PF or N-ZnO@PF) was attached to the sloping plate having a workable area of 20 cm × 20 cm. The AM solution with a volume of 0.5 L was transferred into the reservoir. The pH of the AM solution was adjusted to a desired level using dilute NaOH and HCl. The AM solution falls as a thin film, allowing effective oxygen transfers from the air into the solution film.

The system was further irradiated with solar light to initiate a photocatalytic reaction. The solar irradiance was measured regularly during the experiments at the same angle as that of the sloping plate. The average solar irradiance during the AM degradation by N-WO$_3$@PF and N-ZnO@PF were found to be 577.2 and 585.1 W/m^2, respectively. For comparison, visible and UVA light were used in some experiments of the AM degradation by N-WO$_3$@PF. A metal halide lamp 250 W (Philips) with an irradiance of 210.5 W/m^2 and a blacklight lamp 11 W (General Electric) with an irradiance of 53.1 W/m^2 were used as visible and UVA light sources, respectively. When visible or UVA light irradiation was applied, the reactor was put in a box chamber, in which the inner wall is covered with aluminum foil to reflect light. After a given irradiation time, the solution was withdrawn and centrifuged to measure its absorbance at λ_{max} of 521 nm using a UV-vis spectrophotometer. The dye concentration was determined based on the calibration plots of the absorbance versus the concentration. The dye degradation efficiency (*DE*) was calculated according to the equation (3.1).

To study the effect of operating parameters, the experiments were performed by varying key operating parameters, namely dye concentration (5-25 mg/L), pH (5-9), plate inclination (20-40 degree), recirculation rate (80-120 mL/min), salinity (0.6-4.8 g/L of NaCl), and inorganic ions (Ca^{2+}, CO$_3^{2-}$, SO$_4^{2-}$, and NO$_3^-$ with a concentration of 0.05 M). DI water was circulated for 30 min to clean the system before the next run. All of the experiments were replicated twice under identical conditions and the results are presented as a mean of two experiments.
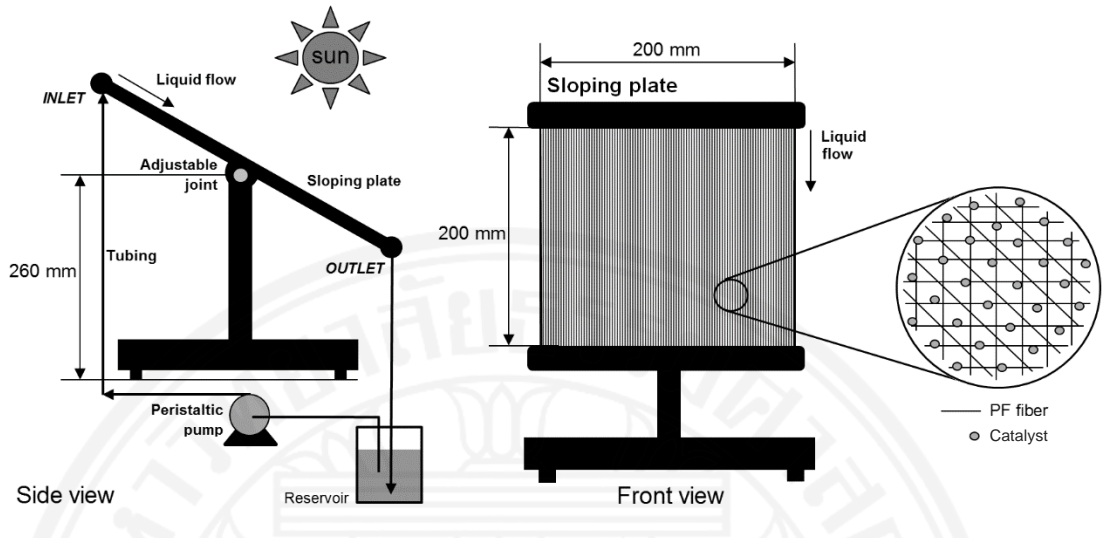
Figure 3.3 Experimental set-up for the photocatalytic degradation of AM using photoactive system in a TFFBR with recirculation under solar light.

3.3.4 IUPAC figures-of-merit

For evaluation and comparison of various advanced oxidation technologies (AOTs), figures-of-merit have been proposed by the photochemistry commission of International Union of Pure and Applied Chemistry (IUPAC) (Bolton et al., 2001). For AOTs with solar light, the figures-of-merit are estimated on the basis of solar collector area, namely the collector area per order (A_{CO}) and the collector area per mass (A_{CM}). They are defined as the collector area required for reducing the concentration of a contaminant in the water by one order of magnitude (for A_{CO}) or by unit mass of contaminant (for A_{CM}) within 1 h at 1000 W/m^2 (Bolton et al., 2001). Lower value indicates higher efficiency. A_{CO} (m^2/(m^3 order)) and A_{CM} (m^2/g contaminant) are calculated from:

$$A_{CO} = \frac{A \times E_S \times t}{1000 \text{ W/m}^2 \times 1 \text{ h} \times V \times \log (C_0/C)} \tag{3.5}$$

$$A_{CM} = \frac{A \times E_S \times t}{1000 \text{ W/m}^2 \times 1 \text{ h} \times V \times (C_0 - C)} \tag{3.6}$$

38

where, A (m^2) is the solar collector area, V (m^3) is the photocatalytically treated volume, E_S (W/m^2) is the average solar irradiance at 360 nm over the period t (h), and C_0 and C (mg/L) are the initial and final contaminant concentration, respectively.

Chapter 4

Dye degradation in batch slurry system

The experimental results of the dye degradation in batch slurry system and their discussion are presented in this chapter, including the properties of the catalysts. They are divided into three parts, namely dye degradation by N-ZnO, N-ZrO$_2$, and N-WO$_3$.

4.1 Dye degradation by N-ZnO

4.1.1 Photocatalytic activity of N-ZnO synthesized with different amounts of urea

To study the effect of urea addition on the photocatalytic activity enhancement, the N-ZnO catalysts synthesized with different amounts of urea were tested for the degradation of MB, AM, and R6G under visible and UVC light at chosen experimental conditions. As shown in Table 4.1, in all the cases, DE of the doped ZnO under visible light is higher than that of the pristine counterpart. DE increases with increasing U/Z. Similar results are found for the degradation of dyes under UVC light. DE increases with the increase of U/Z. It is clearly seen that urea addition improves the photocatalytic activity of pristine ZnO. This improved photocatalytic activity is most likely due to the alteration on the physicochemical properties of the catalysts as a result of N doping. In order to verify this, characterization is performed for the N-ZnO with U/Z of 2 as it is shown to have the highest activity. It is further evaluated for the degradation of dyes under different operating conditions.

Table 4.1 DE of the N-ZnO catalysts synthesized with different amounts of urea.

Light source	Dye	Irradiation time (h)	DE (%)				
			U/Z = 0	U/Z = 0.25	U/Z = 0.5	U/Z = 1	U/Z = 2
Visible	MB	0.8	29.2	45.2	60.7	75.2	82.4
	AM	2	41.5	62.3	71.4	82.9	83.6
	R6G	2.5	40.8	49.5	68.0	86.7	89.4
UVC	MB	1.5	75.7	81.8	85.6	89.0	89.3
	AM	4	78.0	79.5	84.2	87.1	88.5
	R6G	2	74.3	83.7	90.1	90.5	94.3

Initial dye concentration (C_0) = 10 mg/L, catalyst concentration (W) = 1 g/L, pH = 7, visible light intensity (I_{vis}) = 16.5 W/m^2, UVC light intensity (I_{UVC}) = 3.5 W/m^2.

4.1.2 Properties of N-ZnO

4.1.2.1 Crystallinity and structural properties

Figure 4.1 shows the XRD patterns of ZnO and N-ZnO. The diffraction patterns match the hexagonal structure of ZnO (JCPDS No.36-1451). No additional peaks are observed, suggesting that the catalysts have a single phase. After adding urea, the crystalline sizes decrease (Table 4.2), resulting in peak broadening. The crystallinity also slightly decreases due to crystal defects, crystal growth inhibition by the urea (Qin et al., 2011), or due to the substitution of O by N (Patil et al., 2011). As a result, the peak intensities lower. Considering the lattice shrinkage and the shift of several peaks to higher diffraction angles, it is suggested that N dopants may have been incorporated in the ZnO lattice. Interestingly, these N dopants do not lead to an extra phase due to their high solubility in the doped matrix.
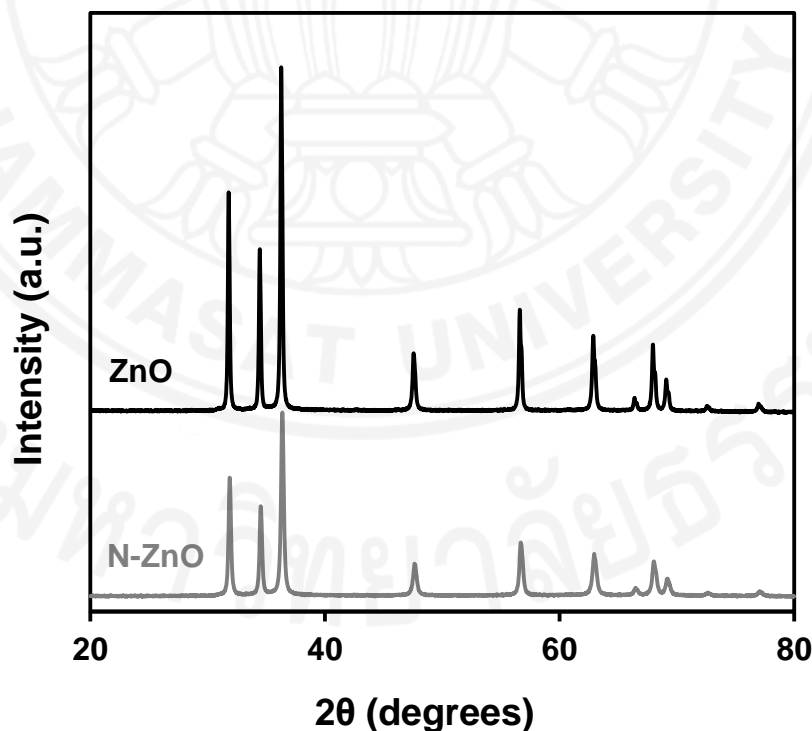
Figure 4.1 XRD patterns of ZnO and N-ZnO.

Table 4.2 Crystalline size and unit cell volume of ZnO and N-ZnO.

Catalyst	Crystalline size[a] (nm)	Unit cell volume[b] (Å^3)
ZnO	39.31	48.29
N-ZnO	29.08	47.15

[a] Calculated by the Scherrer equation.
[b] The formula of $0.866 \times a^2 \times c$ (hexagonal primitive cell) is used.

4.1.2.2 Vibrational spectroscopy

The FTIR spectra are shown in Figure 4.2. The intense, sharp peaks in the range of 400-600 cm^{-1} correspond to the Zn-O stretching modes and are indicative of the formation of crystalline ZnO (Ntwaeaborwa & Holloway, 2005). After N doping, Zn-O stretching peaks split into two components. This peak splitting is ascribed to the variation of the oxygen defect density (Zheng et al., 2007). The higher the splitting degree, the higher is the oxygen defect density. Since the splitting degree of Zn-O peak of N-ZnO is higher than that of ZnO, a higher density of oxygen defect in N-ZnO is expected. The oxygen defects such as oxygen vacancy are known to serve as electron traps which suppress electron-hole recombination (Wang et al., 2008; Zheng et al., 2007), and thus are beneficial for improving the photocatalytic activity.
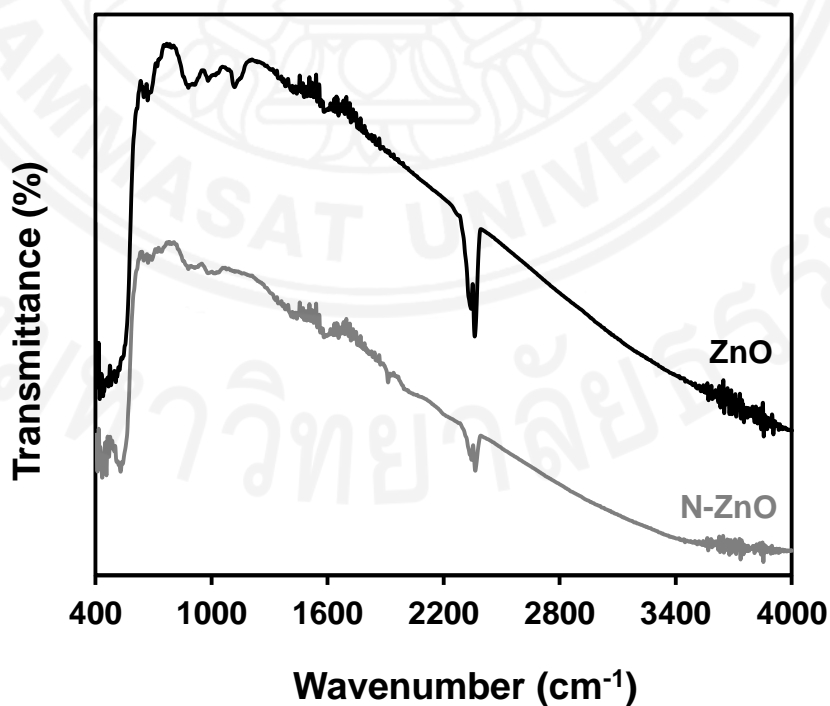
Figure 4.2 FTIR spectra of ZnO and N-ZnO.

4.1.2.3 Thermal properties

Figure 4.3 shows the thermogram of the catalysts. There are several stages of weight loss. The weight loss below 500 °C is from the removal of water adsorbed on the catalyst surface and in the catalyst pores. As for ZnO, no obvious weight loss was observed from 500-700 °C, indicating its high thermal stability. In the case of N-ZnO, a small weight loss appeared from 500-700 °C, which may be due to decomposition of surface hydroxyl groups (Aimable et al., 2010). This suggests that calcination temperatures of more than 500 °C are not preferable for obtaining a reasonably good N-ZnO since hydroxyl groups as one of the sources of hydroxyl radical would be removed from the surface. Moreover, the availability of surface functional groups such as hydroxyl groups may be higher for N-ZnO since more water is adsorbed.
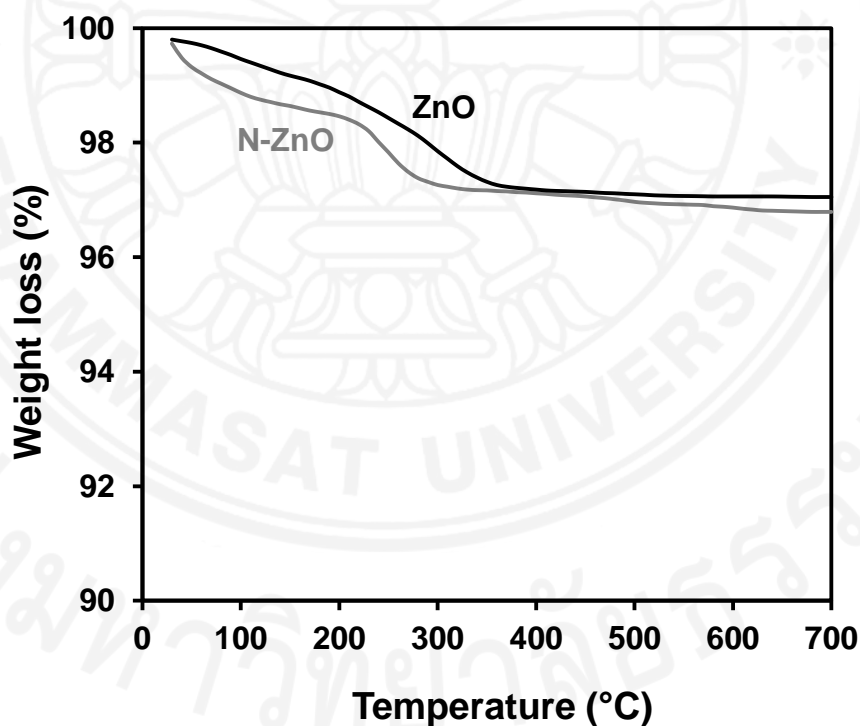
Figure 4.3 Thermogram of ZnO and N-ZnO.

4.1.2.4 Morphological properties

Figure 4.4(a) shows the aggregate structure of N-ZnO particles. The diameter of primary particles is in the range of 30-60 nm, as shown in Figure 4.4(b). The N-ZnO particles are of zero-dimensional structure. Furthermore, the lattice fringes with 0.26 nm are observed, corresponding to *d* spacing of hexagonal ZnO [002] plane (Figure 4.4(c)). The catalyst benefits from its particle size, which is in the nanometer range, to suppress the electron-hole pair recombination. This is possible since rapid migration of electron-hole pairs to the catalyst surface to undergo redox reactions is facilitated.
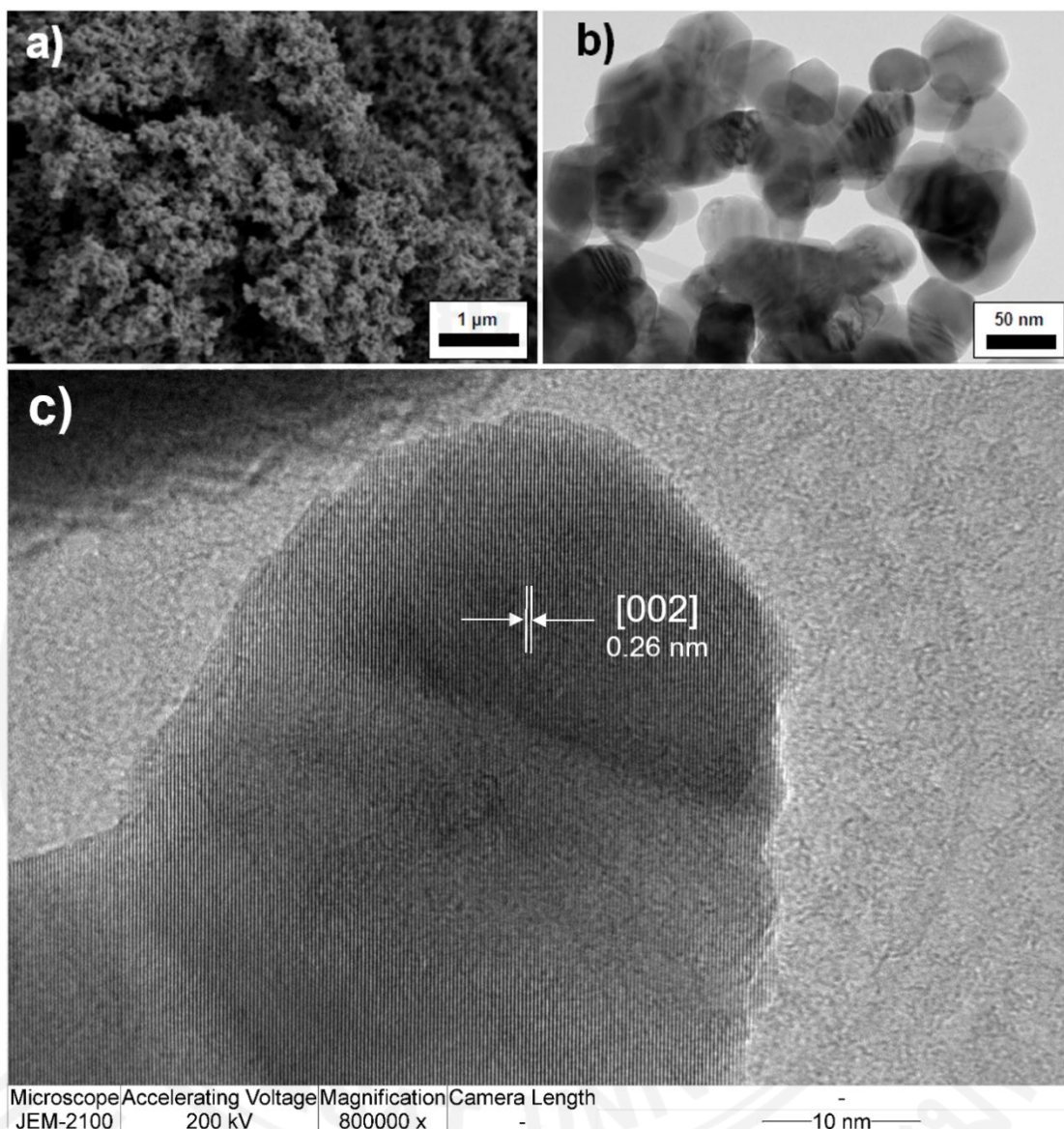
Figure 4.4 SEM (a), TEM (b), and HR-TEM (c) images of N-ZnO.

4.1.2.5 Optical properties

Figure 4.5 shows the DRS spectra of the catalysts. After doping with N, the spectral response is greatly extended not only to the visible region but also to the NIR region. The formation of a mid-band state by N 2p orbital within the band gap may be responsible for this extended spectral response. Along with this, oxygen defect band states, such as oxygen vacancy (O_v), may also be formed (Banerjee et al., 2014). Thus, the visible-NIR response in the N-ZnO could be due to the electron transition from the N mid-gap state to the CB, from the VB to the O_v, and/or from the O_v to the

CB. It should be noted that the oxygen vacancy and N mid-gap state may also act as electron traps in the N-ZnO that can prevent the electron-hole pairs from recombination.
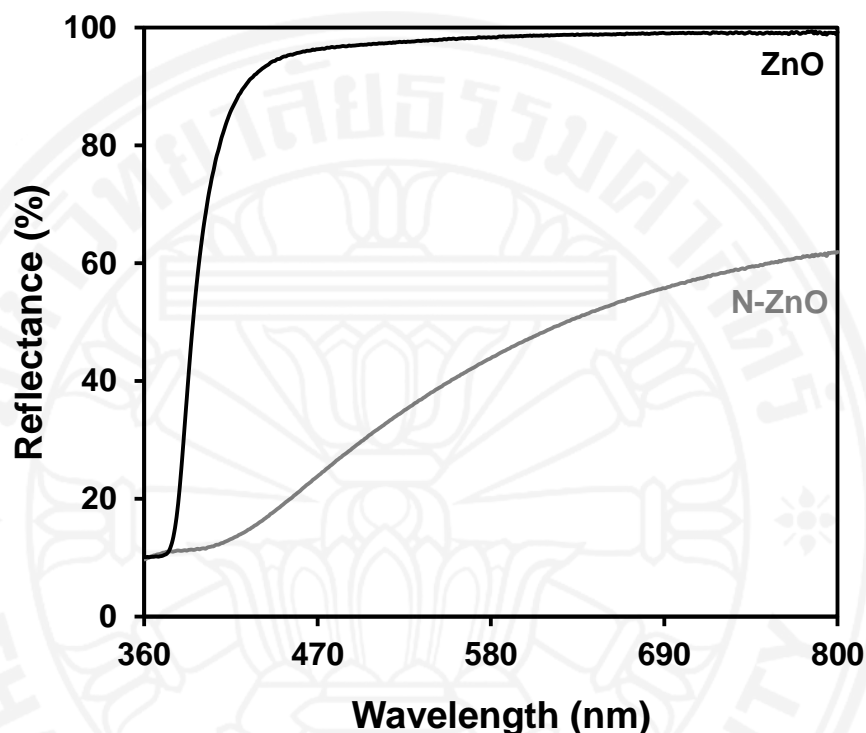
Figure 4.5 DRS spectra of ZnO and N-ZnO.

4.1.2.6 Chemical state of nitrogen

Figure 4.6(a) shows the high resolution N 1s XPS spectrum of the N-ZnO. There are two peaks at 397.8 and 400.4 eV. The peak at 397.8 eV corresponds to Zn-N bond, while that at 400.4 eV is due to N-O bond for the Zn-O-N state (Shifu et al., 2009). Furthermore, as shown in the N K-edge XANES spectrum of the N-ZnO (Figure 4.6(b)), there are two energy features originating from transitions 1s → π* of Zn-N (400.1 eV) and 1s → π* of N-O (403 eV) and higher energy features related to transitions 1s → σ*. The position and shape of 1s → π* resonances are different from those reported for N_2 gas measured using the same instrument, shown in Figure D1 (Nakajima et al., 2013). This indicates the absence of N_2 in the lattice structure of N-ZnO. Overall, the XANES and XPS spectra unambiguously prove the incorporation of N into the ZnO lattice in substitutional and interstitial modes.
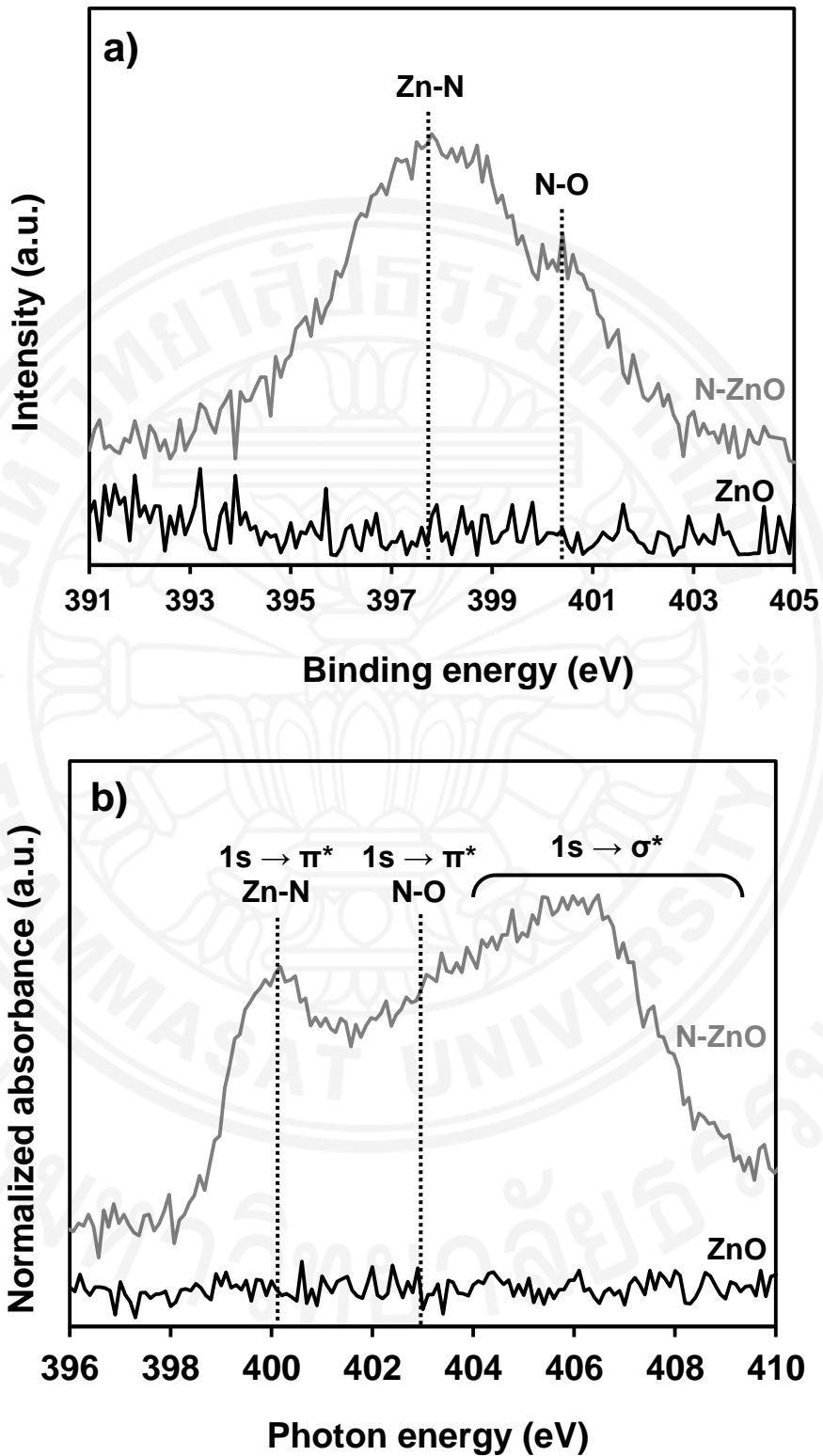
Figure 4.6 N 1s XPS spectra (a) and N *K*-edge XANES spectra (b) of ZnO and N-ZnO.

4.1.2.7 Textural properties

Table 4.3 summarizes the textural properties of the catalysts. The specific surface area (SSA) is determined using the Brunauer-Emmett-Teller (BET) method. The pore volume and pore diameter are calculated from the Barrett-Joyner-Halenda (BJH) method based on N_2 desorption isotherm. After urea addition, the SSA increases due to the decreased crystalline size as a result of the crystal growth inhibition by the urea. An increased SSA is advantageous for improving photocatalytic efficiency since photocatalysis is a surface phenomenon and the catalyst surface also plays a critical role in determining the adsorption extent of the targeted pollutants and the absorption of the incoming light. Furthermore, N-ZnO has a smaller average pore diameter as compared to ZnO (Table 4.3), but its pore volume is higher. These are probably due to the liberation of gases during the decomposition of zinc acetate-urea complex in the calcination process, creating more pores with smaller sizes. It is clearly seen that N doping has beneficially altered the textural properties of ZnO.
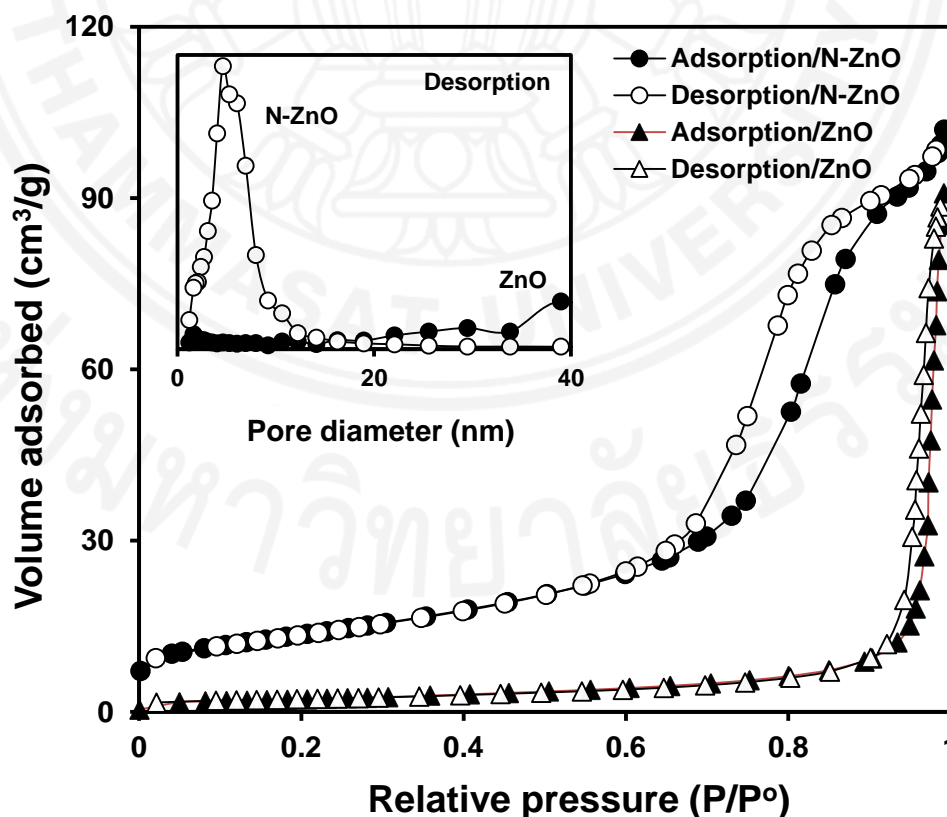
Figure 4.7 N_2 adsorption-desorption isotherms. The insert is pore size distribution curves of ZnO and N-ZnO.

Table 4.3 Textural properties of ZnO and N-ZnO.

Catalyst	Specific surface area (m^2/g)	Average pore diameter (nm)	Pore volume (cm^3/g)
ZnO	8	39.01	0.135
N-ZnO	46	4.61	0.157

4.1.3 Comparative dye degradation under visible and UVC light

Figure 4.8 shows the comparative dye degradation by ZnO, N-ZnO, c/ZnO, and c/N-ZnO. The photocatalytic degradation of the dyes is in the order of MB > R6G > AM. The photocatalytic degradation order might be associated with the complexity of the molecular structure of the dye. Particularly for AM, it is found to be the most difficult dye to degrade. This because the sulfonic groups of AM, as electron withdrawing groups, could reduce the electron density of the aromatic structure, making the aromatic structure less susceptible to the electrophilic attack by hydroxyl radical.
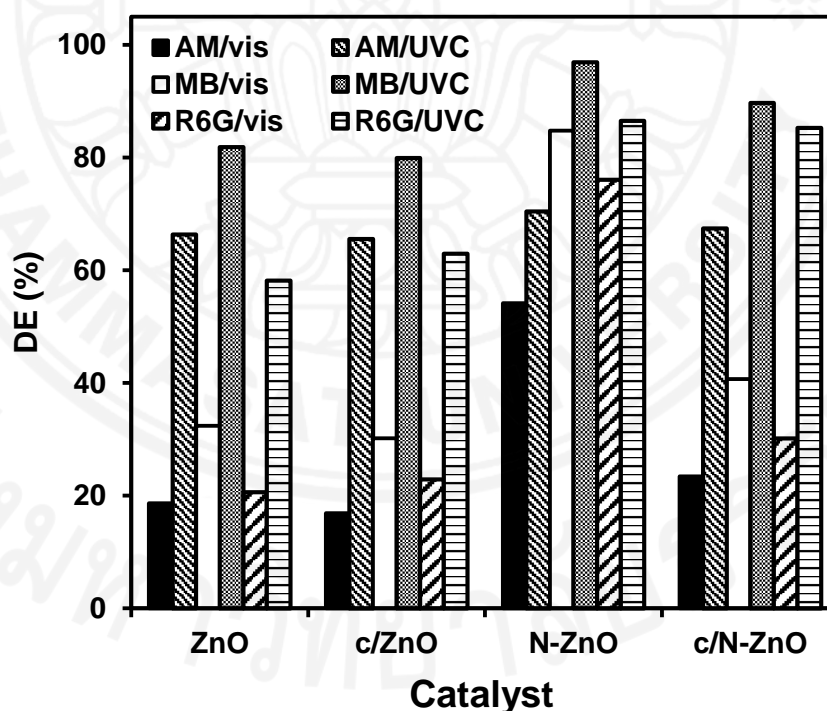
Figure 4.8 Efficiency of the ZnO-based catalysts for the dye degradation (W = 1 g/L, C_0 = 5 mg/L, pH = 7, t = 1 h, I_{vis} = 16.5 W/m^2, I_{UVC} = 3.5 W/m^2).

Comparing the pristine catalysts, they all have approximately the same photocatalytic activity. In all the cases, the doped ZnO has higher photocatalytic activity than the pristine ZnO counterpart for the degradation of particular dye using a

49

particular light source. This indicates that the photocatalytic activity of ZnO is improved by doping with N. Moreover, the photocatalytic activity of c/N-ZnO is found to be lower than that of N-ZnO. This is presumably due to ineffective incorporation of N in the ZnO lattice. In addition, the specific surface area of c/N-ZnO (12.45 m^2/g) is lower than that of N-ZnO (46.32 m^2/g). Furthermore, the enhancement of DE after N doping is more significant in the case of dye degradation under visible light. This is because according to the DRS spectra, the catalyst ability to absorb light in the visible region is greatly improved as compared to that in the UV region.

The dyes can be degraded by pristine ZnO under visible light, albeit a pristine ZnO is reported to be active only under UV light (Rehman et al., 2009). This fact can be attributed to the self-sensitization of dye (Yin et al., 2009). The adsorbed dye on the catalyst surface absorbed visible light for exciting its electrons and transferring them into the CB of the catalyst to generate reactive radicals. After losing its electrons, the dye becomes a radical cation and further undergoes degradation.

4.1.4 Effect of operating parameters on the dye degradation under visible light

The efficiency of photocatalytic degradation is known to be greatly affected by some key operating parameters such as dye concentration, catalyst concentration, pH, and salinity (Daneshvar et al., 2003). Thus, the effects of such parameters on the dye degradation by N-ZnO were evaluated and discussed in the subsequent sections.

4.1.4.1 Effect of dye concentration

As shown in Table 4.4, as the initial concentration increases from 5 to 25 mg/L, DE decreases from 93.2 to 64.1% after 1.5 h for MB degradation, from 91.3 to 70.1% after 4 h for AM degradation, and from 97.6 to 60.1% after 2.5 h for R6G degradation. It can be explained as follows. With increasing dye concentration, more dye absorb incoming light and more dye is also adsorbed on the catalyst surface. As a result, less photons are available for reaching the surface to produce reactive radicals.

Table 4.4 Dye degradation efficiency by N-ZnO at different operating parameters under visible light.

Parameter	Value	DE (%)			Fixed parameter
		MB	AM	R6G	
Dye concentration (mg/L)	5	93.2	91.3	97.6	$W = 1$ g/L, pH $= 7$, $t = 1.5$ h (MB); 4 h (AM); 2.5 h (R6G), $I_{vis} = 16.5$ W/m^2
	10	89.3	88.5	89.4	
	15	80.3	83.3	78.6	
	20	73.5	76.4	68.3	
	25	64.1	70.1	60.1	
Catalyst concentration (g/L)	0.5	72.4	73.8	71.3	$C_0 = 10$ mg/L, pH $= 7$, $t = 1.5$ h (MB); 4 h (AM); 2.5 h (R6G), $I_{vis} = 16.5$ W/m^2
	1	89.3	88.5	89.4	
	1.5	90.8	85.6	86.8	
	2	85.4	81.8	83.6	
	2.5	74.5	69.5	70.2	
pH	5	61.2	59.7	68.5	$W = 1$ g/L, $C_0 = 10$ mg/L, $t = 1.5$ h (MB); 4 h (AM); 2.5 h (R6G), $I_{vis} = 16.5$ W/m^2
	6	76.1	77.8	85.9	
	7	89.3	88.5	89.4	
	8	93.8	90.3	88.1	
	9	92.7	85.2	85.0	
Salinity (g/L NaCl)	0	89.3	88.5	89.4	$W = 1$ g/L, $C_0 = 10$ mg/L, pH $= 7$, $t = 1.5$ h (MB); 4 h (AM); 2.5 h (R6G), $I_{vis} = 16.5$ W/m^2
	0.3	90.9	90.3	88.6	
	0.6	92.4	91.4	86.1	
	1.2	93.1	88.2	82.2	
	4.8	84.5	86.7	78.8	
	9.6	81.8	77.8	73.2	

4.1.4.2 Effect of catalyst concentration

In the case of MB degradation, during 1.5 h of irradiation, DE increases from 72.4 to 90.8% as the catalyst concentration increases from 0.5 to 1.5 g/L. With further increasing of concentration to 2.5 g/L, DE slightly decreases to 74.5%. The same trends are also observed in the degradation of AM and R6G. The optimum catalyst concentration for AM and R6G is found to be 1 g/L, while that for MB is 1.5 g/L. The difference in the optimum catalyst concentration can be attributed to the difference in the dye properties, such as solubility in water, adsorbability on the catalyst surface, and absorbability towards incoming light.

Explaining the present results, at low catalyst concentration, the absorption of light governs the reaction extent due to limited catalyst surface area. Thus, with increasing catalyst concentration and total catalyst surface area, DE increases up to a certain level. At higher concentrations beyond the optimum level, light scattering and

51

shielding by the catalyst particles significantly reduce the light penetration into the suspension and hence DE starts decreasing.

4.1.4.3 Effect of pH

As shown in Table 4.4, in the case of MB degradation, DE increases from 61.2 to 93.8% when the pH increases from 5 to 8. With further increasing pH to 9, DE slightly decreases to 92.7%. Interestingly, the same trend in the DE is observed for the degradation of AM and R6G. The optimum pH for the degradation of AM and R6G are found to be 8 and 7, respectively.

In fact, elucidating the effect of pH on the dye degradation efficiency is quite tricky since it has multiple roles. It is known that due to amphoteric behavior, the suspension pH easily trigger the dissociation of -OH groups leading to coverage with both negatively charged and positively charged species (Uddin et al., 2007). Therefore, the adsorption of a cationic dye, for instance, is favorable in the alkaline condition as the catalyst surface is negatively charged, and vice versa. However, in the present study, the same trend of DE is observed for all dyes although their ionic states in aqueous suspension are different. MB and R6G are cationic dyes, while AM is an anionic dye.

To explain the present results, several factors should be taken into account. At low pH, DE is low since more H^+ is available for the adsorption to cover the catalyst surface; thereby reducing the generation of reactive radicals. Additionally for AM, the low DE might be ascribed to the decrease of electron densities at -N=N- group due to an excess of H^+ interacting with this chromophore (Shanthi & Kuzhalosai, 2012). This makes the chromophore less susceptible to electrophilic attack by the reactive radicals. The dissolution of ZnO under acidic condition is also reported to give an adverse effect to the photocatalytic activity (Bahnemann et al., 1987; Behnajady et al., 2006). As pH increases to 8, DE then increases due to the high availability of OH^- reacting with photogenerated holes to form more •OH radicals. With further increasing pH to 9, DE somewhat decreases. This result might be appropriately explained on the basis of zero point charge pH (pH_{ZPC}). The pH_{ZPC} of N-ZnO was determined to be 9.2 (Figure 4.9). When the suspension pH is around 9, which is close to pH_{ZPC}, the neutral charge of catalyst surface cannot generate interactive rejection

for solid-liquid separation. This can induce aggregation of catalyst particles and diminishes the total surface sites available for the adsorption of dye and the absorption of light.
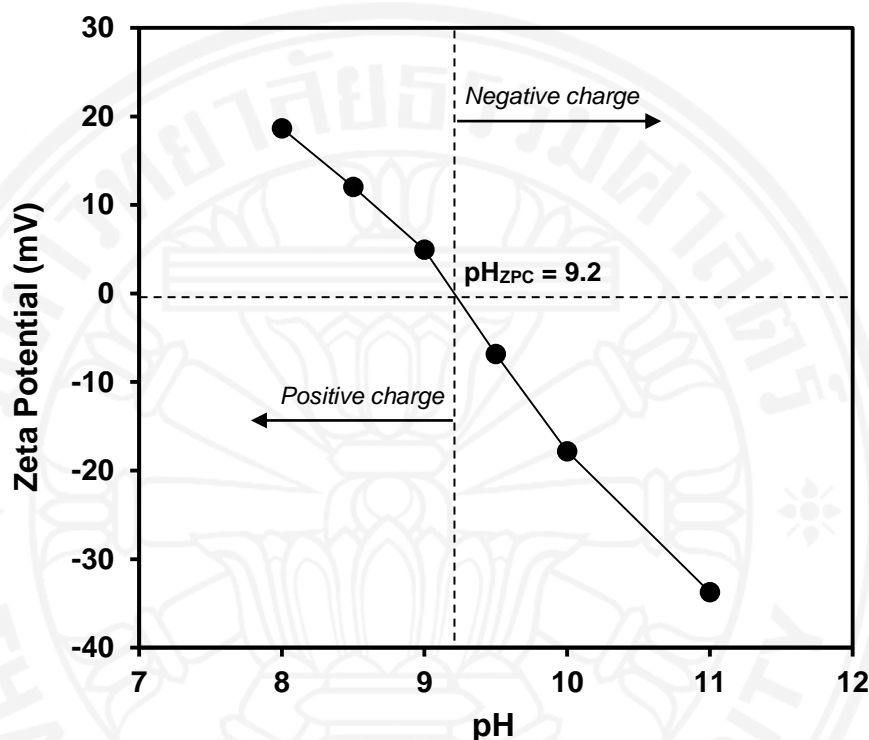
Figure 4.9 Zeta-potentials of N-ZnO suspended in water as a function of pH.

4.1.4.4 Effect of salinity

Dye wastewaters are characterized by high concentrations of salt components such as Cl^- ion (Wang et al., 2011b). Therefore, the effect of salinity on the photocatalytic process efficiency should be studied. It is observed that, for MB degradation, as NaCl concentration increases from 0.3 to 1.2 g/L, DE increases from 90.9 to 93.1%. Interestingly, DE then decreases to 81.8% with an increase in NaCl concentration to 9.6 g/L. The same trend is also observed for AM degradation and the optimum concentration of NaCl is found to be 0.6 g/L.

The dual effect of salinity has previously been reported on the advanced oxidation processes for degradation of organic compounds (Wang et al., 2011b; Yang et al., 2005; Yuan et al., 2011; Yuan et al., 2012). At relatively low salinity, the presence of •Cl radical formed as a result of surface chain-transfer reaction of Cl^- is

beneficial. This radical possesses a relatively high oxidation potential (2.47 V) and is able to oxidize organic substances (Hirakawa & Nosaka, 2002). Besides, its high affinity for a hole can also prevent electron-hole recombination (Yang et al., 2005). However, with increasing the salinity beyond the optimum level, there is a significant competition between Cl^- and the dye molecules for the limited catalyst surface, leading to catalyst deactivation (Konstantinou & Albanis, 2004b).

Interestingly, the effect of salinity on the degradation of R6G is different than those of MB and AM. It seems that effect of salinity on organic compound degradation cannot be generalized. It would depend on the properties of organic compound in the suspension system. However, one can conclude that high salinity of the suspension system is detrimental to the dye degradation.

It is also important noting that Na^+ may be capable of inhibiting the dye degradation due to the adsorption of Na^+ on the catalyst surface. This prevents the dye molecules from accessing the active sites (site-blocking effect) and reduces the absorption of the incoming light by the catalyst.

4.1.5 Effect of operating parameters on the dye degradation under UVC light

The dye degradation using N-ZnO is also carried out under UVC light for comparison. The trends in the effect of operating parameters under UVC light are very similar to those under visible light (Table 4.5). However, it takes less time to achieve the same value of DE because the maximum absorption peak of N-ZnO is still in the UV region. Thus, UV light is more strongly absorbed instead of visible light. In addition, electrons and holes generated by UVC light have stronger reduction and oxidation power compared to those generated by visible light. The minor difference in the effect of operating parameters can also be due to the difference in the dye degradation mechanism. Under visible light, self-photosensitized degradation of dye occurs. Although N-ZnO is more effectively used to degrade the dye under UVC light, it was proven to be active under visible light. Thus, sunlight consisting of 46% visible light can be used as a radiation source to activate the catalyst for practical applications (Rehman et al., 2009).

Table 4.5 Dye degradation efficiency by N-ZnO at different operating parameters under UVC light.

Parameter	Value	DE (%)			Fixed parameter
		MB	AM	R6G	
Dye concentration (mg/L)	5	90.3	90.1	98.7	W = 1 g/L, pH = 7, t = 0.8 h (MB); 2 h (AM); 2 h (R6G), I_{UVC} = 3.5 W/m^2
	10	82.4	83.6	92.3	
	15	75.5	77.4	84.6	
	20	67.3	70.2	76.4	
	25	60.1	66.3	68.4	
Catalyst concentration (g/L)	0.5	68.3	69.1	70.2	C_0 = 10 mg/L, pH = 7, t = 0.8 h (MB); 2 h (AM); 2 h (R6G), I_{UVC} = 3.5 W/m^2
	1	82.4	83.6	92.3	
	1.5	85.6	81.7	93.3	
	2	79.7	70.1	86.5	
	2.5	64.8	65.8	78.6	
pH	5	52.7	41.5	84.1	W = 1 g/L, C_0 = 10 mg/L, t = 0.8 h (MB); 2 h (AM); 2 h (R6G), I_{UVC} = 3.5 W/m^2
	6	75.2	67.3	89.4	
	7	82.4	83.6	92.3	
	8	84.1	84.7	94.1	
	9	80.5	83.1	92.1	
Salinity (g/L NaCl)	0	82.4	83.6	92.3	W = 1 g/L, C_0 = 10 mg/L, pH = 7, t = 0.8 h (MB); 2 h (AM); 2 h (R6G, I_{UVC} = 3.5 W/m^2
	0.3	83.5	85.1	90.5	
	0.6	86.3	89.2	88.7	
	1.2	85.7	86.5	84.4	
	4.8	80.2	84.3	78.1	
	9.6	75.8	78.8	73.7	

4.1.6 Effect of H$_2$O$_2$ concentration on the R6G degradation

As previously explained, one of the important factors for efficient photocatalysis is preventing electron-hole recombination. Studies suggest that H$_2$O$_2$ can act as an electron acceptor, which is better than O$_2$ (Chu & Wong, 2004). Thus, such recombination can be prevented and the photocatalytic efficiency is then enhanced. For the degradation of R6G by N-ZnO, DE increases from 65.7 to 78.2% as H$_2$O$_2$ concentration increases from 0.1 to 0.7 g/L (Table 4.6). The enhancement of DE after H$_2$O$_2$ addition can be due to the consumption of the photogenerated electrons by H$_2$O$_2$ producing •OH radical (Eq. 4.1). Thus, electron-hole recombination is prevented and at the same time additional •OH is generated. The added H$_2$O$_2$ can also produce •OH by reacting with •O$_2^-$ (Eq. 4.2). However, under visible light, it is not possible to generate •OH from the direct dissociation of H$_2$O$_2$ as H$_2$O$_2$ does not absorb visible light. It should be noted that the H$_2$O$_2$ adsorbed on the catalyst surface may also form surface complexes that extend the photoresponse of the catalyst to the visible region, as evident in the case of UV/TiO$_2$ system reported elsewhere (Li et al., 2001). It is

postulated that the electron transfer process from surface complexes to the CB of the catalyst leads to the reaction between transferred electron and the surface adsorbed H_2O_2 forming additional •OH (Doong & Chang, 1998).

$$H_2O_2 + e^- \rightarrow •OH + OH^- \qquad (4.1)$$

$$H_2O_2 + •O_2^- \rightarrow •OH + OH^- + O_2 \qquad (4.2)$$

Furthermore, it is found that the enhancement of DE becomes insignificant with increasing H_2O_2 concentration. This is most likely due to the reaction of H_2O_2 with •OH (Eq. 4.3) (Dionysiou et al., 2000b) or with photogenerated holes (Eq. 4.4) (Doong & Chang, 1998), forming •HO_2 radical which possesses much lower oxidation potential compared to •OH.

$$H_2O_2 + •OH \rightarrow H_2O + •HO_2 \qquad (4.3)$$

$$H_2O_2 + h^+ \rightarrow H^+ + •HO_2 \qquad (4.4)$$

Table 4.6 Dye degradation efficiency by N-ZnO at different concentration of H_2O_2.

H_2O_2 concentration (g/L)	DE (%)		Fixed parameter
	Visible	UVC	
0	60.1	70.4	$W = 1$ g/L, $C_0 = 25$ mg/L,
0.1	65.7	78.3	pH = 7, $t = 2$ h, $I_{vis} = 16.5$
0.3	70.8	82.1	W/m², $I_{UVC} = 3.5$ W/m²
0.5	77.1	96.5	
0.7	78.2	98.2	

4.1.7 Role of reactive species on the degradation of R6G by N-ZnO

It must be noted that the photocatalytic activity of the catalyst depends on not only the light absorption ability, but also the type of the reactive species produced. This is because reactive species have different oxidation and reduction potential. To elucidate the role of reactive species during the degradation of R6G, the quenching technique with chemical quenchers is employed (Antonopoulou et al., 2013). The kinetics plots for pseudo first order reaction of R6G degradation by N-ZnO with visible and UVC light in the presence of quencher are shown in Figures 4.10-4.11. The ability of the quenchers to reduce k_{app} is different in the two cases, under visible and UVC light. It is seen that the role of reactive species depends on the type of light source applied

56

because it determines the dye degradation mechanism and the reactive species formation.

As summarized in Table 4.7, less oxidative species such as superoxide radical ($\bullet O_2^-$) and singlet oxygen ($^1O_2$) are predominant in the degradation of R6G under visible light. In contrast, highly oxidative $\bullet OH$ radicals are present under UVC light. These are because the dye degradation under visible light proceeds mainly through self-sensitization mechanism. The holes photogenerated under visible light in the N mid-band state of the catalyst also do not have suitable reduction potential to produce $\bullet OH$ radical by the oxidation of H_2O although they can oxidize $\bullet O_2^-$ to form $^1O_2$ (Figure 4.12). In the visible/N-ZnO system, $\bullet O_2^-$ is the most dominant reactive species. It can be understood that extra electrons are available in the CB of N-ZnO as a result of electron transfer through self-sensitization of R6B.
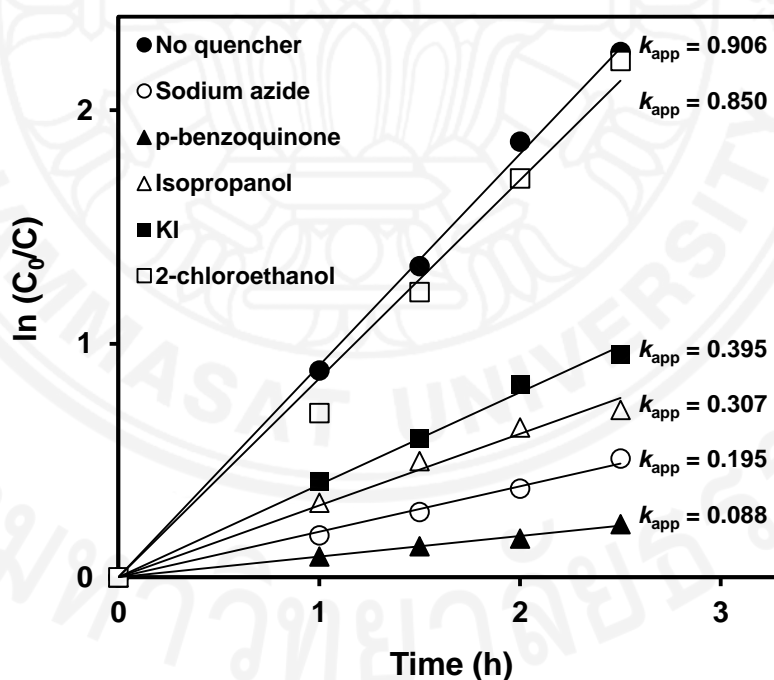
Figure 4.10 The kinetics plots for pseudo first order reaction of R6G degradation by N-ZnO under visible light in the presence of quencher ($I_{vis} = 16.5$ W/m^2, $C_0 = 10$ mg/L, $W = 1$ g/L, pH = 7).
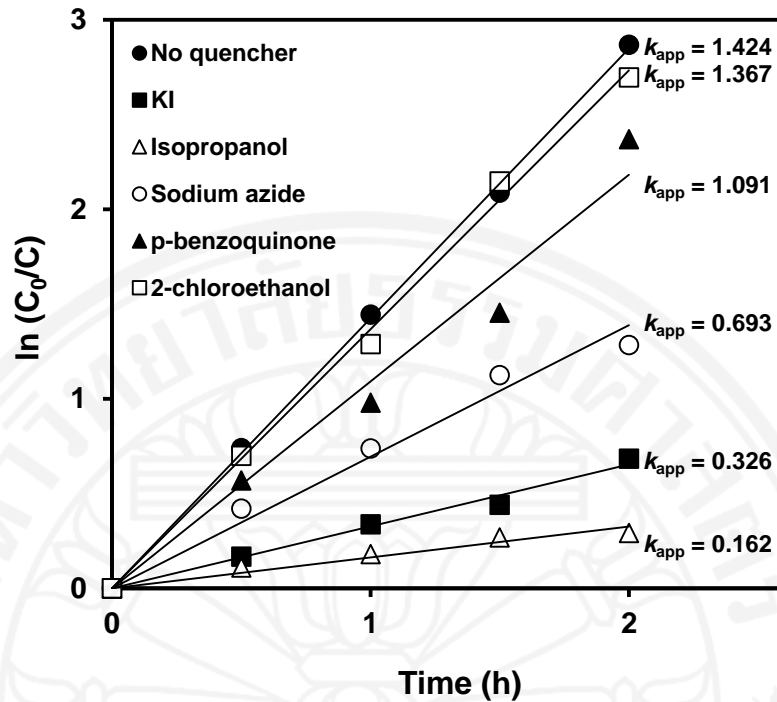
Figure 4.11 The kinetics plots for pseudo first order reaction of R6G degradation by N-ZnO under UVC light in the presence of quencher (I_{UVC} = 3.5 W/m^2, C_0 = 10 mg/L, W = 1 g/L, pH = 7).

Table 4.7 The k_{app} of R6G degradation by N-ZnO in the presence of quenchers.

Quencher	Quenched reactive species	k_{app} (h^{-1}); RS (%)	
		vis1/N-ZnO	UVC/N-ZnO
No quencher		0.906; -	1.424; -
KI	h$^+$	0.395; 56.3	0.326; 77.0
Isopropanol	•OH	0.307; 66.1	0.162; 88.5
Sodium azide	$^1O_2$	0.195; 78.5	0.693; 51.3
2-chloroethanol	e$^-$	0.850; 6.2	1.367; 4.0
p-benzoquinone	•O$_2^-$	0.088; 90.2	1.091; 23.3

W = 1 g/L, C_0 = 10 mg/L, pH = 7, I_{vis} = 16.5 W/m^2, I_{UVC} = 3.5 W/m^2.
The role of reactive species is in the following order:
vis/N-ZnO: •O$_2^-$ > $^1O_2$ > •OH > h$^+$ > e$^-$.
UVC/N-ZnO: •OH > h$^+$ > $^1O_2$ > •O$_2^-$ > e$^-$.

58
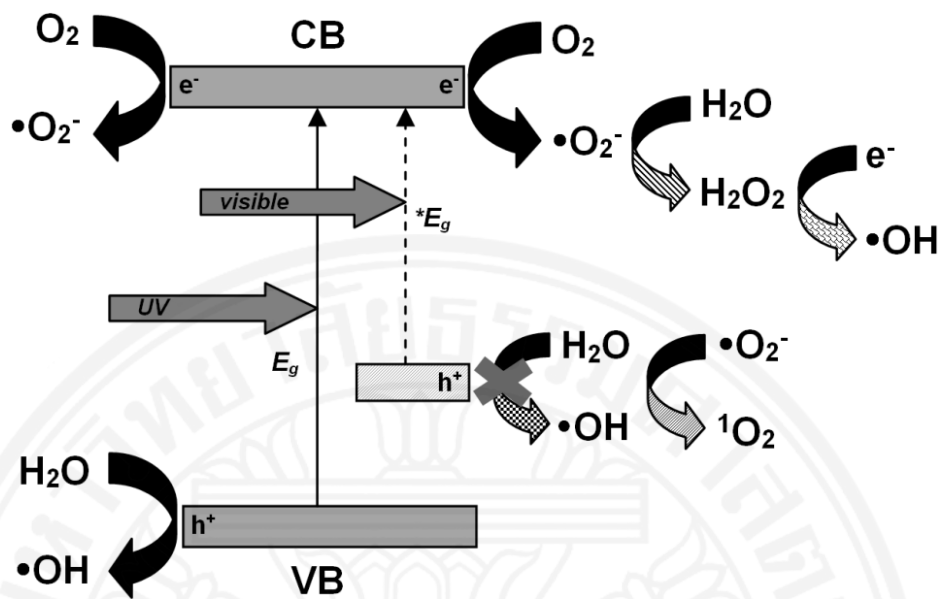
Figure 4.12 Mechanism of reactive species formation in the N-ZnO under visible or
UV light.

Comparing the role of reactive species under UVC light, •OH is found to be
the most dominant reactive species. The photogenerated h^+ also seems to play an
important role in the dye degradation through direct attack of R6G on the catalyst
surface. In all the cases, the role of photogenerated electrons is negligible.

4.1.8 Catalyst reusability

As shown in Table 4.8, there were no significant decreases of photocatalytic activity
in six successive runs. The DEs were found to decrease by less than 10% of the
original values. These minor decreases of DE over time might be due to formation of
inert $Zn(OH)_2$ surface layers (Rao et al., 1980) or deposition of dye degradation
products. Furthermore, the N-ZnO catalyst is found to be stable because of its
relatively high crystallinity. On the basis of TN measurement, N-containing
compounds are also not observed in the solution above the detection limit of the
instrument. Indeed, N dopants within N-doped metal oxides is relatively stable
(Quesada-Cabrera et al., 2014).

Table 4.8 Reusability of N-ZnO for the dye degradation.

Light source	Dye	Irradiation time (h)	DE (%)					
			1st run	2nd run	3rd run	4th run	5th run	6th run
Visible	MB	1.5	88.6	87.3	86.6	84.4	83.2	83.1
	AM	4	88.3	87.2	86.8	85.9	83.8	83.3
	R6G	2.5	89.4	87.6	86.4	81.2	80.8	76.3
UVC	MB	0.8	82.5	81.8	81.2	81.0	76.9	75.6
	AM	2	83.6	82.5	82.3	81.9	80.3	79.8
	R6G	2	94.3	91.8	93.5	88.2	85.7	82.6

$W = 1$ g/L, $C_0 = 10$ mg/L, pH = 7, $I_{vis} = 16.5$ W/m^2, $I_{UVC} = 3.5$ W/m^2.

4.1.9 Toxicity evaluation

It is likely that the dye degradation by-products still exist when complete dye decolorization is achieved. They may be more toxic than the parent compounds and thus cannot be discharged to the environment directly. To further verify this, toxicity evaluation of the photocatalytically treated AM and MB solutions against *Bacillus cereus* (Aftab et al., 2011), is undertaken with the REMA plate method (Palomino et al., 2002). The results show no inhibition for the dye solutions treated with N-ZnO for 2 h (AM) and 4 h (MB) of UVC light irradiation (Table 4.9).

Table 4.9 Comparative bacterial inhibition by the dye solutions photocatalytically treated with N-ZnO.

	Inhibition (%)	
	AM	MB
Initial	8.13	3.52
Final	No inhibition	No inhibition

The initial dye concentration is 10 mg/L and the final MB and AM concentrations are 1.07 and 1.15 mg/L, respectively.

4.2 Dye degradation by N-ZrO$_2$

4.2.1 Photocatalytic activity of N-ZrO$_2$ synthesized with different amounts of urea

As can be seen in Table 4.10, DE increases with the increase in the amount of urea used. It is obvious that urea plays a critical role in the enhancement of photocatalytic activity. This may be attributed to doping of N into the catalyst structure which then beneficially modify the catalyst properties. For further clarification, characterization is undertaken for the N-ZrO$_2$ with U/Z of 2 as well as pristine ZrO$_2$ for comparison.

Table 4.10 DE of the N-ZrO$_2$ catalysts synthesized with different amounts of urea.

Light source	Dye	Irradiation time (h)	DE (%)				
			U/Z = 0	U/Z = 0.25	U/Z = 0.5	U/Z = 1	U/Z = 2
Visible	MB	4	6.56	13.3	30.5	42.9	50.1
	AM	4	4.43	12.0	14.7	21.7	26.4
	R6G	4	15.5	23.8	33.8	36.8	40.3
UVC	MB	4	88.1	95.2	97.6	100	100
	AM	4	70.1	73.5	76.1	77.0	84.5
	R6G	3.2	78.0	85.6	88.2	91.9	92.3

C_0 = 10 mg/L, W = 1 g/L, pH = 7, I_{vis} = 16.5 W/m^2, I_{UVC} = 3.5 W/m^2.

4.2.2 Properties of N-ZrO$_2$

4.2.2.1 Crystallinity and structural properties

The XRD patterns of ZrO$_2$ and N-ZrO$_2$ are shown in Figure 4.13. The diffraction patterns can be indexed to monoclinic ZrO$_2$ (JCPDS No.37-1484). No extra peaks of unwanted impurities are observed, suggesting that the catalysts have a single phase with high purity. The diffraction peaks are also sharp, indicating high crystallinity of the catalyst. The formation of ZrO$_2$ with pure monoclinic phase is of paramount significance of the present study, as the synthesis of ZrO$_2$ mainly results in mixed phases (Navio et al., 2001).

After adding urea, the crystalline size decreases, resulting in peak broadening. The crystallinity also slightly decreases, likely due to crystal defects, crystal growth inhibition by the urea, or due to the substitution of O by N. As a result, the peak intensities are reduced. Using the Scherrer equation (λ of 0.15406 and K of 0.91), the crystalline sizes are determined to be 46.32 and 37.38 nm for ZrO$_2$ and N-ZrO$_2$,

respectively. Furthermore, the shift of several peaks to lower diffraction angles indicates an increase of the crystal plane spacing and may also be attributed to incorporation of N within the ZrO_2 lattice. The incorporation of N does not lead to the formation of other crystalline phases. N atoms seem to be highly soluble in the lattice structure.
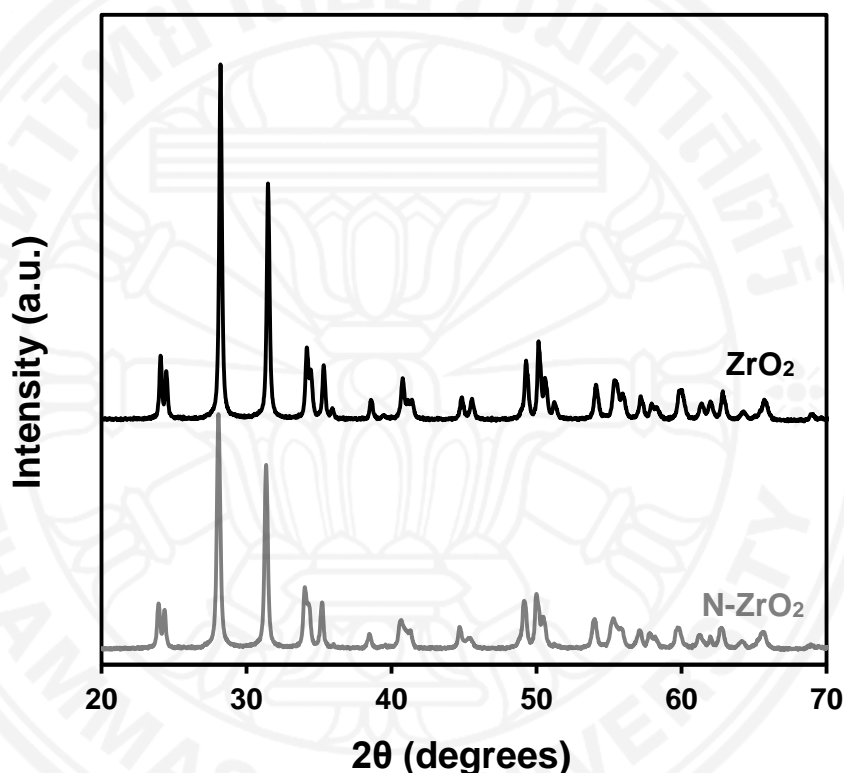
Figure 4.13 XRD patterns of ZrO_2 and N-ZrO_2.

4.2.2.2 Vibrational spectroscopy

Figure 4.14 shows the FTIR spectra of ZrO_2 and N-ZrO_2. The peaks at 584 cm^{-1} and 497 cm^{-1} are attributed to the metal and oxygen bond (Zr-O) and metal, oxygen, and metal bond (Zr-O-Zr), respectively (Matos et al., 2009). The peaks at around 1240-1380 cm^{-1} correspond to the metal and hydroxide bond (Zr-OH). Furthermore, the peaks at around 2368-2370 cm^{-1} are due to the presence of adsorbed CO_2. As can be seen, additional peaks are observed after doping with N. The peaks noticed at around 700-850 cm^{-1} are associated with the wagging vibration of N-H bonds, while those at 1450-1550 cm^{-1} are of bending mode. The presence of these new functional groups may be advantageous for improving the adsorption ability of the catalyst.
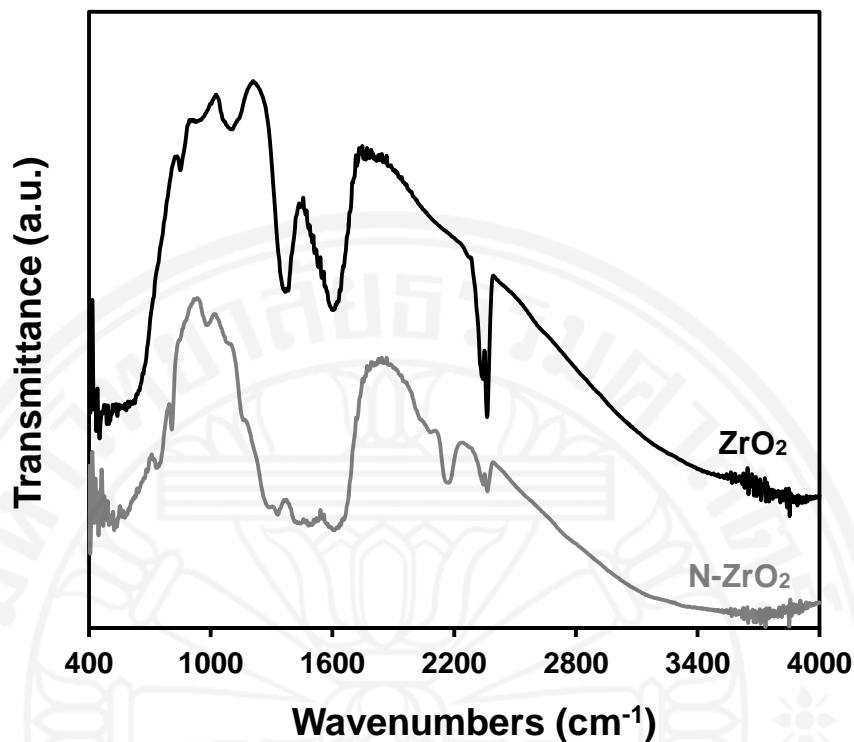
Figure 4.14 FTIR spectra of ZrO_2 and N-ZrO_2.

4.2.2.3 Thermal properties

The thermogram of ZrO_2 and N-ZrO_2 reveal initial weight loss of about 3% corresponding to temperature up to 500 °C (Figure 4.15). This weight loss could be due to water removal on the catalyst surface and the catalyst pores. Moreover, small weight loss is found from 580 to 700 °C, likely due to the decomposition of surface hydroxyl groups (Aimable et al., 2010). More water is adsorbed by N-ZrO_2 compared to pristine ZrO_2. This may be an indication of higher surface area and higher availability of surface functional groups in N-ZrO_2.
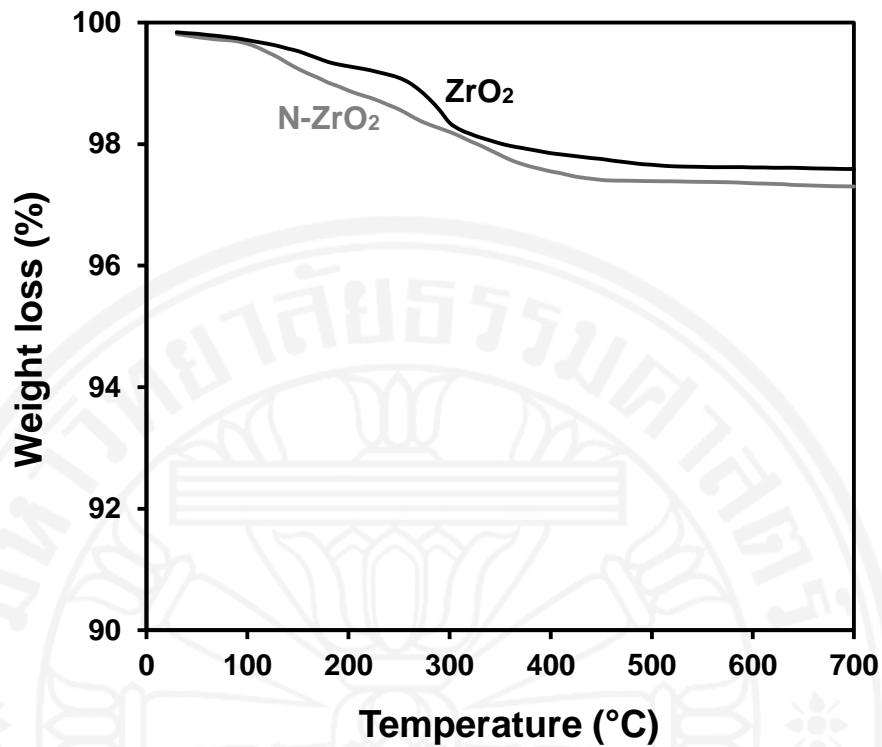
Figure 4.15 Thermogram of ZrO_2 and N-ZrO_2.

4.2.2.4 Morphological properties

The aggregate structure of N-ZrO_2 particles is observed (Figure 4.16(a)). According to TEM, diameter of primary particles in the range of 30-60 nm (Figure 4.16(b)). The structure of N-ZrO_2 particles is of zero-dimensional. As seen in Figure 4.16(c), the lattice fringes with 0.28 nm are clearly identified, corresponding to d spacing of monoclinic ZrO_2 [111] plane.

| Microscope | Accelerating Voltage | Magnification | Camera Length | - |
| JEM-2100 | 200 kV | 800000 x | - | ——10 nm—— |
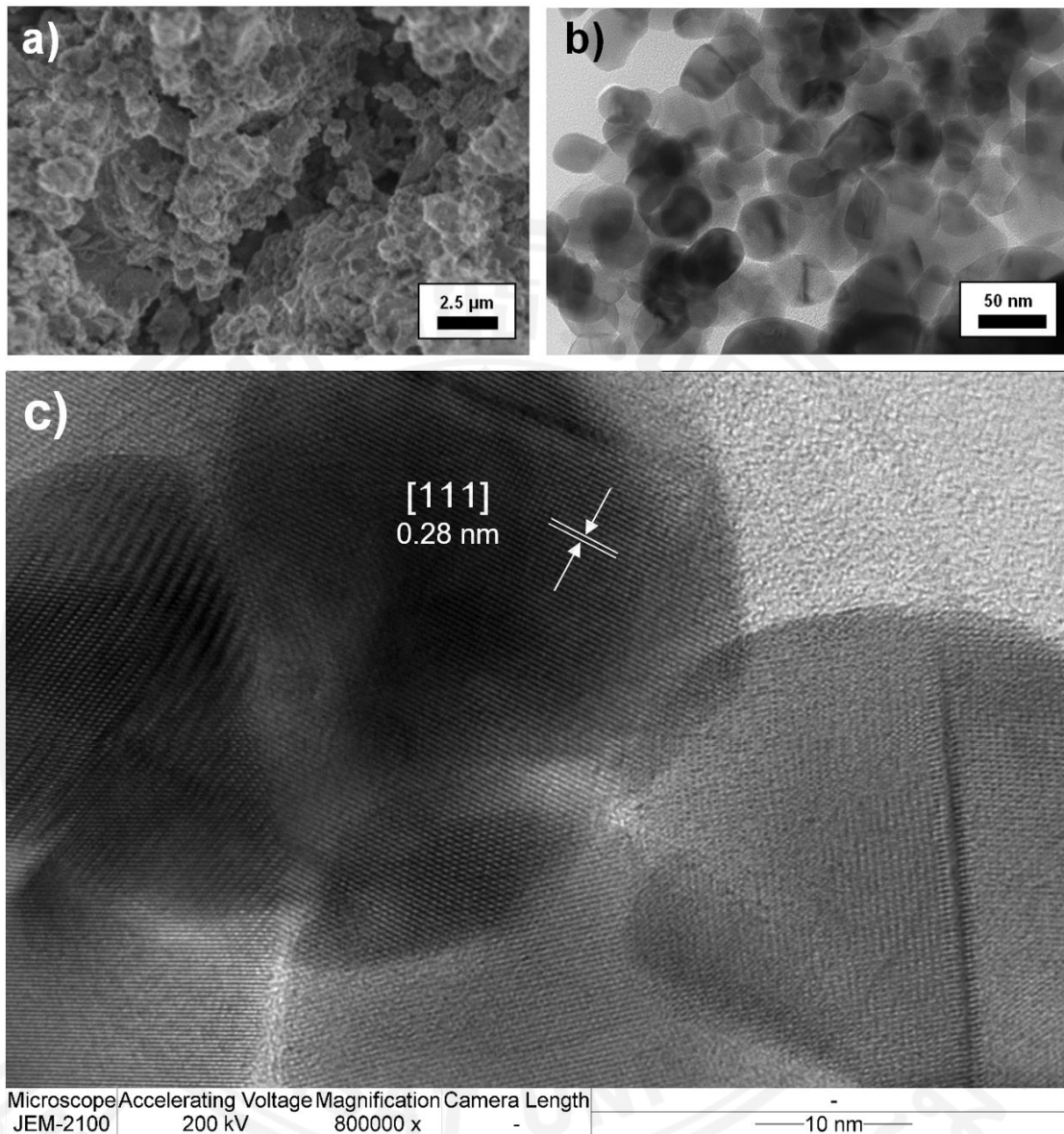
Figure 4.16 SEM (a), TEM (b), and HR-TEM (c) images of N-ZrO$_2$.

4.2.2.5 Optical properties

As shown in Figure 4.17, N doping enables extension of spectral response up to the NIR region with additional strong peak at around 330 nm. This can be due to the formation of a mid-band state by N 2p orbital within the band gap and the presence of oxygen defect states such as O$_v$. Not only extending the spectral response, N doping also makes the doped catalyst visible light active. This is because N 2p and O$_v$ can act as electron traps which suppress the electron-hole recombination.
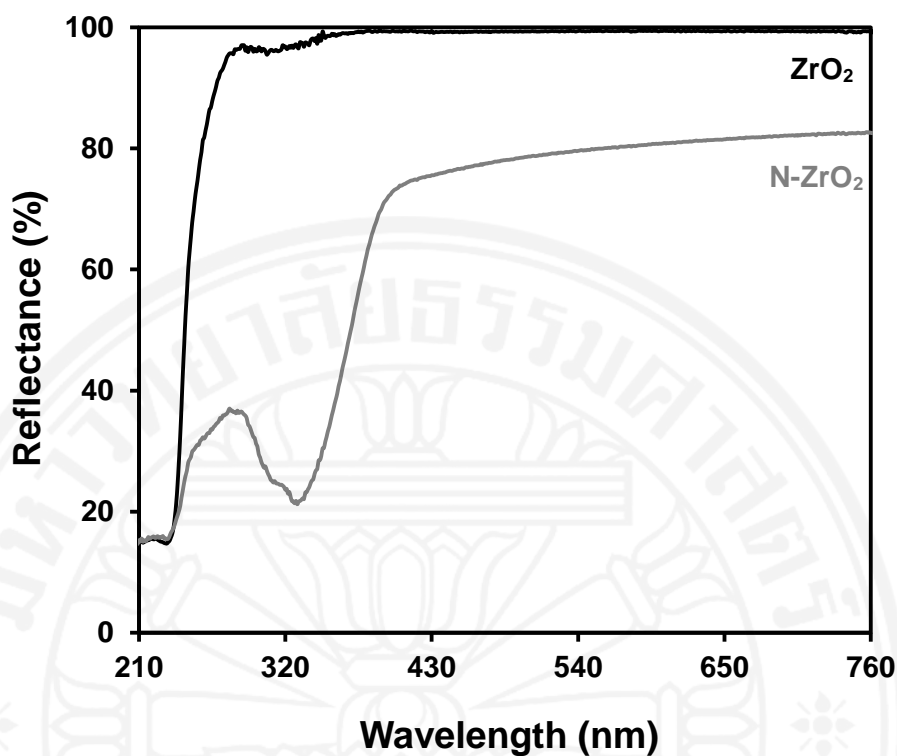
Figure 4.17 DRS spectra of the catalysts.

4.2.2.6 Chemical state of nitrogen

The high resolution XPS spectra of N 1s region of ZrO_2 and N-ZrO_2 are shown in Figure 4.18a. There is one main peak centered at 396.8 eV in the XPS spectrum of N-ZrO_2, corresponding to the Zr-N bond (Milošev et al., 1996). An additional peak at higher (400 eV) binding energy compared to the main peak is also seen. This characteristic peak is assigned to the N-O bond for the Zr-O-N state (Milošev et al., 1997). Furthermore, as shown in the N K-edge XANES spectrum of N-ZrO_2 (Fig. 4.18b), two energy features at 399 and 402 eV are observed, reflecting transitions 1s $\rightarrow \pi^*$ of Zr-N and 1s $\rightarrow \pi^*$ of N-O, respectively. Broad energy features at around 405 eV are also present, corresponding to transitions 1s $\rightarrow \sigma^*$. Similar with N-ZnO, the position and shape of 1s $\rightarrow \pi^*$ resonances of N-ZrO_2 are also different from those reported for N_2 gas shown in Figure D1 (Nakajima et al., 2013), indicating that N_2 molecules do not exist in the lattice structure.
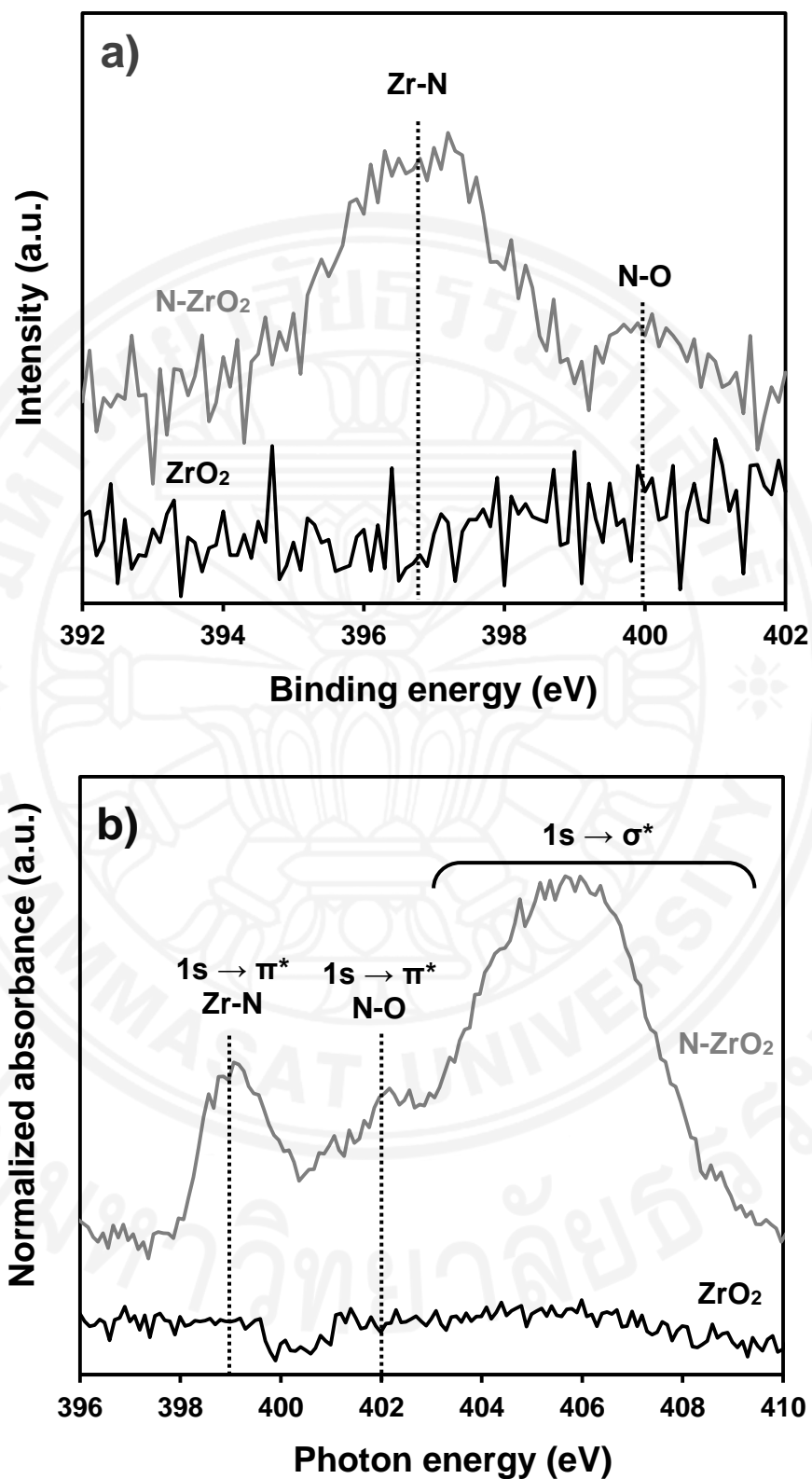
Figure 4.18 N 1s XPS spectra (a) and N K-edge XANES spectra (b) of ZrO_2 and N-ZrO_2.

4.2.2.7 Textural properties

The textural properties of ZrO_2 and N-ZrO_2 are presented in Figure 4.19. N-ZrO_2 possesses a higher SSA and higher pore volume, but lower average pore diameter than ZrO_2. The increased SSA after adding urea is probably due to the decreased crystalline size or due to the formation of more pores with smaller sizes as a result of gases liberation during the decomposition of zirconium hydroxide-urea complex in the calcination process.
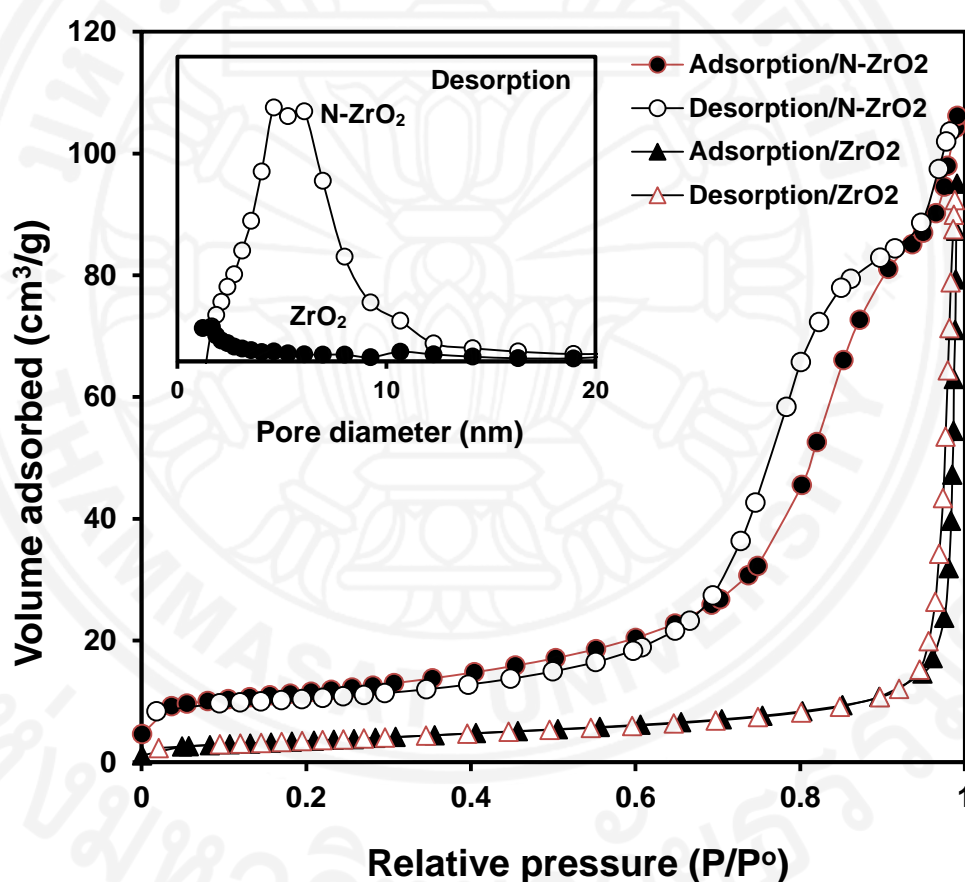
Figure 4.19 N_2 adsorption-desorption isotherms of ZrO_2 and N-ZrO_2. The insert is pore size distribution curves of ZrO_2 and N-ZrO_2.

Table 4.11 Textural properties of ZrO_2 and N-ZrO_2.

Photo catalyst	Specific surface area (m^2/g)	Average pore diameter (nm)	Pore volume (cm^3/g)
ZrO_2	9	71.31	0.144
N-ZrO_2	37	4.62	0.164

4.2.3 Comparative dye degradation under visible, UVC, and UVA light

The comparative degradation of MB and AM by ZrO_2, $N\text{-}ZrO_2$, c/ZrO_2, and $c/N\text{-}ZrO_2$ are summarized in Table 4.12. The trend is generally the same with the degradation of dyes by ZnO-based catalysts. The photocatalytic degradation order of the dyes is MB > R6G > AM. The photocatalytic activity of ZrO_2 is found to be higher than that of c/ZrO_2. This can be attributed to the difference in the specific surface area. The specific surface area of ZrO_2 (9.79 m^2/g) is slightly higher than that of c/ZrO_2 (7.83 m^2/g). Therefore, ZrO_2 can adsorb more dyes. As expected, the doped ZrO_2 catalysts show better photocatalytic activity than the pristine counterpart due to doping with N. Moreover, $c/N\text{-}ZrO_2$ exhibits lower photocatalytic activity than $N\text{-}ZrO_2$. This can be due to ineffective incorporation of N in the ZrO_2 lattice and lower specific surface area of $c/N\text{-}ZrO_2$ (11.1 m^2/g) as compared to that of $N\text{-}ZrO_2$ (37.62 m^2/g).

Table 4.12 Catalyst efficiency for the degradation of dyes by ZrO_2–based catalysts under different light sources.

Dye	Catalyst	DE (%)			
		vis1	vis2	UVC	UVA
MB	ZrO_2	6.6	10.2	88.1	56.9
	c/ZrO_2	4.8	9.4	80.8	52.4
	$N\text{-}ZrO_2$	50.1	91.2	100	100
	$c/N\text{-}ZrO_2$	24.6	60.5	95.6	60.5
AM	ZrO_2	4.4	6.8	70.1	43.5
	c/ZrO_2	3.7	6.4	63.4	52.7
	$N\text{-}ZrO_2$	26.5	60.9	84.5	100
	$c/N\text{-}ZrO_2$	9.5	14.1	80.5	51.3
R6G	ZrO_2	2.4	5.3	61.5	57.4
	c/ZrO_2	2.8	6.7	59.3	55.8
	$N\text{-}ZrO_2$	24.5	51.0	76.5	93.5
	$c/N\text{-}ZrO_2$	6.8	12.3	72.7	40.6

C_0 = 10 mg/L, W = 1 g/L, pH = 7, t = 4 h (AM and MB); 2 h (R6G), vis1 = visible light with an intensity of 16.5 W/m^2, vis2 = visible light with an intensity of 144.7 W/m^2.

In order to evaluate the effect of visible light intensity and UV light wavelength on the dye degradation, similar experiments with a higher visible light intensity (144.7 W/m^2) and longer UV light wavelength (315 < λ < 400 nm; UVA) are also carried out. As can be seen in Table 4.13, in all the cases, DE increases when a higher visible light intensity is applied. This may be because more radiation falls on

the catalyst surface for generating electron-hole pairs and ultimately more reactive radicals are produced. Significant increases of DE are found in N-ZrO$_2$ since it is able to absorb light in the visible region. Moreover, when UVA light is applied instead of UVC light, DE decreases, except for N-ZrO$_2$. This is most likely because N-ZrO$_2$ strongly absorb light in the UVA region.

Although increasing visible light intensity will increase operating cost, appreciable enhancement of DE can be obtained by N-ZrO$_2$, especially for MB degradation. However, it should be noted that at high light intensity, the formation of electron-hole pairs also competes with electron-hole pairs recombination (Ollis et al., 1991). Based on the criteria by Ollis et al. (Ollis et al., 1991), the visible light intensity applied in this study (16.5 and 144.7 W/m^2) corresponds to low irradiation. Therefore, if light intensity continuously increases, the enhancement of DE would still increase due to insignificant recombination of electron-hole pairs. Furthermore, at the same intensity of 3.5 W/m^2, UVA is more effective than UVC for the dye degradation by N-ZrO$_2$. Thus, UVA is preferable to be used for the degradation of AM, MB, and R6G using N-ZrO$_2$. Also, UVA is less harmful than UVC.

4.2.4. Effect of operating parameters on the dye degradation under visible light

4.2.4.1 Effect of dye concentration

As is evident, the dye concentration is directly proportional to DE. When the initial concentration increases from 5 to 25 mg/L, DE decreases from 59.4 to 32.8% for MB, from 31.5 to 18.3% for AM, and from 53.4 to 21% for R6G after 4 h (Table 4.13).

4.2.4.2 Effect of catalyst concentration

It is well-known that there is a limit of catalyst concentration, above which the DE will decrease (Akpan & Hameed, 2009). The same effect is also found in the present case. For the MB degradation, DE increases from 44.3 to 50.1% as the catalyst concentration increases from 0.5 to 1 g/L. With further increasing concentration to 2.5 g/L, DE decreases to 17.8%. A similar trend is observed in the case of AM and R6G degradation and the optimum catalyst concentration is found to be 1.5 g/L.

4.2.4.3 Effect of pH

For the MB degradation, DE increases from 45.5 to 51.2% when the pH increases from 5 to 8. With further increasing pH to 9, DE slightly decreases to 49.8%. The same trend of DE is observed for the degradation of AM. The optimum pH is also found to be 8. However, in the case of R6G degradation, DE keeps increasing with the increase of pH. As it is seen, AM is more easily degraded in slightly basic conditions above pH_{ZPC} of 7.05. This lower AM degradation in low pH below pH_{ZPC} may be due to the interaction of the three sulfonic groups in AM molecule with H^+ forming a neutral species of AM and hence making AM poorly adsorbed on the catalyst surface. In the present study, the same trend of DE is also observed for AM and MB although their ionic states in aqueous suspension are different.
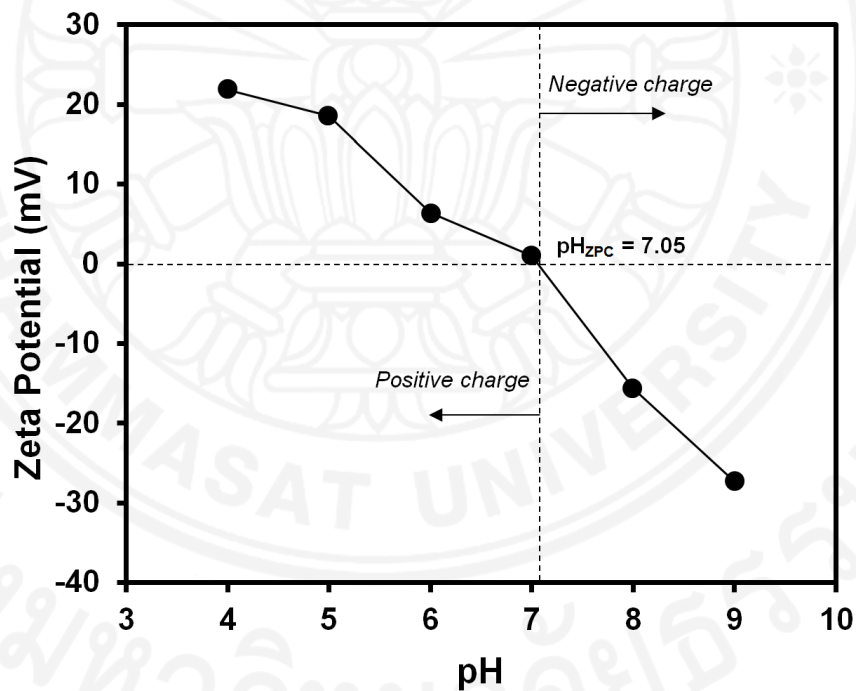
Figure 4.20 Zeta-potentials of N-ZrO$_2$ suspended in water as a function of pH.

Table 4.13 Dye degradation efficiency by N-ZrO$_2$ at different operating parameters under visible light.

Parameter	Value	DE (%)			Fixed parameter
		MB	AM	R6G	
Dye concentration (mg/L)	5	59.4	31.5	53.4	$W = 1$ g/L, pH = 7, $t = 4$ h, $I_{vis} = 16.5$ W/m^2
	10	50.1	26.4	40.3	
	15	41.3	23.7	32.4	
	20	35.6	20.2	25.2	
	25	32.8	18.3	21.0	
Catalyst concentration (g/L)	0.5	44.3	22.3	26.2	$C_0 = 10$ mg/L, pH = 7, $t = 4$ h, $I_{vis} = 16.5$ W/m^2
	1	50.1	26.4	40.3	
	1.5	47.6	28.1	41.5	
	2	32.3	19.5	37.8	
	2.5	17.8	07.3	30.2	
pH	5	45.5	23.2	34.5	$W = 1$ g/L, $C_0 = 10$ mg/L, $t = 4$ h, $I_{vis} = 16.5$ W/m^2
	6	49.4	25.1	37.8	
	7	50.1	26.4	40.3	
	8	51.2	28.5	42.6	
	9	49.8	27.3	44.1	
Salinity (g/L NaCl)	0	50.1	26.4	40.3	$W = 1$ g/L, $C_0 = 10$ mg/L, pH = 7, $t = 4$ h, $I_{vis} = 16.5$ W/m^2
	0.3	47.2	27.7	39.3	
	0.6	45.5	28.9	37.8	
	1.2	42.3	25.1	36.2	
	4.8	30.2	20.1	30.6	
	9.6	27.4	19.8	19.2	

4.2.4.4 Effect of salinity

The effect of salinity on the dye degradation efficiency is different for AM, R6G, and MB. As NaCl concentration increases from 0.3 to 9.6 g/L, DE continuously decreases from 47.2 to 27.4% for MB degradation and from 39.3 to 19.2% for R6G degradation. This fact may be because Cl⁻ can react with •OH radicals resulting in decreased concentration of these radicals. Also, with increasing salinity, there is a significant competition between Cl⁻ and dye molecules for the limited catalyst surface, leading to catalyst deactivation (Konstantinou & Albanis, 2004a). However, in the case of AM, with increasing NaCl concentration from 0.3 to 0.6 g/L, DE slightly increases from 27.7 to 28.9%. DE then decreases to 19.8% with an increase in NaCl concentration to 9.6 g/L. From these results, it is obvious that the effect of salinity on the dye degradation efficiency varies with respect to the molecular structure and the chemical state of the dye in suspension system.

4.2.5 Effect of operating parameters on the dye degradation under UVC light

The results of the dye degradation using $N-ZrO_2$ under UVC light are summarized in Table 4.14. The trend in the effect of operating parameters under UVC light are similar to those under visible light. Nevertheless, less time is required to attain the same value of DE. This is because the maximum absorption peak of $N-ZrO_2$ is still in the UV region and the charge carriers produced by UV light also have stronger reduction and oxidation power. The minor difference in the effect of operating parameters can also be due to the difference in the dye degradation mechanism. Under visible light, self-degradation of dye through photosensitization mechanism occurs, together with dye oxidation by reactive species (Wang et al., 2011a).

Table 4.14 Dye degradation efficiency by $N-ZrO_2$ at different operating parameters under UVC light.

Parameter	Value	DE (%)			Fixed parameter
		MB	AM	R6G	
Dye concentration	5	95.3	89.1	98.7	$W = 1$ g/L, pH = 7, $t = 2$ h (MB); 4 h
(mg/L)	10	85.2	84.5	92.3	(AM); 3.2 h (R6G), $I_{UVC} = 3.5$ W/m^2
	15	71.4	71.3	84.6	
	20	59.6	63.6	76.4	
	25	50.5	55.2	68.4	
Catalyst	0.5	74.5	82.3	70.2	$C_0 = 10$ mg/L, pH = 7, $t = 2$ h (MB); 4
concentration (g/L)	1	85.2	84.5	92.3	h (AM); 3.2 h (R6G), $I_{UVC} = 3.5$ W/m^2
	1.5	87.6	79.8	93.3	
	2	77.5	68.2	86.5	
	2.5	65.7	51.1	78.6	
pH	5	79.6	81.2	84.1	$W = 1$ g/L, $C_0 = 10$ mg/L, $t = 2$ h
	6	80.9	82.6	89.4	(MB); 4 h (AM); 3.2 h (R6G), $I_{UVC} =$
	7	85.2	84.5	92.3	3.5 W/m^2
	8	86.7	85.3	94.1	
	9	83.2	84.8	92.1	
Salinity (g/L NaCl)	0	85.2	84.5	92.3	$W = 1$ g/L, $C_0 = 10$ mg/L, pH = 7, $t = 2$
	0.3	84.5	85.1	90.5	h (MB); 4 h (AM); 3.2 h (R6G), $I_{UVC} =$
	0.6	82.4	83.9	88.7	3.5 W/m^2
	1.2	80.1	82.4	84.4	
	4.8	75.7	81.3	78.1	
	9.6	60.3	76.2	73.7	

4.2.6 Effect of H_2O_2 concentration on the R6G degradation

The effect of H_2O_2 concentration on the degradation of R6G that by N-ZrO_2 (Table 4.15) is found to be similar with that by N-ZnO. DE increases from 24.5 to 32.5% and from 72.1 to 83.1% with increasing H_2O_2 concentration from 0.1 to 0.7 g/L under visible and UVC light, respectively. As explained previously, the enhancement of DE after H_2O_2 addition is mainly due to the generation of additional •OH by the reaction of H_2O_2 with •O_2^- (Eq. 4.2) and the prevention of electron-hole recombination as a result of the consumption of the photoproduced electrons by H_2O_2 (Eq. 4.1).

Table 4.15 Dye degradation efficiency by N-ZrO_2 at different concentrations of H_2O_2.

H_2O_2 concentration (g/L)	DE (%)		Fixed parameter
	Visible	UVC	
0	21.0	68.4	$W = 1$ g/L, $C_0 = 25$ mg/L,
0.1	24.5	72.1	pH = 7, $t = 2$ h, $I_{vis} = 16.5$
0.3	27.2	76.5	W/m^2, $I_{UVC} = 3.5$ W/m^2
0.5	30.7	80.2	
0.7	32.5	83.1	

4.2.7 Role of reactive species on the degradation of R6G by N-ZrO_2

As can be seen in Table 4.16 and Figures 4.21-4.22, superoxide radical (•O_2^-) and singlet oxygen ($^1O_2$) are mainly responsible for the degradation of R6G under visible light. On the contrary, highly oxidative •OH radicals are predominant under UVC light. The hole also plays an important role in the R6G degradation through direct attack of R6G molecules on the catalyst surface. In all the cases, photoproduced electron plays a negligible role, which further indicates effective electron transfer from the N-ZrO_2 surface to the adsorbed molecules to produce reactive species. Since the R6G degradation under visible light are mainly due to the presence of less oxidative radicals instead of highly oxidative radicals, DE under visible light is lower than that under UVC light.

Table 4.16 The k_{app} of R6G degradation by $N-ZrO_2$ in the presence of quenchers.

Quencher	Quenched reactive species	k_{app} (h^{-1}); RS (%)	
		vis1/N-ZrO$_2$	UVC/N-ZrO$_2$
No quencher		0.133; -	0.803; -
KI	h$^+$	0.110; 17.4	0.238; 70.3
Isopropanol	•OH	0.093; 30.1	0.157; 80.4
Sodium azide	$^1O_2$	0.038; 70.9	0.545; 32.1
2-chloroethanol	e$^-$	0.129; 3.4	0.746; 7.1
p-benzoquinone	•O$_2^-$	0.066; 50.1	0.461; 42.5

W = 1 g/L, C_0 = 10 mg/L, pH = 7, I_{vis} = 16.5 W/m^2, I_{UVC} = 3.5 W/m^2.
The role of reactive species is in the following order:
vis1/N-ZrO$_2$: $^1O_2$ > •O$_2^-$ > •OH > h$^+$ > e$^-$.
UVC/N-ZrO$_2$: •OH > h$^+$ > •O$_2^-$ > $^1O_2$ > e$^-$.
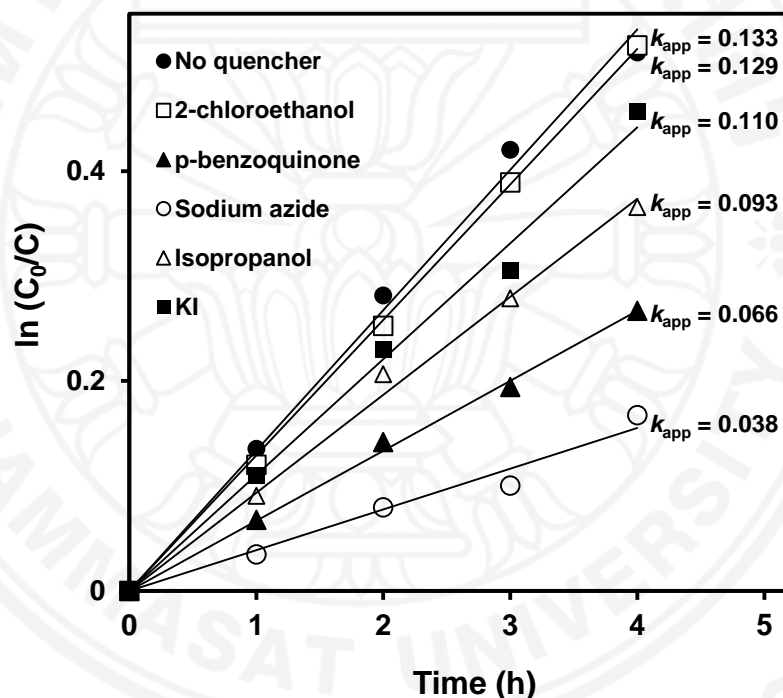
Figure 4.21 The kinetics plots for pseudo first order reaction of R6G degradation by N-ZrO$_2$ under visible light in the presence of quencher (I_{vis} = 16.5 W/m^2, C_0 = 10 mg/L, W = 1 g/L, pH = 7).
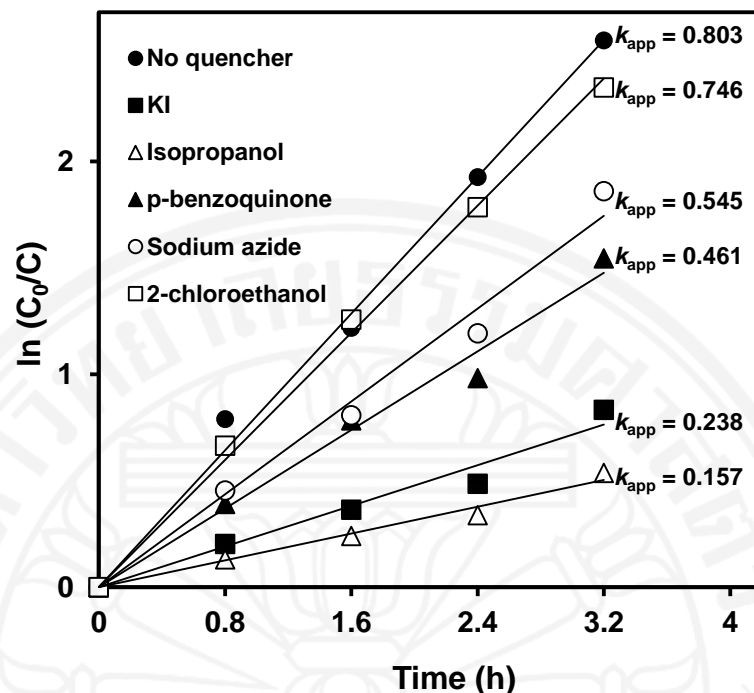
Figure 4.22 The kinetics plots for pseudo first order reaction of R6G degradation by
N-ZrO$_2$ under UVC light in the presence of quencher (I_{UVC} = 3.5 W/m^2,
C_0 = 10 mg/L, W = 1 g/L, pH = 7).

4.2.8 Catalyst reusability

As presented in Table 4.17, N-ZrO$_2$ is highly reusable, indicating its exceptional
photochemical stability. Insignificant decreases of DE over time may be due to the
deposition of the dye degradation products. Based on the TN measurement, N-
containing compounds are also not observed in the solution above the detection limit
of the instrument.

Table 4.17 Reusability of N-ZrO$_2$ for the dye degradation.

Light source	Dye	Irradiation time (h)	DE (%)					
			1st run	2nd run	3rd run	4th run	5th run	6th run
Visible	MB	4	51.8	52.4	53.1	52.6	52.2	51.4
	AM	4	30.4	31.2	30.8	31.3	31.2	29.5
	R6G	4	40.3	38.2	39.7	37.5	36.4	36.6
UVC	MB	2	88.4	88.3	88.6	87.8	87.2	86.0
	AM	4	89.4	89.0	88.3	87.4	86.2	85.1
	R6G	3.2	92.3	93.5	90.3	89.3	89.8	87.1

W = 1 g/L, C_0 = 10 mg/L, pH = 7, I_{vis} = 16.5 W/m^2, I_{UVC} = 3.5 W/m^2.

4.2.9 Toxicity evaluation

Toxicity evaluation of the photocatalytically treated AM and MB solutions against *Bacillus cereus* with the REMA plate method shows no inhibition for the dye solutions treated with N-ZnO for 4 h (AM) and 1.5 h (MB) under visible light (Table 4.18).

Table 4.18 Comparative bacterial inhibition by the dye solutions photocatalytically treated with N-ZrO$_2$.

	Inhibition (%)	
	AM	MB
Initial	8.13	3.52
Final	No inhibition	No inhibition

The initial dye concentration is 10 mg/L, and the final MB and AM concentrations are 1.48 and 1.55 mg/L, respectively.

4.3 Dye degradation by N-WO$_3$

4.3.1 Photocatalytic activity of N-WO$_3$ synthesized with different amounts of urea

Table 4.19 shows DE of the N-WO$_3$ catalysts synthesized with different amounts of urea. DE increases with increasing the amount of urea up to an optimum value. Thus, the enhancement of photocatalytic activity is evidently attributed to the addition of urea which may lead to N doping. Although it is not that significant, addition of more urea is found to be detrimental to DE, as in the case of N-WO$_3$ with U/Z of 2. The N-WO$_3$ with U/Z of 2 shows a lower photocatalytic activity compared to that with U/Z of 1. This is most likely due to crystallinity reduction. Reduced crystallinity may lead to low mobility of charge carriers to migrate from the bulk to the surface of the catalyst and thus results in higher probability of charge carrier recombination.

Table 4.19 DE of the N-WO$_3$ catalysts synthesized with different amounts of urea for the AM degradation.

Light source	DE (%)				
	U/Z = 0	U/Z = 0.25	U/Z = 0.5	U/Z = 1	U/Z = 2
Visible	8.5	10.6	27.8	86.8	86.1
UVA	4.5	12.1	70.8	91.2	89.5

$C_0 = 25$ mg/L, $W = 1$ g/L, pH = 7, $t = 1$ h, $I_{vis} = 144.7$ W/m^2, $I_{UVA} = 3.5$ W/m^2.

4.3.2 Properties of N-WO$_3$

4.3.2.1 Vibrational spectroscopy

The infrared spectra of the catalysts are shown in Figure 4.23. The peaks at around 3440 cm^{-1} are assigned to the O-H stretching (asymmetric and symmetric) modes of adsorbed water and the peak around 1630 cm^{-1} is assigned to the O-H bending of the adsorbed water (Nogueira et al., 2004). Moreover, the strong, broad peak in the fingerprint region of 500-900 cm^{-1} is assigned to the W-O stretching modes (Nogueira et al., 2004). As can be seen, the W-O stretching modes are less intense for N-WO$_3$ and the peak is also slightly shifted to a lower wavenumber.
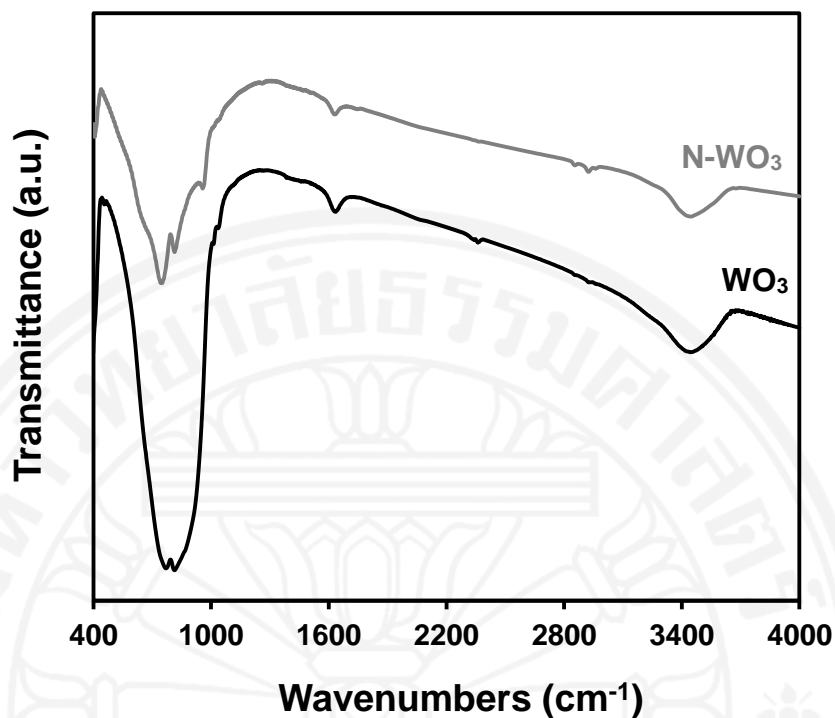
Figure 4.23 FTIR spectra of WO_3 and N-WO_3.

4.3.2.2 Thermal properties

The thermogram of WO_3 and N-WO_3 are shown in Figure 4.24. The weight loss below 500 °C is attributed to the removal of adsorbed water. Insignificant weight loss from 500 to 700 °C in the thermogram of N-WO_3 is ascribed to the decomposition of oxygen-containing groups (Aimable et al., 2010) and can be an indication of higher availability of surface functional groups such as hydroxyl groups in N-WO_3. The final weight loss of WO_3 and N-WO_3 are about 3 and 10%, respectively.
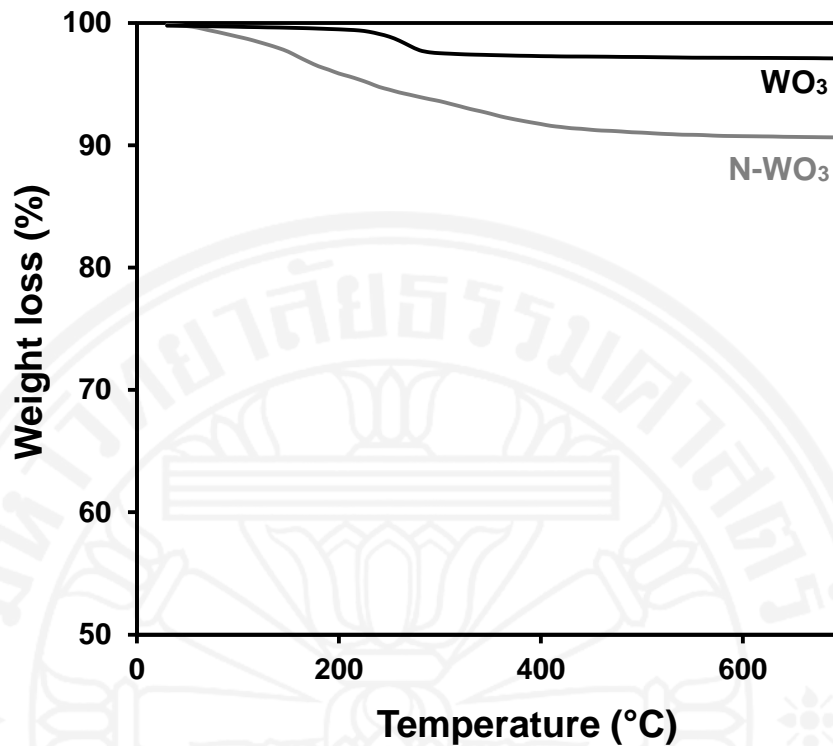
Figure 4.24 Thermogram of WO₃ and N-WO₃.

4.3.2.3 Morphological properties

The diameter of N-WO₃ particles is around 40 nm with no significant aggregation (Figure 4.25(a,b)). The structure of N-WO₃ particles is of zero-dimensional. Figure 4.25(c) shows the HR-TEM image of N-WO₃. The lattice fringes with 0.38 nm can be seen and are assigned to *d* spacing of monoclinic WO₃ [020] plane.
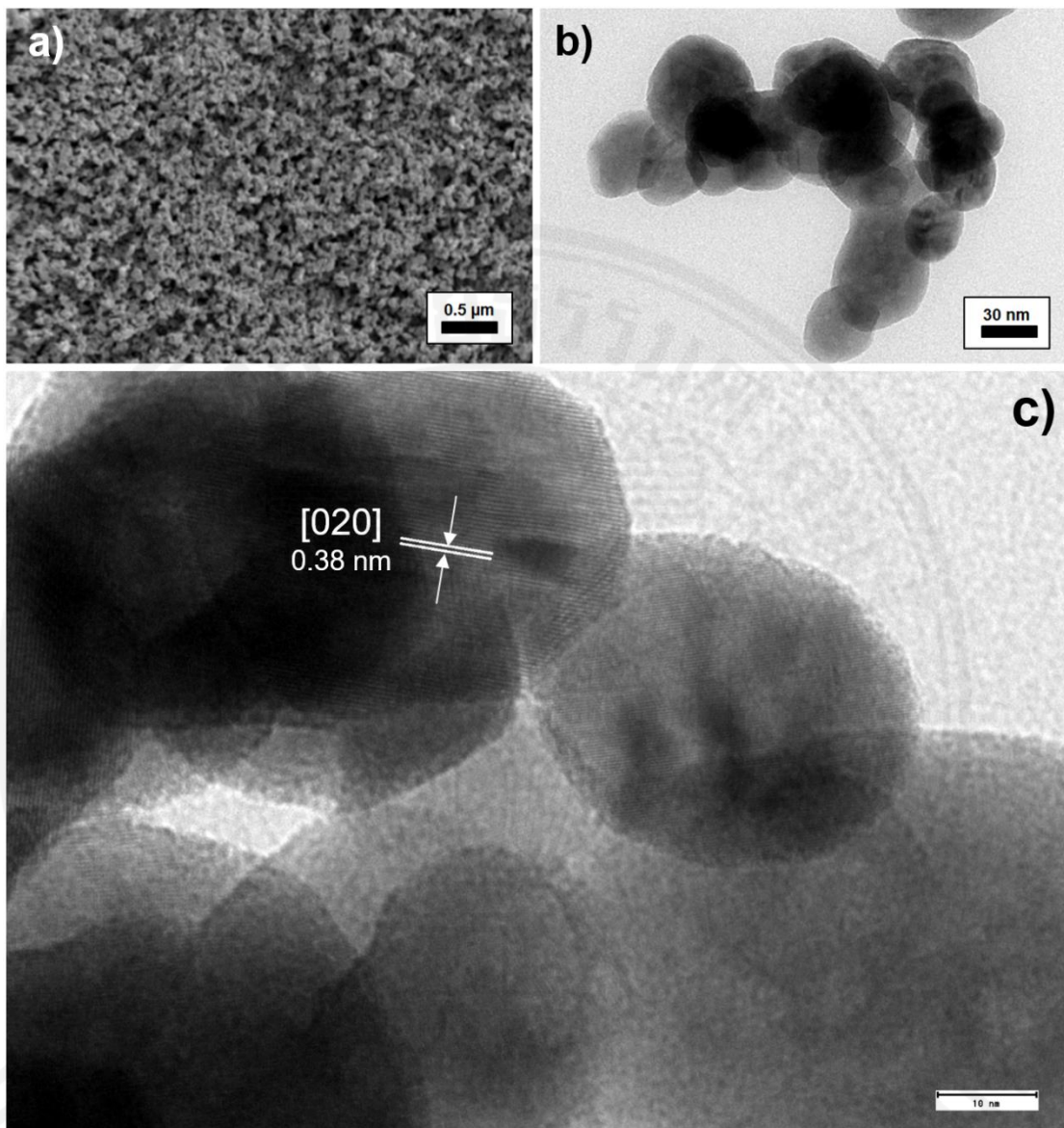
Figure 4.25 SEM (a), TEM (b), and HR-TEM (c) images of N-WO$_3$.

4.3.2.4 Crystallinity and structural properties

Figure 4.26(a) shows the XRD patterns of the WO$_3$ and N-WO$_3$. The diffraction patterns can be assigned to monoclinic WO$_3$ (JCPDS No.43-1035). The formation of W$_2$N, which induces deactivation of the photoresponse (Liu et al., 2012), is not observed. Furthermore, as can be seen from the diffraction pattern, the peak intensity is lowered after adding urea. This can be due to crystal growth inhibition by the urea which reduces the crystallinity. No significant peak shift in the diffraction pattern, and hence no lattice distortion, is observed. The N dopants seem to have been effectively incorporated into the lattice structure of the N-WO$_3$. The primary crystalline sizes of

the WO_3 and $N\text{-}WO_3$, determined by Scherrer equation, are 37.4 and 17.1 nm, respectively. The decrease of crystalline size is beneficial for facilitating rapid migration of electron-hole pairs to the catalyst surface to generate various reactive species.
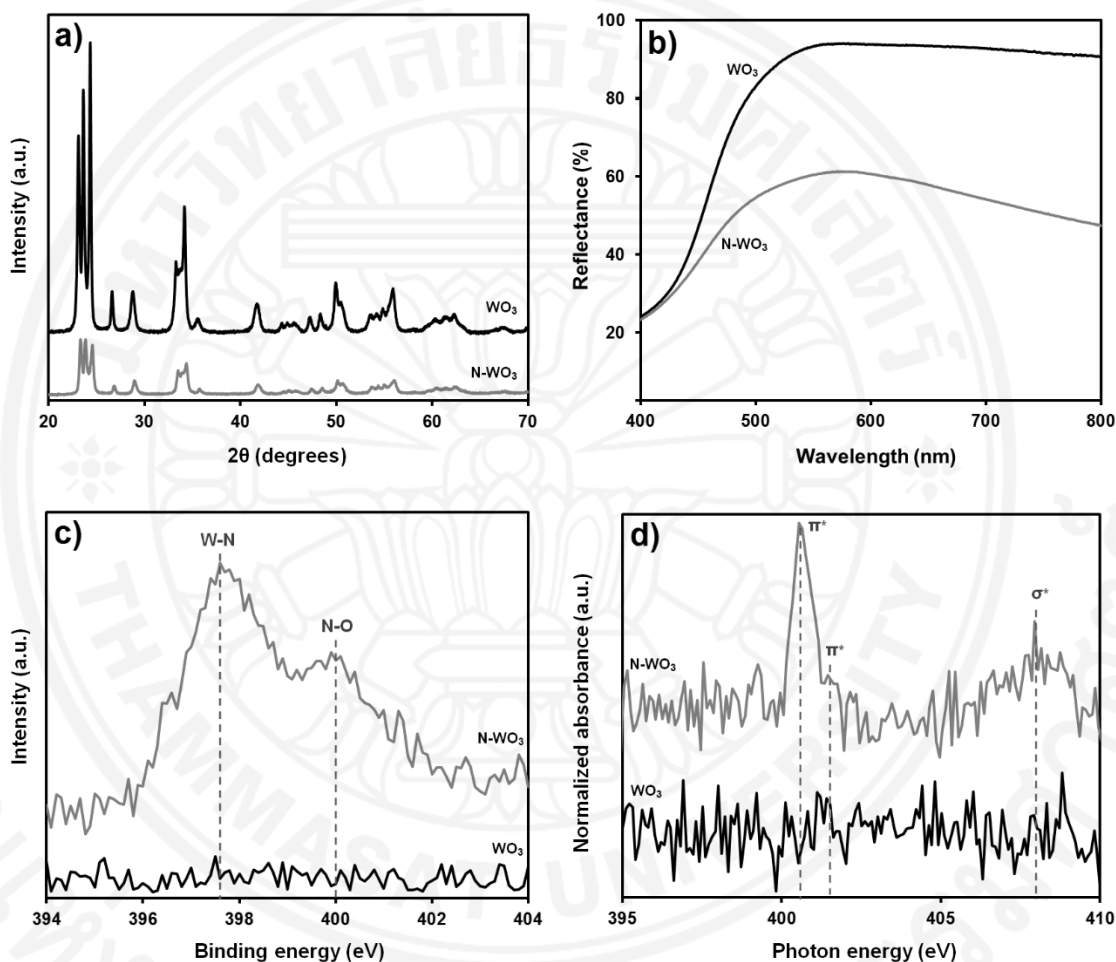
Figure 4.26 The XRD patterns (a), DRS spectra (b), N 1s XPS spectra (c), and N K-edge XANES spectra (d) of WO_3 and $N\text{-}WO_3$.

4.3.2.5 Optical properties

Figure 4.26(b) shows the DRS spectra of the catalysts. Doping with N shifts the absorption edge toward the longer wavelength region with a tail extending up to the NIR region, leading to two-phase absorption in UV and visible/NIR region. This is attributed to the formation of a mid-band state by N 2p orbitals within the band gap and the formation of the oxygen defect band states. Oxygen defects may be enhanced during grinding operation.

4.3.2.6 Chemical state of nitrogen

The high resolution XPS spectra of N 1s region of the catalysts are shown in Figure 4.26(c). Two well-defined peaks are observed in N-WO$_3$. The peak at 397.6 eV is assigned to the W-N bond, while the one centered at 400 eV corresponds to the bonding state of N-O (Zhang et al., 1999). Therefore, it is suggested that O is substituted by N and W-O-N bond is formed. Figure 4.26d shows the N K-edge XANES spectra of the catalysts. Besides the 1s → σ* peak at around 408 eV, a sharp peak at 400.6 eV for 1s → π* of W-N and a peak with lower intensity at 402 eV for 1s → π* of N-O are also observed in N-WO$_3$. Summing up, the incorporation of N into the WO$_3$ lattice is confirmed by the XANES and XPS spectra.

4.3.2.7 Textural properties

The SSA of N-WO$_3$ (14 m^2/g) is slightly higher than that of WO$_3$ (10 m^2/g) (Figure 4.27). The increased SSA after N doping can be due to the decreased crystalline size or the formation of more pores as a result of gas liberation during the decomposition of urea in the calcination process. The increased SSA is beneficial for enhancing the photocatalytic activity as photocatalytic degradation of dye is a surface phenomenon and occurs on the catalyst surface.
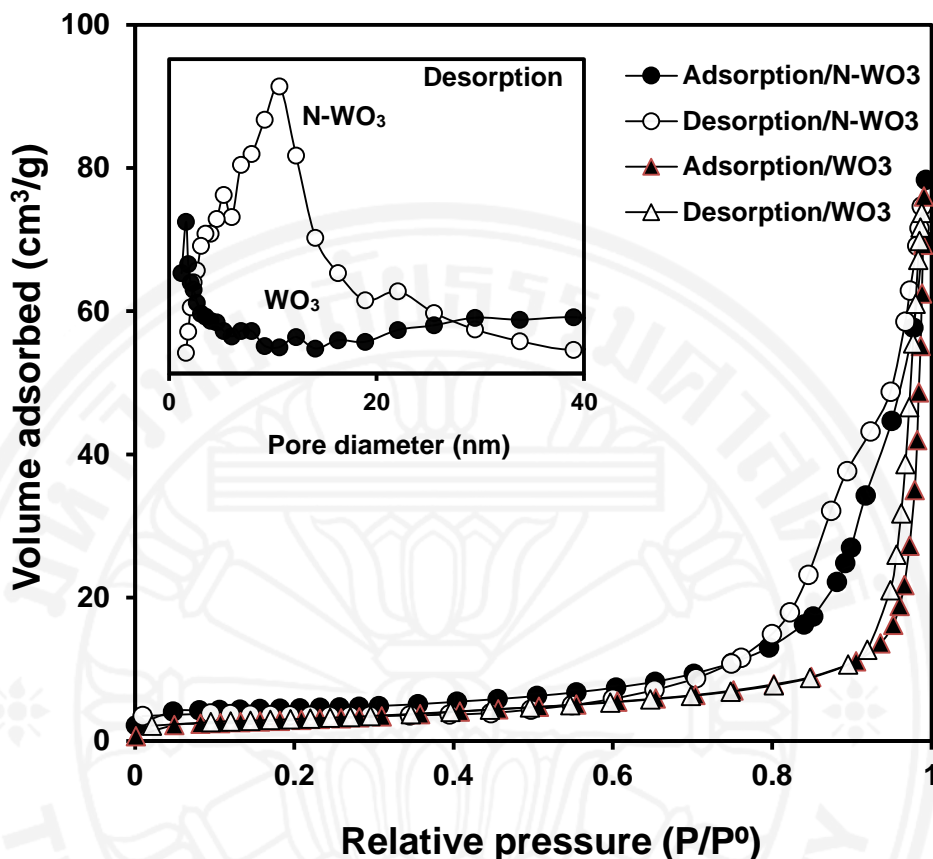
Figure 4.27 N$_2$ adsorption-desorption isotherms. The insert is pore size distribution curves of WO$_3$ and N-WO$_3$.

4.3.3 Comparative AM degradation under visible and UVA light

The comparative degradation of AM by WO$_3$, N-WO$_3$, c/WO$_3$, and c/N-WO$_3$ are summarized in Table 4.20. The photocatalytic activity of WO$_3$ is found to be higher than that of c/WO$_3$. This may be attributed to the difference in the light absorption ability, the availability of surface functional groups, and the specific surface area. The doped catalysts show better photocatalytic activity than the pristine counterpart. Moreover, c/N-WO$_3$ exhibits lower photocatalytic activity than N-WO$_3$. DE under visible light is comparable to that under UVA light because under visible light, AM can also be self-degraded after transferring its electron to the CB of the catalyst (Banerjee et al., 2014). In addition, the irradiance of visible light used is much higher than that of UVA light.

Table 4.20 Efficiency for AM degradation by WO_3-based catalysts.

Catalyst	Adsorption (%)	DE (%)	
		Visible	UVA
WO_3	2.7	17.1	21.0
c/WO_3	2.1	9.3	10.2
N-WO_3	5.5	100	100
c/N-WO_3	3.5	28.3	23.5

$W = 1$ g/L, $C_0 = 5$ mg/L, pH = 7, $t = 1$ h, $I_{vis} = 144.7$ W/m^2, $I_{UVA} = 3.5$ W/m^2.

4.3.4 Effect of operating parameters on the AM degradation

4.3.4.1 Effect of dye concentration

As can be seen in Table 4.21, with increasing initial AM concentration from 5 to 25 mg/L, DE decreases from 100 to 86.2% and from 100 to 89.5% for AM degradation under visible and UVA light, respectively. With an increase in initial AM concentration, AM molecules in the bulk of the suspension become strongly absorb incoming light. This leads to reduced light absorption by the catalyst and the generation of electron-hole pairs is then reduced.

4.3.4.2 Effect of catalyst concentration

For the photocatalytic degradation of 10 mg/L of AM under visible light, with an increase in catalyst concentration from 0.5 to 1 g/L, DE increases from 93.5 to 100%. With further increasing catalyst concentration to 2.5 g/L, DE then decreases to 81.5%. The same trend is also observed for the photocatalytic degradation of AM under UVA light and the optimum catalyst concentration is found to be 1 g/L. This can be due to that with an increase in catalyst concentration, the total active surface area increases. However, the suspension turbidity also increases. As a result, the light scattering increases, leading to decreased light penetration.

4.3.4.3 Effect of pH

Suspension pH is considered to be a critical operating parameter on the photocatalytic degradation of organic compounds (Sun et al., 2008) and therefore its effects on the dye degradation should be studied. As seen in Table 4.23, for the photocatalytic degradation of 10 mg/L of AM under visible light, DE is observed to be the same (100%) with increasing pH from 5 to 7. Further increases of pH from 7 to 9 decreases

85

DE from 100 to 87.3%. Similarly for the degradation of AM under UVA light, with an increase of pH from 5 to 7, DE is the same value of 100% and then decreases to 90.1% with further increasing pH to 9. This can be explained as follows. The pH_{ZPC} of the catalyst is 2.1 (Figure 4.28). Therefore, the N-WO_3 surface is negatively charged above pH of 2.1. AM, as an anionic dye, is poorly adsorbed on the surface of N-WO_3 due to electrostatic repulsion. With increasing pH, this electrostatic repulsion is more significant and the adsorption of AM becomes less favorable. As a result, DE is greatly decreased.
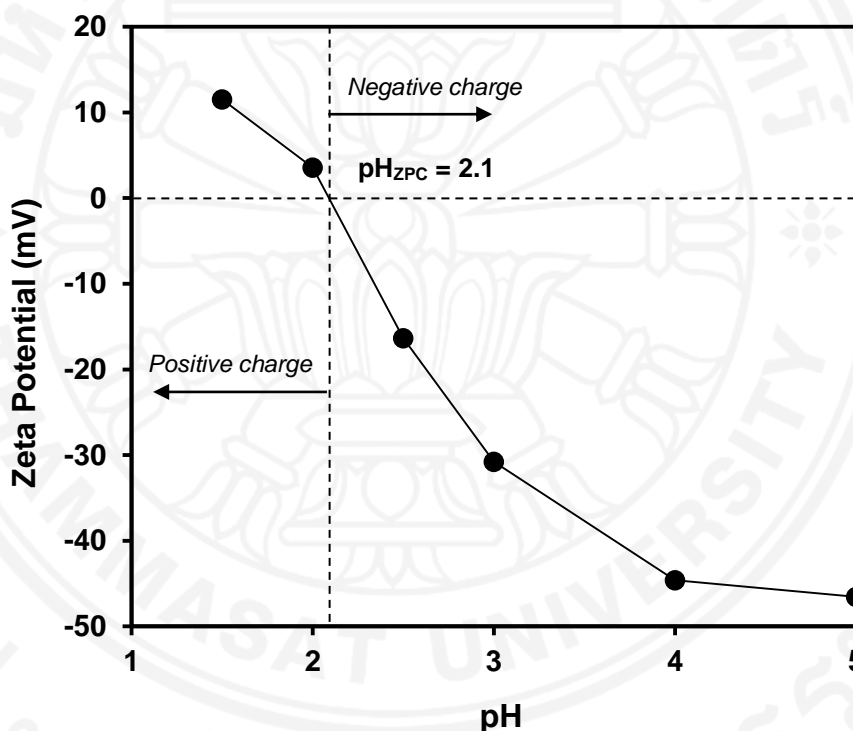
Figure 4.28 Zeta-potentials of N-WO_3 suspended in water as a function of pH.

4.3.4.4 Effect of H_2O_2 concentration

As previously mentioned, H_2O_2 is known to beneficially affect the organic compound degradation due to the generation of $\cdot OH$ radicals and due to its role as an irreversible electron acceptor (Sun et al., 2008). However, it was also reported that an excess of H_2O_2 leads to competitive reactions that can inhibit the photocatalytic degradation process (Daneshvar et al., 2003). The holes generated by the catalyst may also be consumed by H_2O_2. A similar effect is observed in the degradation of AM by N-WO_3

under visible light. With increasing H_2O_2 concentration, DE increases up to an optimum value (0.5 g/L) and subsequently decreases. On the contrary, under UVA light, with increasing H_2O_2 concentration to 0.7 g/L, DE keeps increasing. This may be because H_2O_2 undergoes photolysis producing two additional •OH radicals which can degrade the dye (Stefan et al., 1996). The effect of H_2O_2 on the AM degradation is found to depend on the type of light source used.

Table 4.21 Dye degradation efficiency by N-WO$_3$ at different operating parameters.

Parameter	Value	DE (%)		Fixed parameter
		Vis	UVA	
Dye concentration (mg/L)	5	100	100	$W = 1$ g/L, pH = 7, $t = 1$ h, $I_{vis} = 144.7$ W/m^2, $I_{UVA} = 3.5$ W/m^2
	10	100	100	
	15	94.5	96.6	
	20	90.2	92.1	
	25	86.2	89.5	
Catalyst concentration (g/L)	0.5	93.5	95.1	$C_0 = 10$ mg/L, pH = 7, $t = 1$ h, $I_{vis} = 144.7$ W/m^2, $I_{UVA} = 3.5$ W/m^2
	1	100	100	
	1.5	95.0	96.7	
	2	90.9	88.3	
	2.5	81.5	82.0	
pH	5	100	100	$W = 1$ g/L, $C_0 = 10$ mg/L, $t = 1$ h, $I_{vis} = 144.7$ W/m^2, $I_{UVA} = 3.5$ W/m^2
	6	100	100	
	7	100	100	
	8	93.2	95.4	
	9	87.3	90.1	
H_2O_2 concentration (g/L)	0	86.2	89.5	$W = 1$ g/L, $C_0 = 25$ mg/L, pH = 7, $t = 1$ h, $I_{vis} = 144.7$ W/m^2, $I_{UVA} = 3.5$ W/m^2
	0.1	90.1	92.6	
	0.3	98.4	97.3	
	0.5	100	98.1	
	0.7	96.2	100	

4.3.4.5 Effect of inorganic ions

On the basis of k_{app} values, the inhibition of AM degradation by inorganic anions under visible light is in the following order: $CO_3^{2-} > Cl^- > SO_4^{2-} > NO_3^-$ (Table 4.22). CO_3^{2-} inhibits the degradation of AM quite significantly. The first reason may be due to the weakening of AM adsorption on the catalyst surface. After adding CO_3^{2-}, the catalyst surface becomes more negatively charged due to increased suspension pH. As a result, AM as an anionic species is repelled by the negatively charged surface of N-WO$_3$. The second reason is probably due to the scavenging character of CO_3^{2-} on •OH radical (Guillard et al., 2003b):

$$CO_3^{2-} + \bullet OH \rightarrow OH^- + \bullet CO_3^- \tag{4.5}$$

One can see that the inhibitory effect of Cl^- is lower than that of CO_3^{2-}. The inhibition by Cl^- can be due to displacement of surface bound OH^- ions (Wang et al., 2013a), which then reduces the generation of $\bullet OH$ radicals. The scavenging of the holes and $\bullet OH$ radicals (Eqs. (4.6) and (4.7)) by Cl^- may also inhibit the AM degradation (Chong et al., 2010):

$$Cl^- + h^+ \rightarrow \bullet Cl \tag{4.6}$$
$$Cl^- + \bullet OH \rightarrow \bullet Cl + OH^- \tag{4.7}$$

Furthermore, the inhibitory effect of SO_4^{2-} is found to be lower than that of Cl^-. Although SO_4^{2-} may also scavenge the holes and $\bullet OH$ radicals (Eqs. (4.8) and (4.9)), it is greatly repelled by negatively charged $N-WO_3$ surface via electrostatic repulsion. Thus, there is no significant inhibition on the adsorption of AM observed.

$$SO_4^{2-} + h^+ \rightarrow \bullet SO_4^- \tag{4.8}$$
$$SO_4^{2-} + \bullet OH \rightarrow \bullet SO_4^- + OH^- \tag{4.9}$$

In the case of NO_3^-, it may compete for surface active sites that are involved in displacement over the surface bound OH^- ions. However, it can be photolyzed forming $\bullet OH$ radical (Eqs. (4.10), (4.11), and (4.12)) (Zhang et al., 2005). Therefore, the net result is a negligible inhibitory effect.

$$NO_3^- + hv \rightarrow [NO_3^-]^* \tag{4.10}$$
$$[NO_3^-]^* \rightarrow \bullet NO_2 + \bullet O^- \tag{4.11}$$
$$\bullet O^- + H_2O \rightarrow \bullet OH + OH^- \tag{4.12}$$

Under UVA light, the inhibition order of the dye degradation by the anions investigated is $CO_3^{2-} > Cl^- > NO_3^- > SO_4^{2-}$. The inhibition order under UVA light is found to be slightly different than that under visible light. This is due to the difference in the AM degradation mechanism. As seen, the inhibitory effect of NO_3^- is found to be higher than that of SO_4^{2-}. This may be due to the UV screening effect by NO_3^-

(Burns et al., 1999). One can also see that the reduction of k_{app} is more pronounced in the case of AM degradation under UVA light.

Under both visible and UVA light, the inhibitory effect of NH_4^+ is lower than that of Ca^{2+}. NH_4^+ shows negligible effects since it is at its maximum oxidation state and thus is incapable of inhibiting the photocatalytic degradation process. Although Ca^{2+} is also at its maximum oxidation state, it may be reduced by the photogenerated electron and deposited on the catalyst surface. The deposition of Ca^0 hinders the adsorption of AM. Additionally, the compression of the electrical double layer at a high Ca^{2+} concentration of 0.1 M may induce catalyst aggregation and precipitation (Thio et al., 2011).

Table 4.22 The k_{app} of AM degradation by N-WO$_3$ in the presence of inorganic ions.

Inorganic ions	k_{app} Visible (min^{-1})	k_{app} UVA (min^{-1})
No ion	0.0339	0.0381
Cl$^-$	0.0290	0.0246
NO$_3^-$	0.0319	0.0283
CO$_3^{2-}$	0.0251	0.0233
SO$_4^{2-}$	0.0311	0.0346
NH$_4^+$	0.0335	0.0372
Ca^{2+}	0.0252	0.0218

W = 1 g/L, C_0 = 25 mg/L, pH = 7, ion concentration = 0.1 M, I_{vis} = 144.7 W/m^2, I_{UVA} = 3.5 W/m^2.

4.3.5 Role of reactive species

Table 4.23 shows k_{app} values, with or without the presence of the quenchers. With the addition of quenchers, k_{app} is found to decrease. Under both visible and UVA light, significant role of h^+ is observed. This is because upon irradiation, h^+ is generated not only in the VB, but also in the mid-gap state formed by the N dopant. The h^+ participates in the photocatalytic degradation process by directly attacking AM on the catalyst surface. Small reductions of k_{app} with the addition of isopropanol suggest that $\bullet OH$ contributes to the degradation of AM in a lesser extent. Negligible inhibition of k_{app} with the addition of NaN_3, p-benzoquinone, and 2-chloroethanol suggests that $^1O_2$, $\bullet O_2^-$, and e^- have a very minor role in the AM degradation. The minor role of $^1O_2$ and $\bullet O_2^-$ is due to the lower CB edge of N-WO$_3$. As a result, one-electron reduction process which generates $\bullet O_2^-$ from the reaction between O_2 and e^- cannot occur. Due to unavailability of $\bullet O_2^-$, h^+ cannot react with $\bullet O_2^-$ to produce $^1O_2$.

It is important to note that the role of h^+ under visible light is less significant than that under UVA light. This indicates that dye sensitization mechanism is the major pathway for the degradation of AM under visible light instead of dye oxidation by reactive radicals. The existence of dye sensitization as the major pathway is supported by the fact that this sensitization process is thermodynamically highly favorable. During sensitization process, the excited electrons from the LUMO of AM can be easily transferred to the CB of N-WO$_3$ due to considerably low CB potential of N-WO$_3$. In contrast, oxidation of AM by reactive radicals is the main pathway for AM degradation under UVA light as dye sensitization cannot occur under UV light.

Table 4.23 The k_{app} of AM degradation by N-WO$_3$ in the presence of quenchers.

Quencher	Quenched reactive species	Vis/N-WO$_3$		UVA/N-WO$_3$	
		k_{app} (min^{-1})	RS (%)	k_{app} (min^{-1})	RS (%)
No quencher	-	0.0339	-	0.0381	-
KI	h^+	0.0256	24.4	0.0094	75.3
Isopropanol	$\bullet OH$	0.0285	15.8	0.0269	29.5
NaN$_3$	$^1O_2$	0.0328	3.3	0.0376	1.3
2-chloroethanol	e^-	0.0326	3.5	0.0369	3.1
p-benzoquinone	$\bullet O_2^-$	0.0332	2.1	0.0367	3.7

W = 1 g/L, C_0 = 25 mg/L, pH = 7, I_{vis} = 144.7 W/m^2, I_{UVA} = 3.5 W/m^2.
The role of reactive species is in the following order:
Vis/N-WO$_3$: $h^+ > \bullet OH > e^- > {}^1O_2 > \bullet O_2^-$.
UVA/N-WO$_3$: $h^+ > \bullet OH > \bullet O_2^- > e^- > {}^1O_2$.

Figure 4.29 The kinetics plots for pseudo first order reaction of AM degradation by N-WO$_3$ under visible light in the presence of quenchers (I_{vis} = 144.7 W/m^2, W = 1 g/L, C_0 = 25 mg/L, pH = 7).
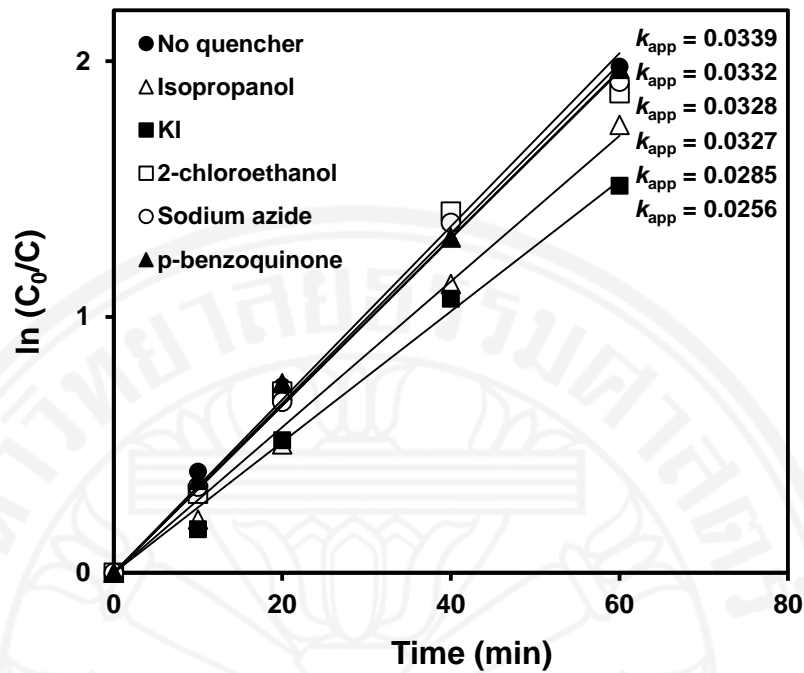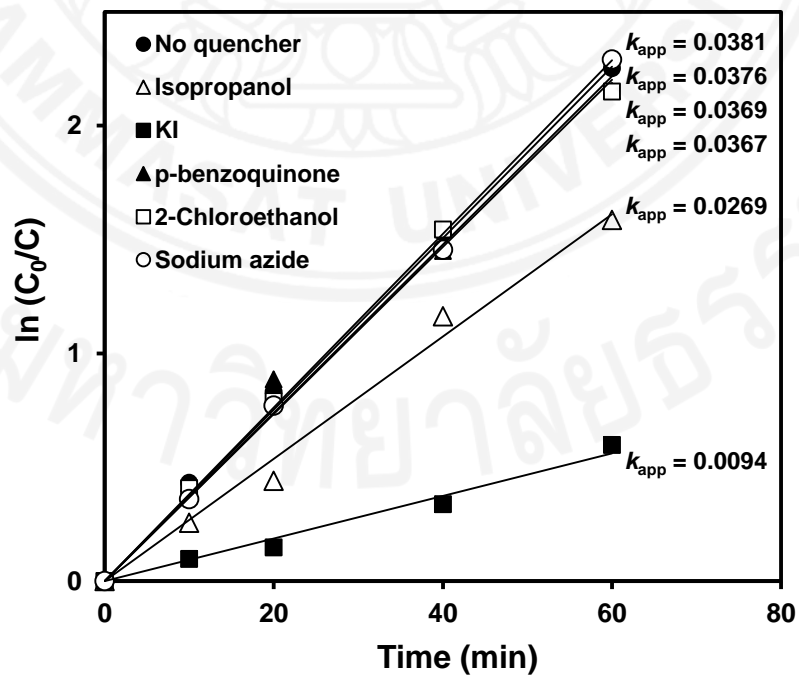

Figure 4.30 The kinetics plots for pseudo first order reaction of AM degradation by N-WO$_3$ under UVA light in the presence of quenchers (I_{UVA} = 3.5 W/m^2, W = 1 g/L, C_0 = 25 mg/L, pH = 7).

91

4.3.6 Visible light activity of N-WO$_3$

The prepared N-WO$_3$ shows superior photocatalytic activity for the degradation of AM under visible light. This can be due to the direct oxidation of AM by the holes generated either in the N$_{2p}$ or in the VB. The self-degradation of AM through a photosensitization mechanism can also indirectly contribute to the observed photocatalytic activity. The photosensitization mechanism involves electron transfer from the AM to the N-WO$_3$, instead of electron transfer from the CB to O$_2$ that produces $\cdot$O$_2^-$ (one-electron reduction mechanism). During light absorption by the adsorbed AM, the electron in AM is excited from the HOMO to the LUMO. This excited electron can be transferred to the CB of N-WO$_3$. This process is thermodynamically very favorable due to considerably low CB edge of N-WO$_3$. After losing its electron, the adsorbed AM becomes a radical cation which undergoes further reactions forming inorganic compounds. Hypothetically, the absence of one-electron reduction is due to the lower CB edge of WO$_3$ which cannot provide a sufficient potential to reduce O$_2$ (Arai et al., 2009). The inability of O$_2$ to scavenge CB electrons results in fast recombination. However, in the N-WO$_3$, fast recombination can be greatly supressed due to electron trapping process involving single-electron-trapped oxygen vacancy and interstitial N (Wang et al., 2011a):

$$\cdot V_o + e^- \rightarrow \cdot\cdot V_o \tag{4.13}$$

$$\cdot\cdot V_o + N \rightarrow \cdot V_o + \cdot N^- \tag{4.14}$$

$$\cdot N^- + O_2 \rightarrow N + \cdot O_2^- \tag{4.15}$$

where, $\cdot V_o$ represents single-electron-trapped oxygen vacancy and $\cdot\cdot V_o$ equates to dual-electrons-trapped oxygen vacancy. Upon irradiation, photogenerated electrons are excited from VB to CB of N-WO$_3$. They can be trapped by single-electron-trapped oxygen vacancy and thus do not recombine with the holes. Interstitial N then entraps the electron from dual-electrons-trapped oxygen vacancy. This interstitial N with an excess electron is unstable and immediately detraps the electron to O$_2$.
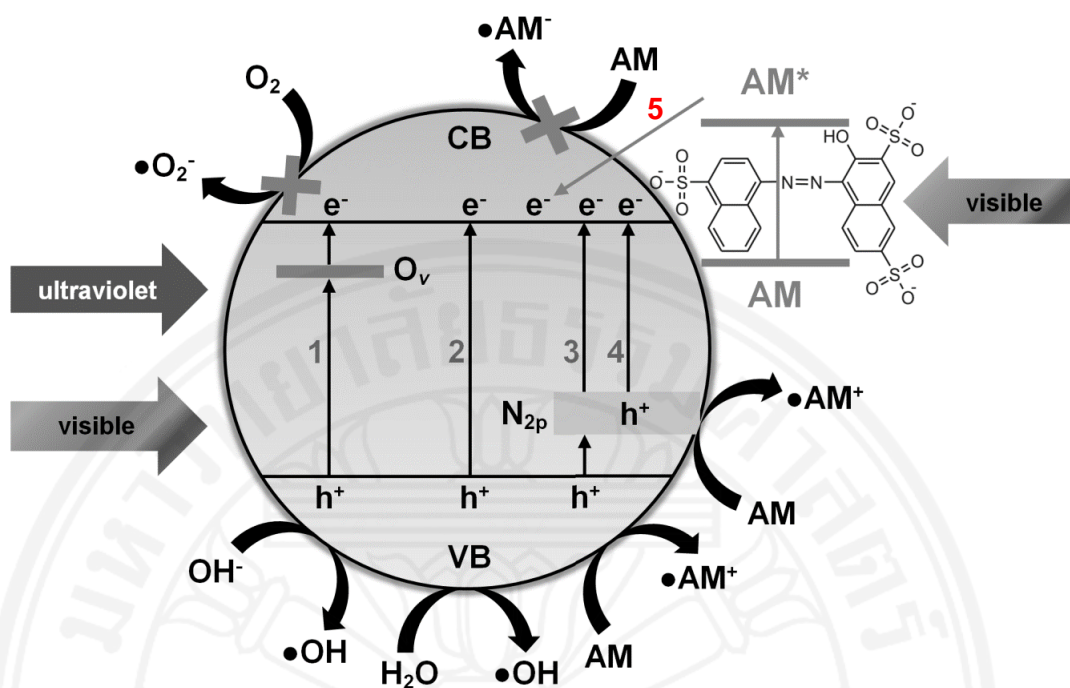
Figure 4.31 The proposed mechanism of AM degradation by N-WO$_3$. The excitation
of electron in N-WO$_3$ upon visible light or UV light takes place through
different pathways: (1) electron is excited from VB to CB via O_v; (2)
electron is directly excited from VB to CB; (3) electron is excited from
VB to CB via N$_{2p}$; (4) electron is excited from N$_{2p}$ to CB. Upon visible
light irradiation, the electron in AM is excited and can be injected to CB
of N-WO$_3$ (5). AM can also be directly oxidized by the hole generated in
either VB or N$_{2p}$. Note that one-electron reduction mechanism, in which
O$_2$ is reduced to •O$_2^-$ by the photogenerated electron, cannot occur due to
very low (positive) CB potential of N-WO$_3$.

4.3.7 Catalyst reusability

The results presented in Figure 4.32 show slight decreases of photocatalytic activity
after repeated cycles under both visible and UVA light. After six runs, degradation
efficiencies under visible and UVA light only decrease from 96.5% to 91.6% and
98.1% to 92.3%, respectively. This indicates high photostability of the N dopants and
the absence of surface modifications.
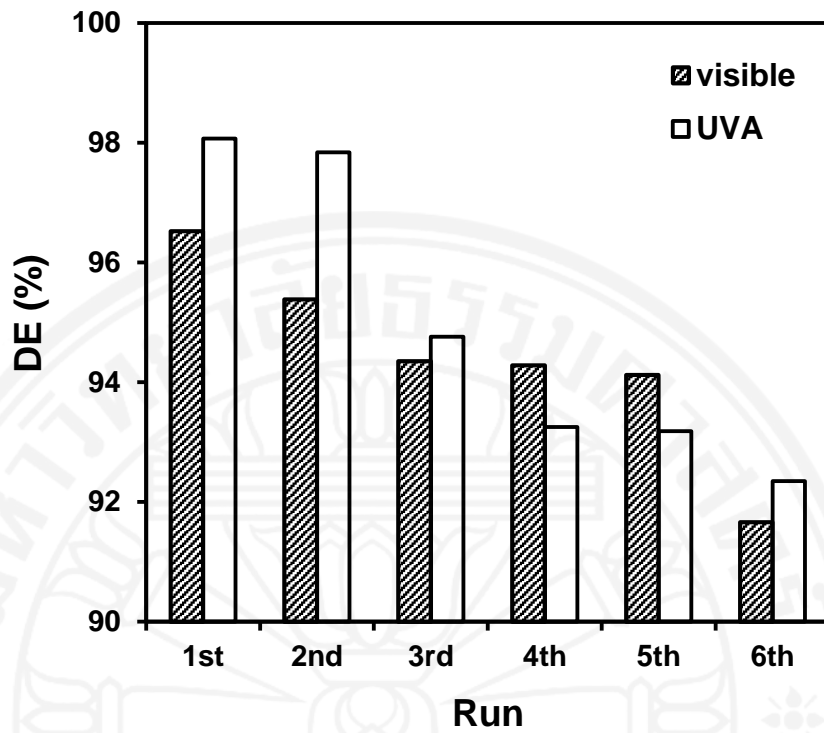
Figure 4.32 Reusability of N-WO$_3$ for the AM degradation (W = 1 g/L, C_0 = 25 mg/L, pH = 7, t = 100 min, I_{vis} = 144.7 W/m^2, I_{UVA} = 3.5 W/m^2).

94

Chapter 5

Dye degradation in continuous flow system

This chapter provides the experimental results of the dye degradation in continuous flow system and their discussion, including the properties of the photoactive systems. The results and discussion are divided into two parts, according to the photoactive system used, namely dye degradation by N-WO$_3$@PF and N-ZnO@PF.

5.1 Dye degradation by N-WO$_3$@PF

5.1.1 Properties of N-WO$_3$@PF

5.1.1.1 Crystallinity and structural properties

Figure 5.1 shows the XRD patterns of the samples. Four major characteristic peaks of polyester are observed at 16.67°, 17.53°, 22.6°, and 25.42°. After coating with N-WO$_3$, some characteristic peaks of WO$_3$ are observed, for instance, those at 23.23° (002), 23.7° (020), and 24.44° (200). The observed diffraction patterns can be assigned to monoclinic WO$_3$ (JCPDS No.43-1035). Moreover, small reductions in the intensity of polyester peaks are seen after catalyst coating. These small reductions are due to the decreased crystallinity of the constituent polymer as the fabric is pretreated with NaOH and UVC. After 12 runs, the polyester peaks slightly decrease because of the decreased crystallinity upon irradiation. Upon irradiation, the reactive radicals produced by N-WO$_3$ can attack the polyester structure leading to decreased crystallinity.
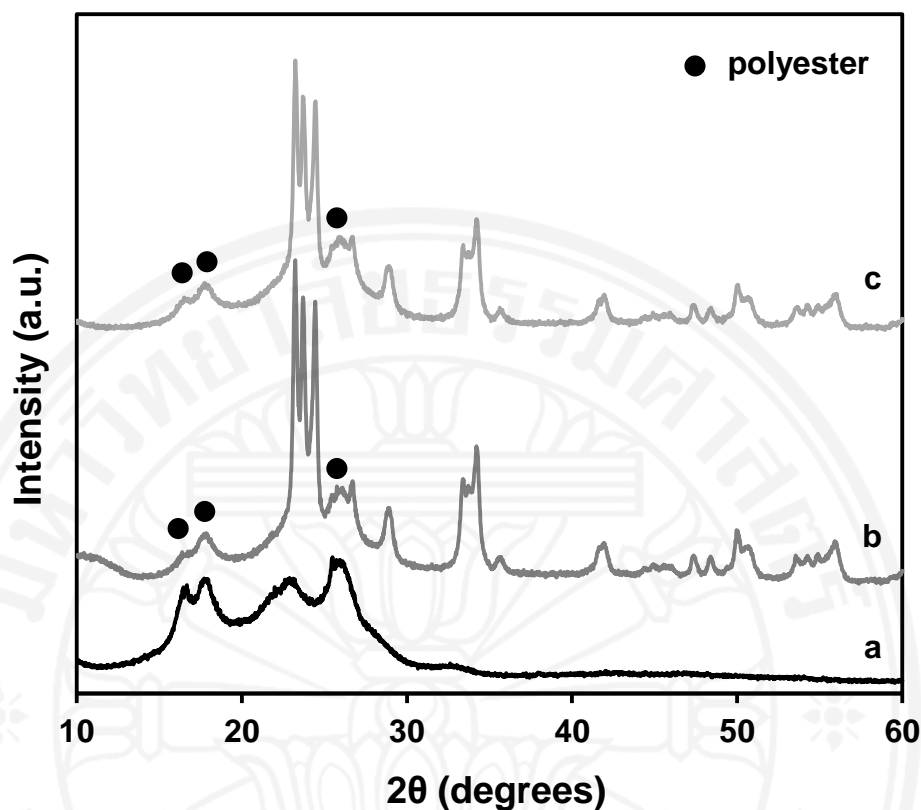
Figure 5.1 XRD patterns of PF (a), N-WO$_3$@PF (b), and used N-WO$_3$@PF (c).

5.1.1.2 Vibrational spectroscopy

As can be seen from the ATR-FTIR spectra (Figure 5.2), characteristic peaks are dominated by those of polyester fabrics. Peaks of saturated esters due to carbonyl stretching are observed at 1712 cm^{-1}. The peaks centered at 1092, 1240, and 1338 cm^{-1} are assigned to ester group vibrations. All these peaks confirm the existence of ester linkage on the PF. Moreover, the overtones peaks observed at around 1407-1504 cm^{-1} are assigned to C–H bonds of the benzene rings, while the out of plane C–H peaks of benzene rings are observed at 720, 870, and 1016 cm^{-1}. After catalyst coating, a new peak due to W=O vibration is observed at 948 cm^{-1}. After 12 runs, this peak is shifted to 951 cm^{-1}. In fact, the position of W=O vibration peaks of N-WO$_3$@PF are different from that of WO$_3$ nanoparticles (962 cm^{-1}) (Pfeifer et al., 1995). This may be due to the interaction between the N-WO$_3$ particles and the functional groups on the PF surface. The characteristic peaks of polyester also overlap main peaks of WO$_3$, such as W-O stretching at 1048 cm^{-1} and out of plane deformation W-O-W at 700 cm^{-1}

(Pfeifer et al., 1995). It is important to note that the characteristic peaks of the N-WO$_3$@PF and the used N-WO$_3$@PF are almost the same. This implies that the chemical structure of the fabric surface is basically unchanged and is quite stable upon irradiation.
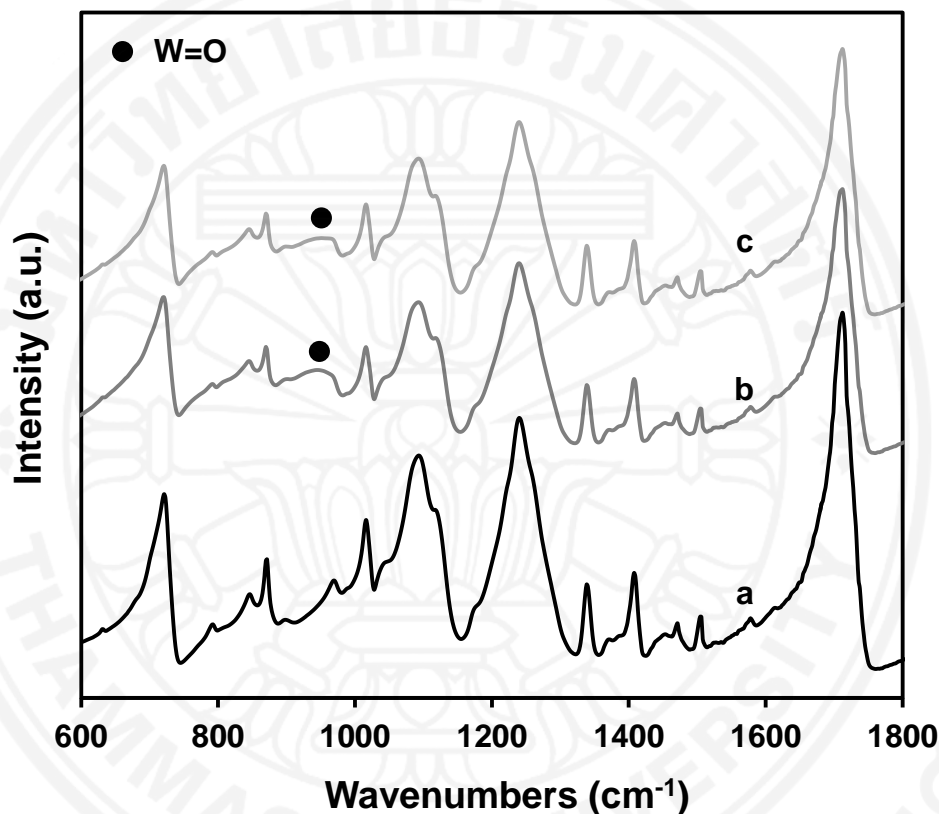
Figure 5.2 ATR-FTIR spectra of PF (a), N-WO$_3$@PF (b), and used N-WO$_3$@PF (c).

5.1.1.3 Morphological properties

The morphological properties of the samples are shown in Figure 5.3. Smooth, clean surface of PF is observed. After coating with N-WO$_3$, the PF surface becomes fully covered by the catalyst particles. The film of catalyst particles is also formed on the surfaces of PF fibers, not in between the fibers. Although aggregation of fine particles on some parts of PF surface is observed, overall, a continuous, relatively homogeneous coating of N-WO$_3$ on PF surface is achieved using the proposed heat attachment method. After 12 runs, some cracks and fiber shrinkages are found. Unattached particles are also visible. This is most likely due to decreased stability of

the catalyst particles on the PF surface, as a result of reactive radical attack on the surface structure of polyester upon irradiation.
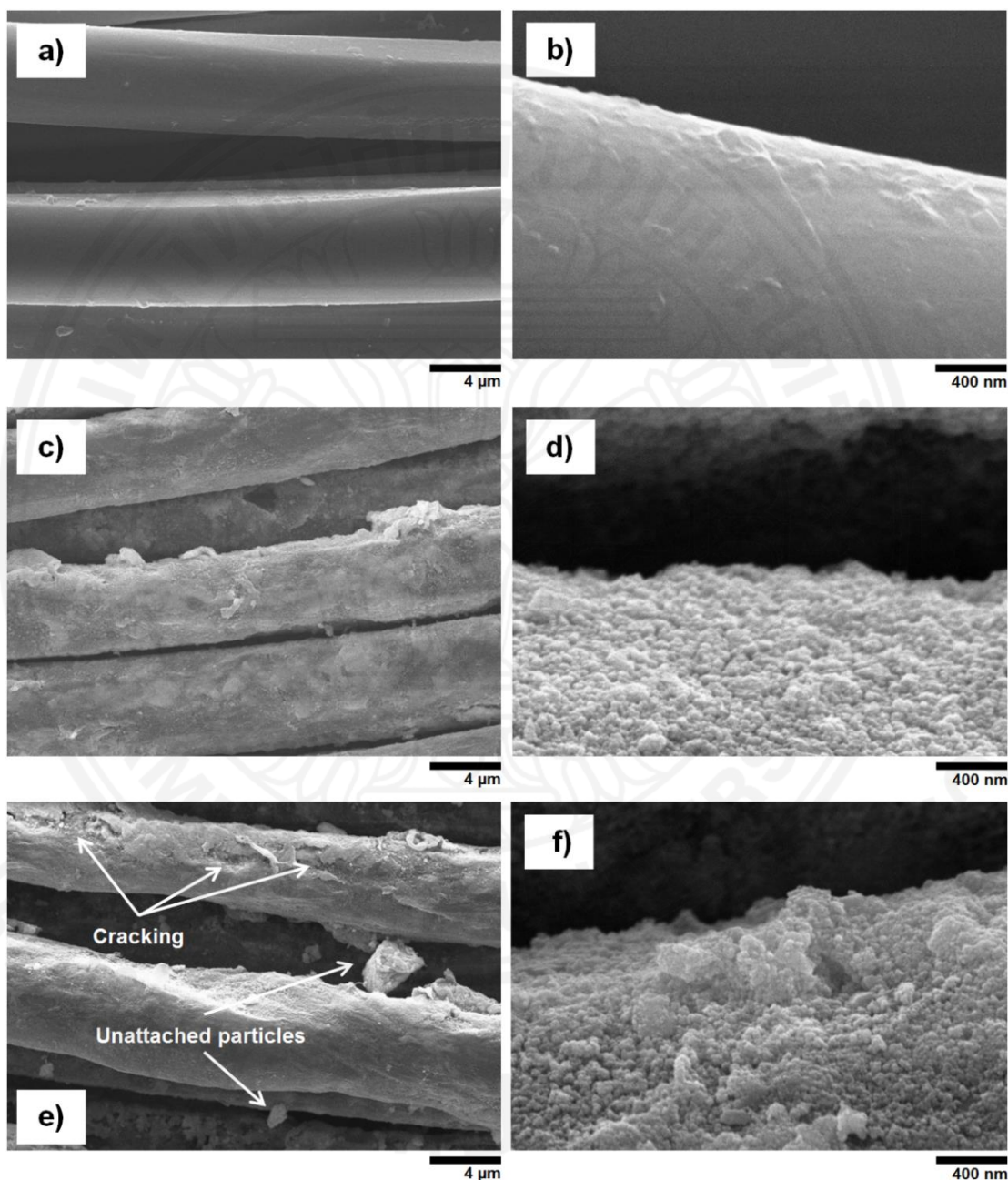
Figure 5.3 SEM images of PF (a, b), N-WO$_3$@PF (c, d), and used N-WO$_3$@PF (e, f).

5.1.1.4 Optical properties

The ability of the photoactive system to absorb light is evaluated by DRS. The spectrum of PF shows no absorption in the visible region (Figure 5.4). In contrast, the N-WO$_3$@PF exhibits remarkable absorption in the visible region even up to the NIR

region. After being used, it shows reduced absorbance in the visible-NIR region. Since N dopant is mainly responsible for the visible-NIR absorbance, it is postulated that the chemical properties of N on the catalyst surface change upon irradiation which then affects the electronic structure, and thus the absorption ability, of the N-WO_3@PF.
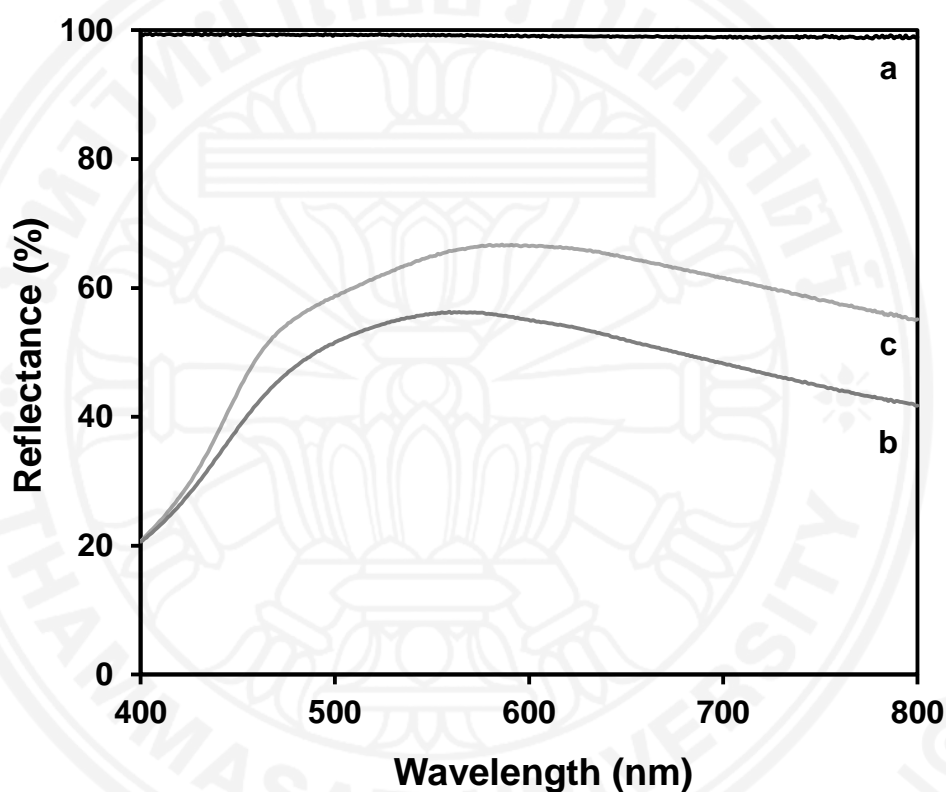
Figure 5.4 DRS spectra of PF (a), N-WO_3@PF (b), and used N-WO_3@PF (c).

5.1.2 Effect of operating parameters on the photocatalytic degradation of AM under solar light

5.1.2.1 Effect of dye concentration

The results of the photocatalytic degradation of AM at different initial concentrations of AM, ranging from 5 to 25 mg/L, are shown in Figure 5.5. The degradation of 5 mg/L AM is completed within 3 h. The time required to achieve complete degradation increases with increasing initial AM concentration.
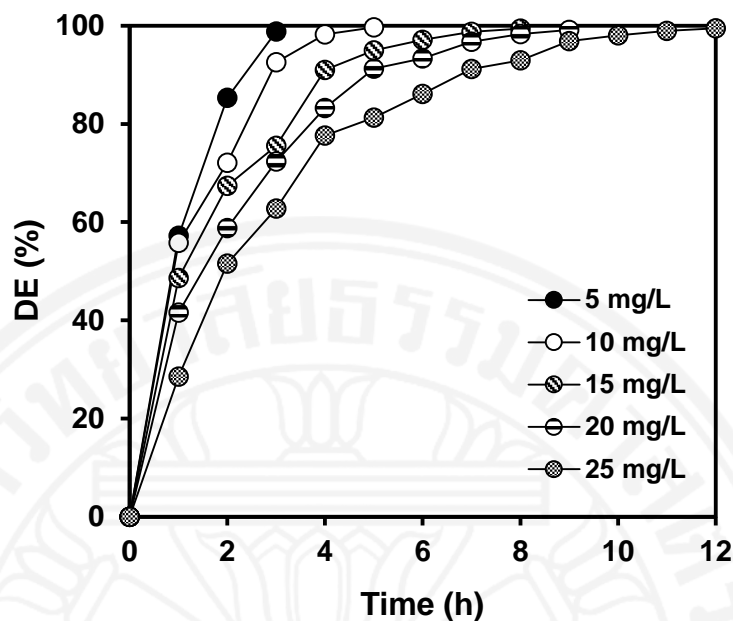
Figure 5.5 Photocatalytic degradation of AM by N-WO$_3$@PF at different initial AM concentration under solar light (pH = 7, v = 80 mL/min, θ = 20°).

5.1.2.2 Effect of pH

Figure 5.6 presents the photocatalytic degradation of AM at different pH values. The effect of pH on the photocatalytic process is relatively minor. DE is found to be higher in neutral conditions than in acidic or basic conditions. Up to 97.8% of AM can be degraded at pH of 7 within 4 h. This behavior may be related to the stability of the N-WO$_3$ on the PF surface. Although PF is quite resistant to weak acids and weak alkalis (Natarajan & Jeyakodi Moses, 2012), it may undergo hydrolysis which can degrade the polymer structure to a certain extent, as indicated by the crystallinity reduction. As a result, the stability of the loaded catalyst decreases. This then leads to reduced DE.

100
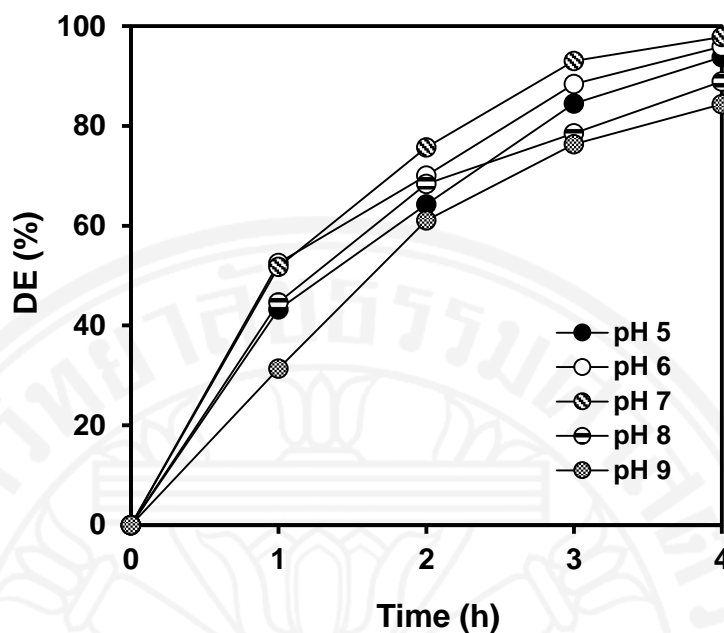
Figure 5.6 Photocatalytic degradation of AM by N-WO$_3$@PF at different pH under
solar light (C_0 = 10 mg/L, v = 80 mL/min, θ = 20º).

5.1.2.3 Effect of recirculation rate

The photocatalytic degradation of AM at different recirculation rates is shown in Figure 5.7. As recirculation rate increases from 80 to 120 mL/min, DE decreases from 97.2 to 78.4% with irradiation of 4 h. It is seen that photocatalytic degradation of AM is unfavorable at high recirculation rates. This is most likely due to that with increasing recirculation rate, the average liquid residence time decreases. Therefore, there is no sufficient contact between the dye molecules and the photoactive system. The shorter the liquid residence time on the sloping plate at a higher recirculation rate leads to a reduced probability of photocatalytic degradation. By assuming that the thick of the liquid film is 0.1 cm, the volume of the sloping plate is calculated to be 40 mL. Thus, the liquid residence times with recirculation rates of 80, 100, and 120 mL/min are found to be 0.5, 0.4, and 0.34 min, respectively.

101
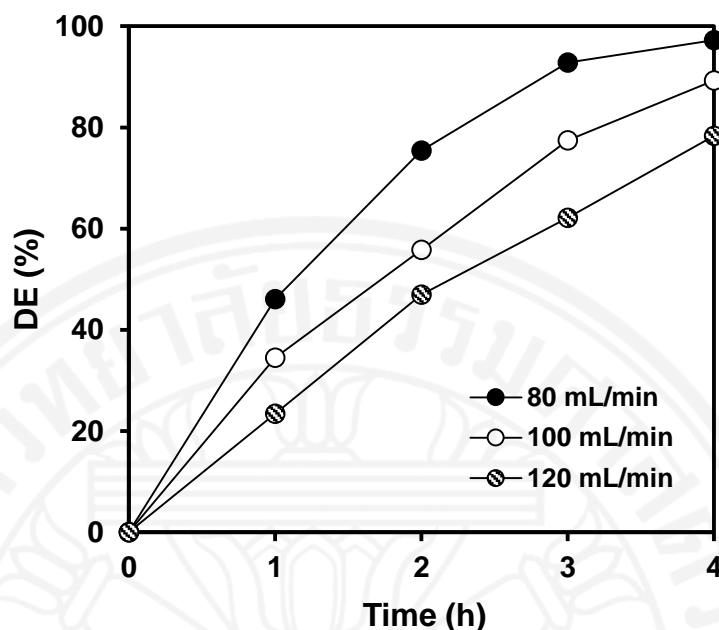
Figure 5.7 Photocatalytic degradation of AM by N-WO$_3$@PF at different recirculation
rate (C_0 = 10 mg/L, pH = 7, θ = 20º).

5.1.2.4 Effect of reactor inclination

AM degradation at different inclination angles of sloping plate from the horizontal
line is shown in Figure 5.8. With increasing inclination angles from 20° to 40°, DE
decreases from 97.4 to 82.8 % at irradiation of 4 h. This may be due to the fact that
increasing inclination angle reduces the liquid residence time. In addition, during a
particular period of experiment time, the amount of solar radiation received by the
photoactive system slightly decreases with increasing inclination angle. The average
solar irradiances, which were measured directly at the same angle as that of the
sloping plate, are found to be 586 (θ = 20º), 580 (θ = 30º), and 569 W/m^2 (θ = 40º). It
is to be noted that the amount of solar radiation does not always decrease with
increasing inclination angle since it depends on the elevation angle of the sun which
varies throughout the day and is dependent on the day of the year.
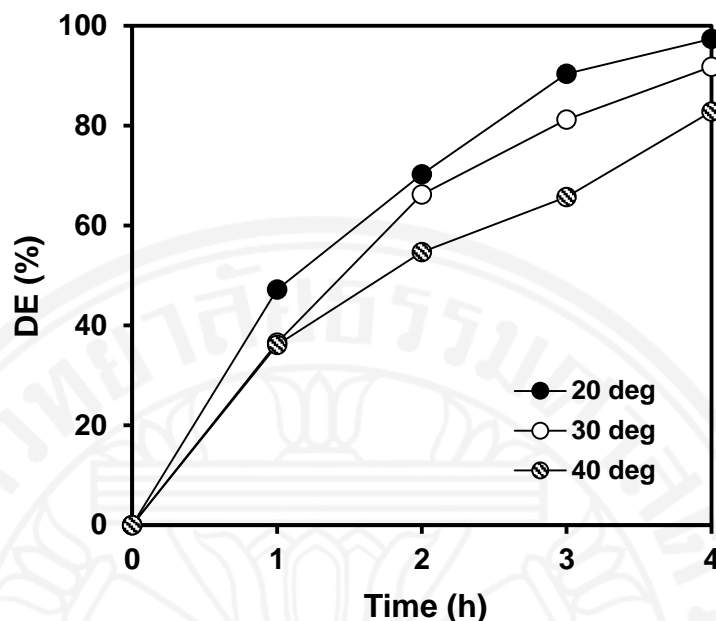
Figure 5.8 Photocatalytic degradation of AM by N-WO$_3$@PF at different reactor inclination (C_0 = 10 mg/L, pH = 7, v = 80 mL/min).

5.1.2.5 Effect of salinity

Figure 5.9 shows the effect of salinity on the photocatalytic degradation of AM. A noticeable effect on DE is found with the variation in salinity of the solution. With increasing salinity from 0.6 to 4.8 g/L of NaCl, DE decreases from 95.8 to 85.6 % with irradiation of 4 h. The inhibition of the photocatalytic degradation process in the presence of NaCl can be due to two factors. First is the scavenging of the holes and •OH radicals by Cl$^-$ (Chong et al., 2010). Second is the inhibition of the AM degradation as Na$^+$ may be adsorbed on the photoactive system surface. Strong adsorption of Na$^+$ prevents the AM molecules from accessing the active sites and reduces the absorption of the incoming light by the photoactive system.

103
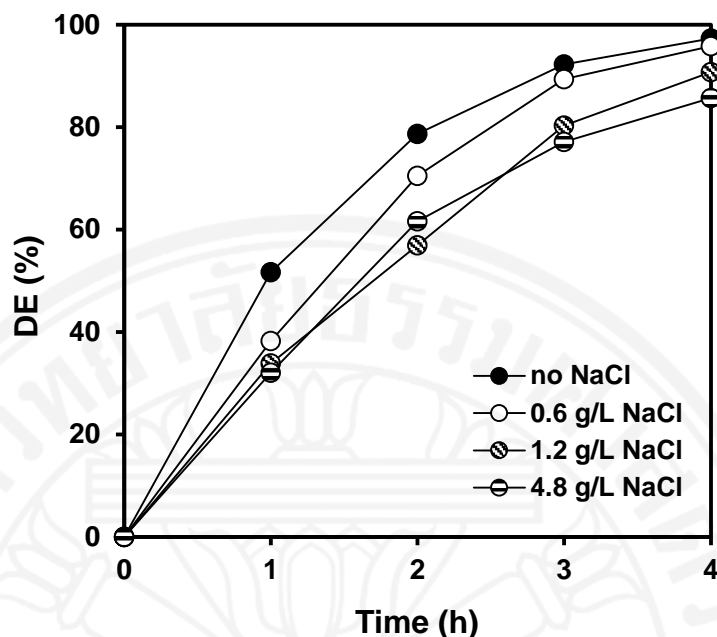
Figure 5.9 Photocatalytic degradation of AM by N-WO$_3$@PF at different salinity (C_0 = 10 mg/L, pH = 7, v = 80 mL/min, θ = 20º).

5.1.2.6 Effect of inorganic ions

As shown in Figure 5.10 and based on k_{app} values obtained, the inhibition by inorganic ions is in the following order: Ca^{2+} (k_{app} 0.582 h^{-1}) > CO$_3^{2-}$ (k_{app} 0.712 h^{-1}) > SO$_4^{2-}$ (k_{app} 0.820 h^{-1}) > NO$_3^-$ (k_{app} 0.875 h^{-1}). k_{app} in the absence of inorganic ions is 1.033 h^{-1}. It is found that Ca^{2+} considerably inhibits the degradation of AM. As previously explained, this is possibly because Ca^{2+} is greatly adsorbed by the photoactive system surface. The deposition of Ca^0 hinders the adsorption of AM and the absorption of incoming light. CO$_3^{2-}$ can also inhibit AM degradation quite significantly. This is probably because CO$_3^{2-}$ can scavenge the photogenerated •OH radicals (Eq. (4.5)) (Guillard et al., 2003b).

Furthermore, the inhibitory effect of SO$_4^{2-}$ is found to be insignificant. Although SO$_4^{2-}$ may scavenge the holes and •OH radicals (Eqs. (4.8) and (4.9)), it is repelled by N-WO$_3$ surface via electrostatic repulsion. In the case of photocatalytic degradation of AM in the presence of NO$_3^-$, NO$_3^-$ may displace the surface bound OH$^-$ ions, which can reduce the generation of •OH radicals. However, NO$_3^-$ can also be photolyzed, forming additional •OH radicals (Eqs. (4.10), (4.11), and (4.12)) (Zhang et al., 2005). Thus, the inhibitory effect of NO$_3^-$ is negligible.

It is to be noted that sodium salts are used as the sources of inorganic anions. Therefore, Na^+ may also inhibit the AM degradation because of its adsorption on the photoactive system surface which further interferes the adsorption of AM and the absorption of the incoming light, similar to the effect of salinity.
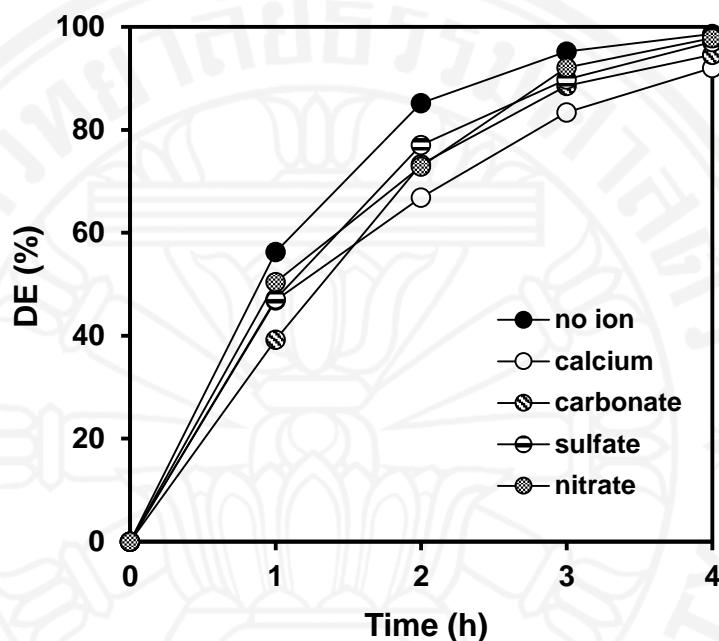
Figure 5.10 Photocatalytic degradation of AM by N-WO$_3$@PF in the presence of inorganic ions (C_0 = 10 mg/L, pH = 7, v = 80 mL/min, θ = 20°, ion concentration = 0.05 M).

5.1.3 Photocatalytic degradation of AM with different light sources

Light sources with different wavelength emitting regimes are used to evaluate the photocatalytic activity of N-WO$_3$@PF. The results are shown in Figure 5.11(a). Since there is a significant difference among the intensity of the light sources applied, the photocatalytic activity should not be compared directly. For solar photocatalytic degradation with initial AM concentration of 10 mg/L, almost 100% degradation of AM occurs within 5 h. Under UVA and visible light, it requires around 12 and 15 h for complete degradation, respectively. It is interesting to note that DE under UVA light is higher than that under visible light, although the intensity of UVA light is lower that of visible light. This is because the light absorption ability of the photoactive system is higher in UVA region than in visible region, as confirmed by

the DR spectra. Furthermore, analysis of the results indicates that the photocatalytic degradation of AM follows pseudo first order kinetics for all three types of irradiation (Figure 5.11(b)).
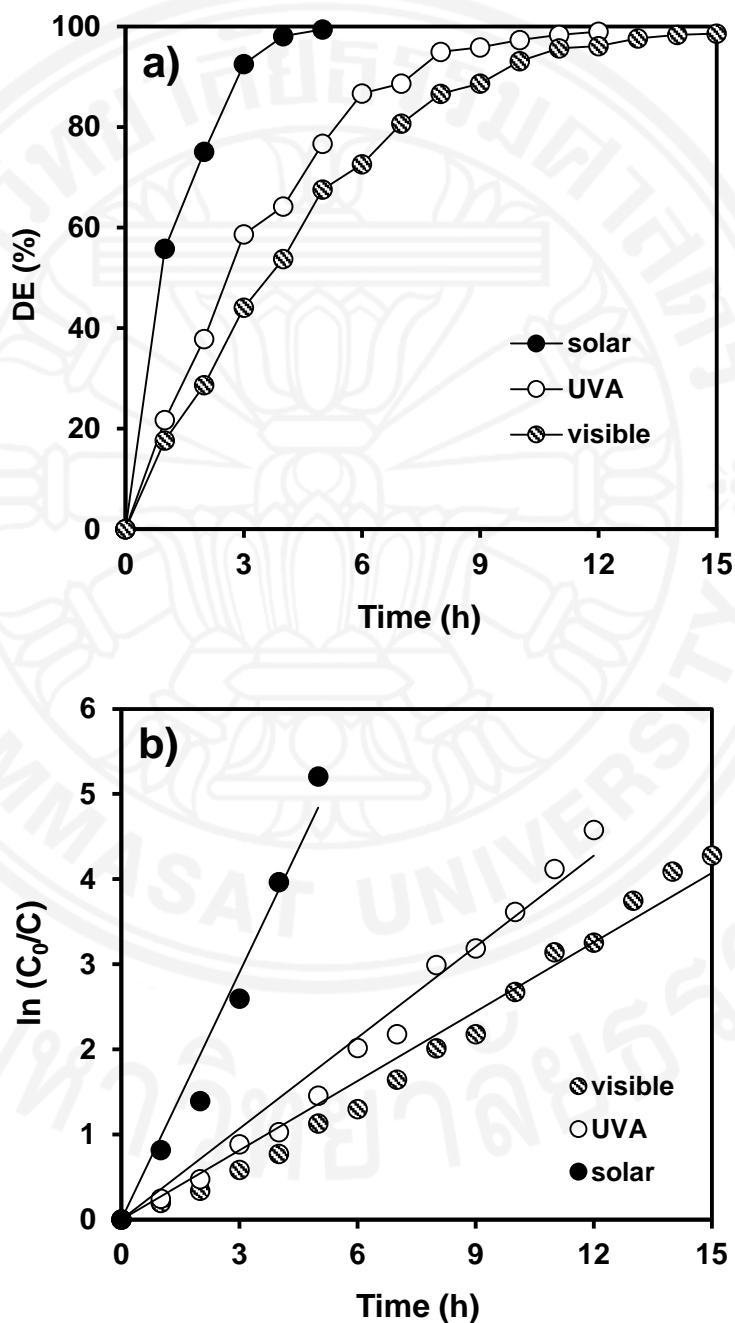
Figure 5.11 Photocatalytic degradation of AM by N-WO$_3$@PF (a) and plots for pseudo first order degradation under different light sources (b) (C_0 = 10 mg/L, pH = 7, v = 80 mL/min, θ = 20°).

5.1.4 Reusability of N-WO$_3$@PF

For reusability evaluation, the photoactive system is used 12 times with similar conditions. As seen in Figure 5.12, small decreases of DE, especially for the photocatalytic degradation under solar and visible light, are observed. After 12 runs, DE under solar, UVA, and visible light decreases from 98.2% to 86.9%, 63.6% to 56.2%, and 56.6% to 41.3%, respectively. These results may be associated with the decrease in the capability of the photoactive system to absorb light, as indicated by the DR spectra shown in Figure 5.4. Another factor may also play a role in the photocatalytic activity reduction. On the basis of SEM and XRD results, it is indicated that the stability of the surface-loaded N-WO$_3$ decreases over time because of the reduced strength of PF support to anchor the N-WO$_3$ particles on the surface. The reduction of PF strength is most likely due to reactive radical attack on the constituent polymer upon irradiation. All of these make the surface-loaded N-WO$_3$ particles susceptible to leaching out. In spite of these facts, overall, the photoactive system N-WO$_3$@PF is shown to be relatively reusable for the photocatalysis of dye using different light sources, as the decline in DE is not very high even after 12 runs.
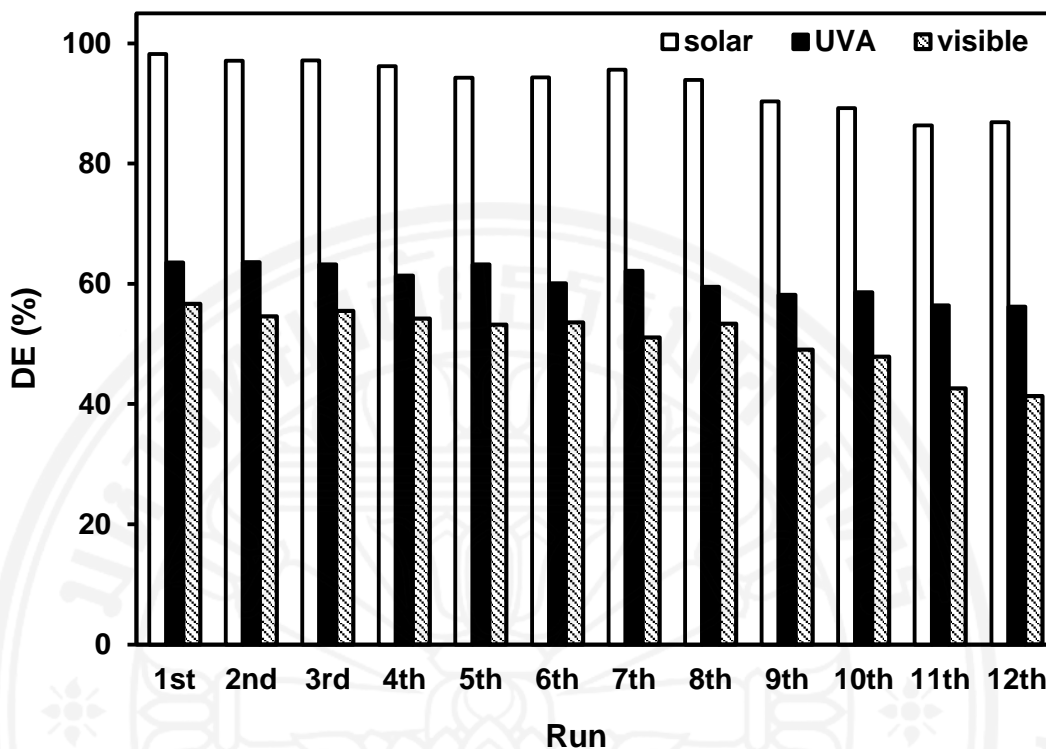
Figure 5.12 Cycling runs of photocatalytic degradation of AM by N-WO$_3$@PF under different light sources (t = 4 h, C_0 = 10 mg/L, pH = 7, v = 80 mL/min, θ = 20°).

5.1.5 IUPAC figures-of-merit

The A_{CO} and A_{CM} for photocatalytic degradation of AM by N-WO$_3$@PF in a TFFBR and those for organic compound degradation by some existing photoactive systems are shown in Table 5.1. The A_{CM} for the degradation of AM with N-WO$_3$@PF in a TFFBR is comparable to those for the degradation of organic compounds by some existing solar photoactive systems. The A_{CO} is found to be lower, indicating that the proposed photoactive system N-WO$_3$@PF in a TFFBR shows a better performance. Overall, N-WO$_3$@PF with a TFFBR is shown to have appreciable photocatalytic performances for degradation of recalcitrant compounds and thus could be a suitable option for solar photocatalysis. Additionally, in comparison with some existing solar photoactive systems, N-WO$_3$@PF in a TFFBR offers simple construction and maintenance, and lower investment costs.

Table 5.1 The A_{CO} and A_{CM} for AM degradation by N-WO$_3$@PF in a TFFBR and those for organic compound degradation by other solar photoactive systems

System	Contaminant	A_{CM} (m^2/g)	A_{CO} (m^2/(m^3 order))	Reference
Fixed bed reactor in continuous flow system[a]; the catalyst (N-WO$_3$) is immobilized on polyester fabric	Amaranth	0.679	2.9	This study
Fixed bed reactor in batch mode; the catalyst (TiO$_2$) is immobilized on pebble	Reactive black 5	0.366	11.2	(Rao et al., 2012)
	Reactive orange 16	0.665	27.3	
	Reactive red 2	0.359	12.2	
	Reactive yellow 84	0.334	9.6	
	Reactive red 141	0.303	8.6	
	Reactive violet 13	0.311	8.6	
Slurry reactor based on photo-Fenton reaction in batch mode with compound parabolic concentrator, CPC	Direct black 38	0.364		(Bandala et al., 2008)
Slurry reactor in batch mode with suspended TiO$_2$; four different solar collector geometries (parabolic trough concentrator, PTC; V trough collector, VTC; flat tubular, FT, and compound parabolic concentrator, CPC) are used	Oxalic acid		7.6 (PTC) 7.4 (VTC) 6.7 (CPC) 11.3 (FT)	(Bandala & Estrada, 2007)
	Carbaryl		11.6 (PTC) 11.5 (VTC) 9.6 (CPC) 16.9 (FT)	

[a]Conditions: $A = 0.04$ m^2, $V = 5 \times 10^{-4}$ m^3, $C_0 = 10$ mg/L; $C_{t = 5 h} = 0.05$ mg/L; pH = 7, $v = 80$ mL/min, $\theta = 20°$, and $t = 5$ h

5.2 Dye degradation by N-ZnO@PF

5.2.1 Properties of N-ZnO@PF

5.2.1.1 Crystallinity and structural properties

Figure 5.13 shows the XRD patterns of PF, N-ZnO@PF, and used N-ZnO@PF. The broad peaks at 16.69°, 17.53°, 22.6°, and 25.42° are the typical XRD pattern of polyester. The presence of N-ZnO after coating is confirmed by the appearance of peaks at 32.05°, 34.71°, and 36.53°, which are of the hexagonal (JCPDS No.36-1451). These sharp, intense peaks indicate good crystallinity of N-ZnO. Small decreases of polyester peak intensities are observed after catalyst coating because of the decreased polymer crystallinity as a result of pretreatment with NaOH and UVC. The further reduction of polyester peak intensities after 12 runs because of decreased crystallinity upon irradiation is also noticeable. This can be due to that the reactive species generated during photocatalysis are able to attack and destroy the polyester structure, leading to crystallinity decrease.
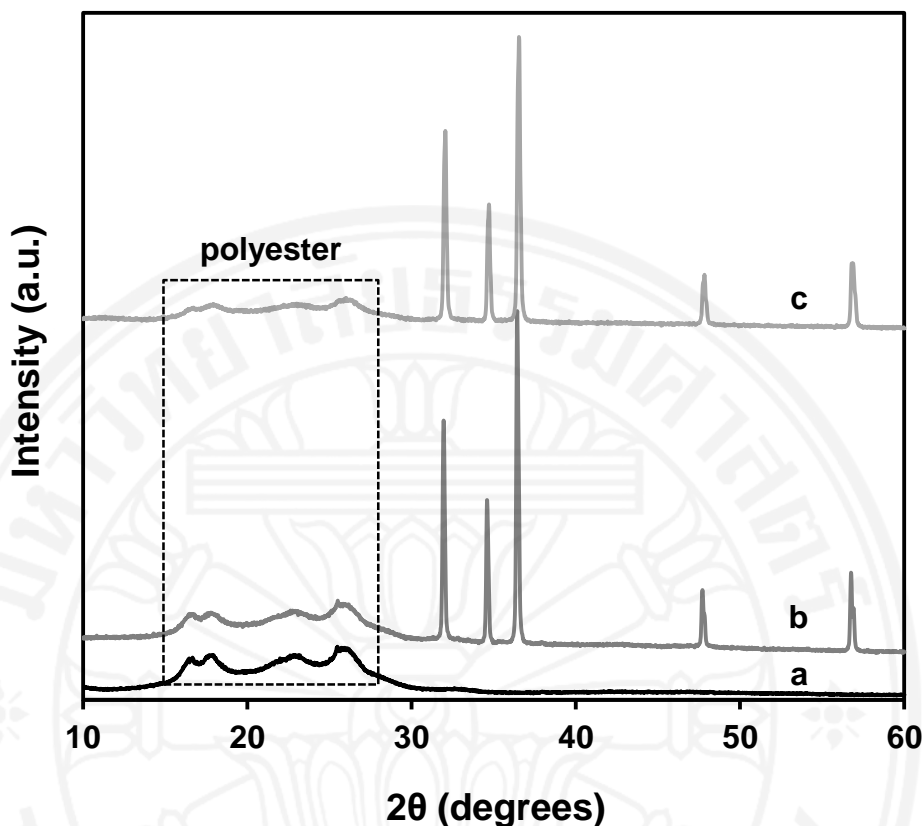
Figure 5.13 The XRD patterns of PF (a), N-ZnO@PF (b), and used N-ZnO@PF (c).

5.2.1.2 Vibrational spectroscopy

Figure 5.14 shows the ATR-FTIR spectra of PF, N-ZnO@PF, and used N-ZnO@PF. As can be seen, the characteristic peaks of PF dominate the observed peaks. The peaks at 1711 cm^{-1} are assigned to saturated esters due to carbonyl stretching. The existence of ester linkages on the PF is confirmed by the presence of peaks at 1089, 1239, and 1338 cm^{-1}. The overtone peaks, corresponding to C–H bonds of the benzene rings, are observed around 1407-1505 cm^{-1}, while the out of plane C–H peaks of benzene rings appear at 721, 870, and 1015 cm^{-1}. A new peak of Zn-O vibration is observed at 536 cm^{-1} after catalyst coating. This peak is not shifted after 12 runs, indicating that the Zn-O bond properties remain unaltered.
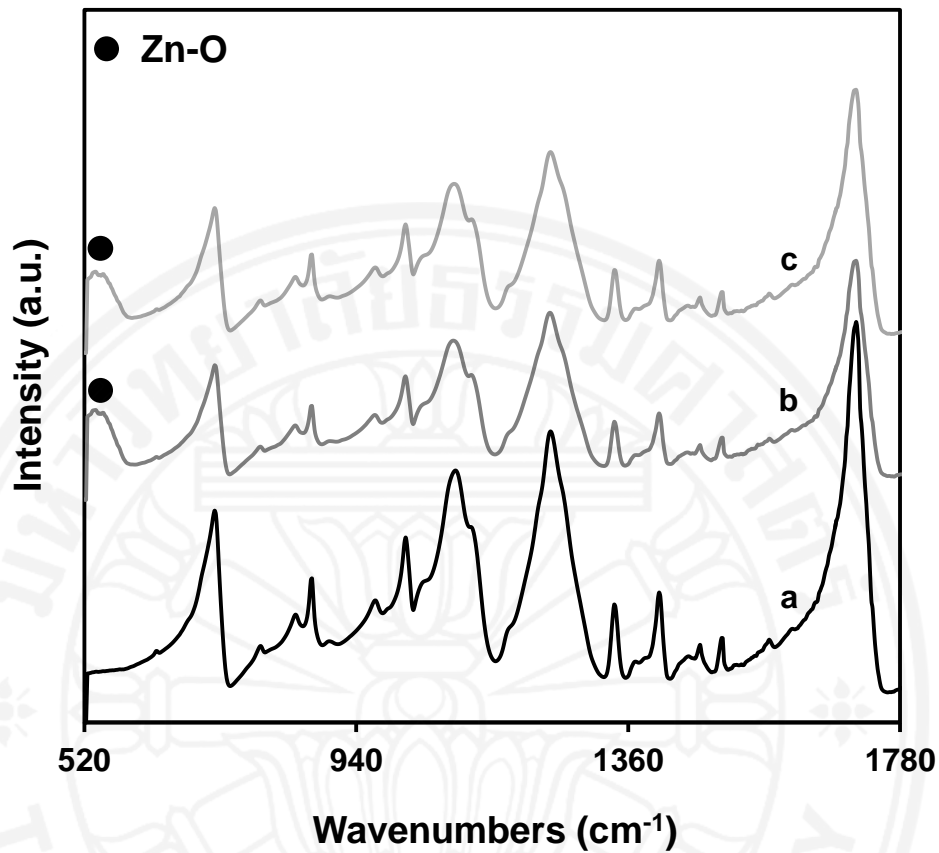
Figure 5.14 The ATR-FTIR spectra of PF (a), N-ZnO@PF (b), and used N-ZnO@PF (c).

5.2.1.3 Morphological properties

Figure 5.15 shows the morphology of PF, N-ZnO@PF, and used N-ZnO@PF. A rough, relatively uniform surface of N-ZnO is observed after coating. The N-ZnO particles can be evenly coated using the heat attachment method. The film of N-ZnO particles is also formed on the fiber surfaces and is not in between them. After 12 runs, the PF surface is not fully covered by the N-ZnO particles (Figure 5.15c). The stability of the N-ZnO particles on the PF surface seems to decrease, likely due to reactive species attack in the PF structure upon irradiation.
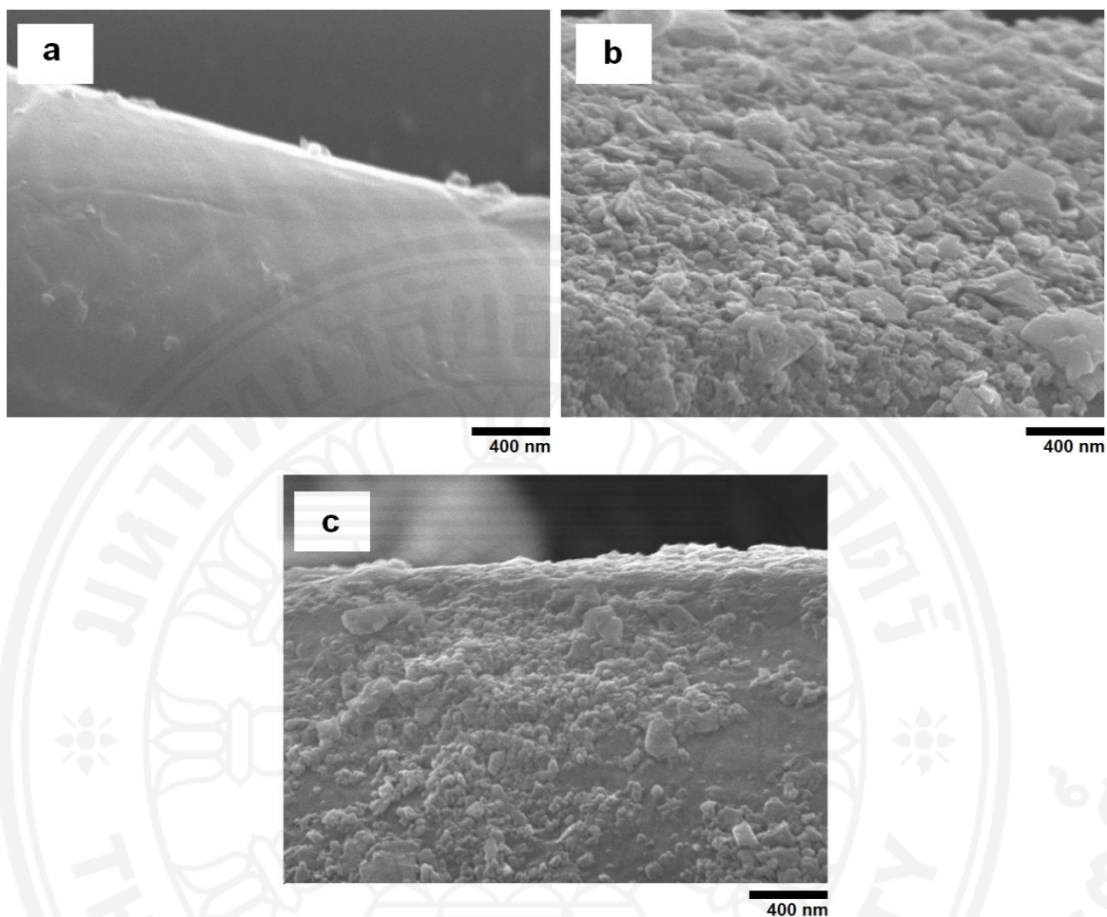
Figure 5.15 SEM images of PF (a), N-ZnO@PF (b), and used N-ZnO@PF (c).

5.2.1.4 Optical properties

Figure 5.16 shows the DRS spectra of PF, N-ZnO@PF, and used N-ZnO@PF. It is shown that PF is unable to absorb light, while N-ZnO@PF shows remarkable absorption of visible light and even NIR light. After 12 runs, a small decrease in the absorbance is observed. This is probably due to alteration in the chemical properties of N dopants upon irradiation which then affects the electronic structure (absorption ability) of the photoactive system.
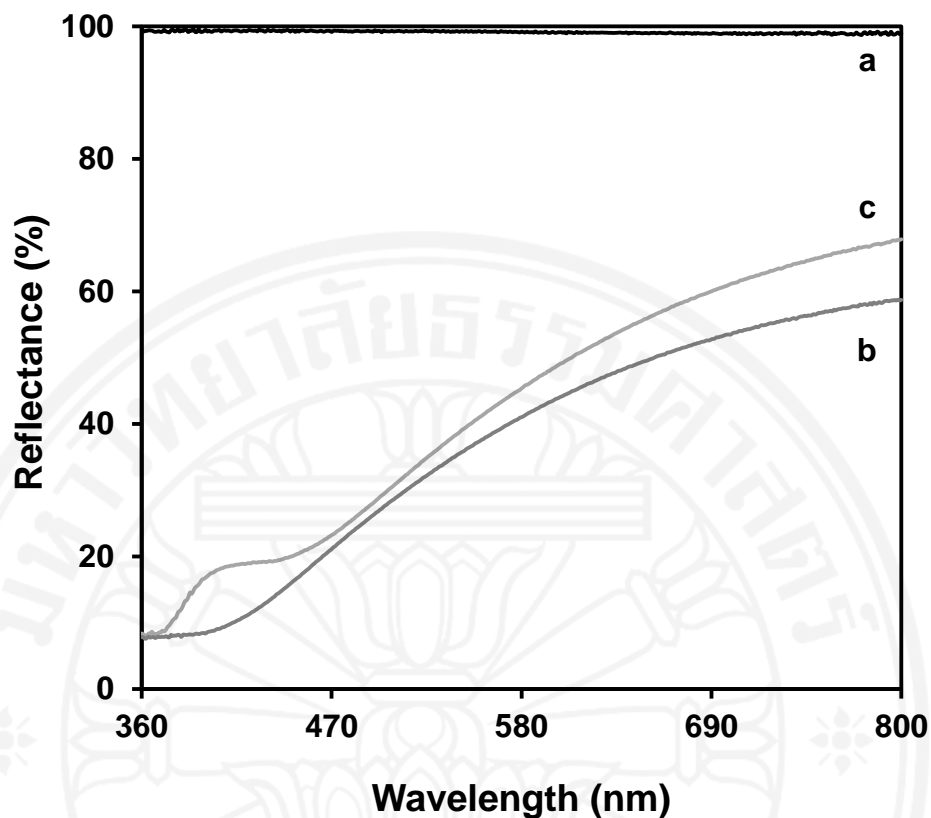
Figure 5.16 DRS spectra of PF (a), N-ZnO@PF (b), and used N-ZnO@PF (c).

5.2.2 Effect of operating parameters on the photocatalytic degradation of AM under solar light

5.2.2.1 Effect of dye concentration

Figure 5.17 shows the photocatalytic degradation of AM at different initial concentrations. The degradation of AM is found to be dependent on the initial AM concentration. The photoactive system can completely degrade 5 mg/L of AM within 12 h. To obtain complete degradation of AM with higher initial concentrations, more time is required. As seen, almost 100% degradation of AM with initial concentrations of 10 and 25 mg/L is observed after 16 and 24 h, respectively.
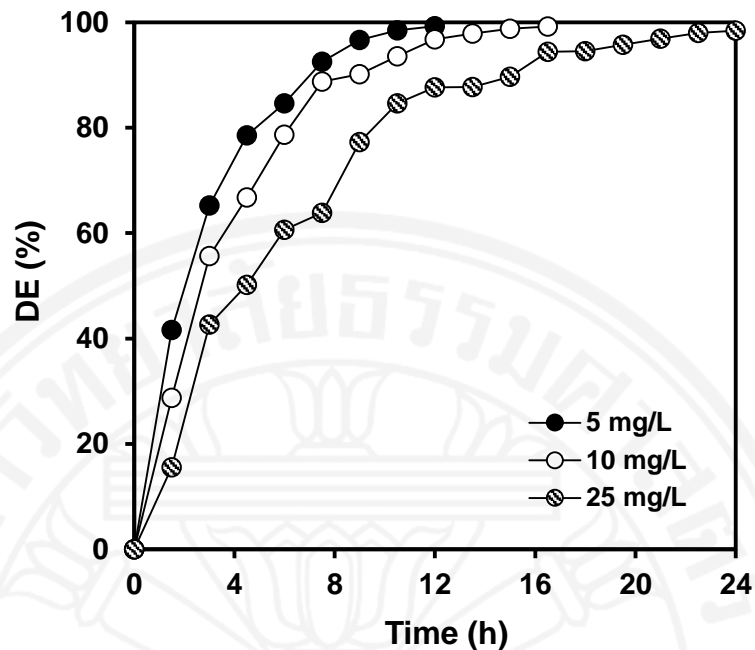
Figure 5.17 Photocatalytic degradation of AM by N-ZnO@PF at different initial AM concentration (pH = 7, v = 80 mL/min, θ = 20°).

5.2.2.2 Effect of pH

Figure 5.18 shows the photocatalytic degradation of 10 mg/L of AM at different pH values. The AM degradation in neutral conditions is more favorable as compared to that in acidic or basic conditions. The efficiencies of AM degradation within 6 h at pH of 7, 5, and 9 are 82.4, 64.4, and 73.6%, respectively. The lower DE at acidic and basic conditions may be due to the reduced stability of the N-ZnO particles on the PF surface. Even though PF is relatively resistant to weak acids and weak bases (Natarajan & Jeyakodi Moses, 2012), it may be hydrolyzed, degrading the surface structure of PF to a certain extent. Moreover, it is worth noting that DE is found to be higher at pH 9 than at pH 5. This is likely due to photocorrosion of N-ZnO at low pH (Fu et al., 2008).

115
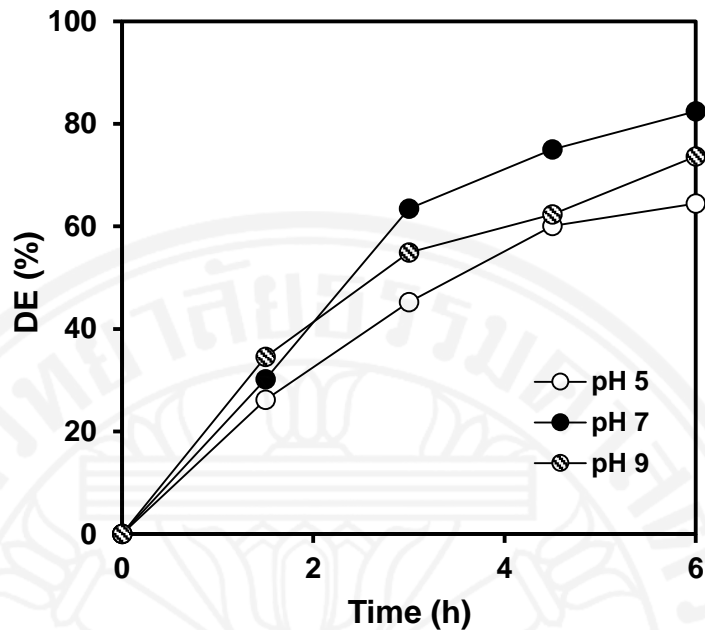
Figure 5.18 Photocatalytic degradation of AM by N-ZnO@PF at different pH ($C_0 =$ 10 mg/L, $v = 80$ mL/min, $\theta = 20°$).

5.2.2.3 Effect of recirculation rate

Figure 5.19 shows the photocatalytic degradation of 10 mg/L of AM at different recirculation rates. One can observe the strong effect of recirculation rate on DE. The higher DE is found at lower recirculation rates. Within 6 h, DE at recirculation rates of 80, 100, and 120 mL/min are 81.6, 70.1, and 62.6%, respectively. It can be seen that the AM degradation favorably takes place at low recirculation rates. As the recirculation rate increases, the average residence time of AM solution decreases. Thus, the contact between AM molecules and N-ZnO@PF is not sufficient to achieve appreciable DE.
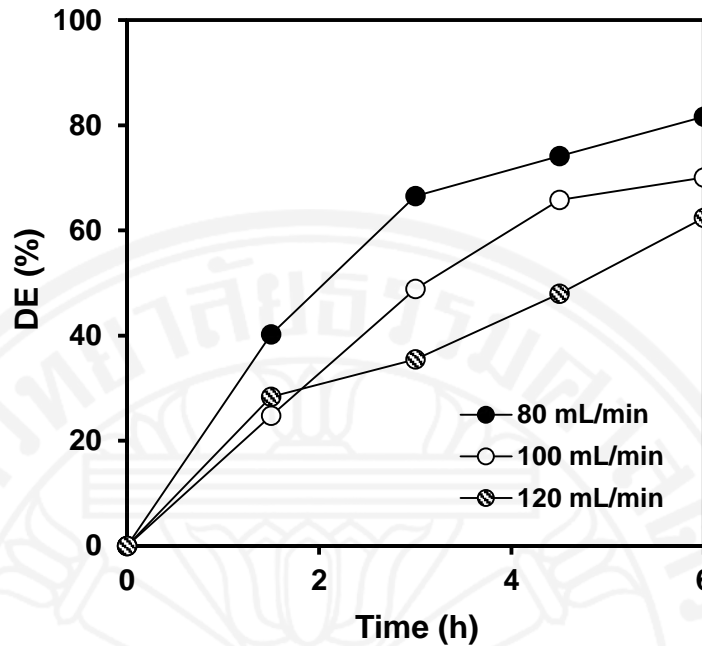
Figure 5.19 Photocatalytic degradation of AM by N-ZnO@PF at different recirculation rates (C_0 = 10 mg/L, pH = 7, θ = 20º).

5.2.2.4 Effect of reactor inclination

Figure 5.20 shows the photocatalytic degradation of 10 mg/L of AM at different inclination angles of sloping plate from the horizontal line. At an inclination angle of 20°, 81.5% of AM is degraded within 6 h, while only 68.4% is degraded at 40°. The AM degradation is favored at lower inclination angles. This is most likely due to that with increasing the inclination angle, the residence time of AM solution decreases, leading to reduced contact between the solution and N-ZnO@PF.
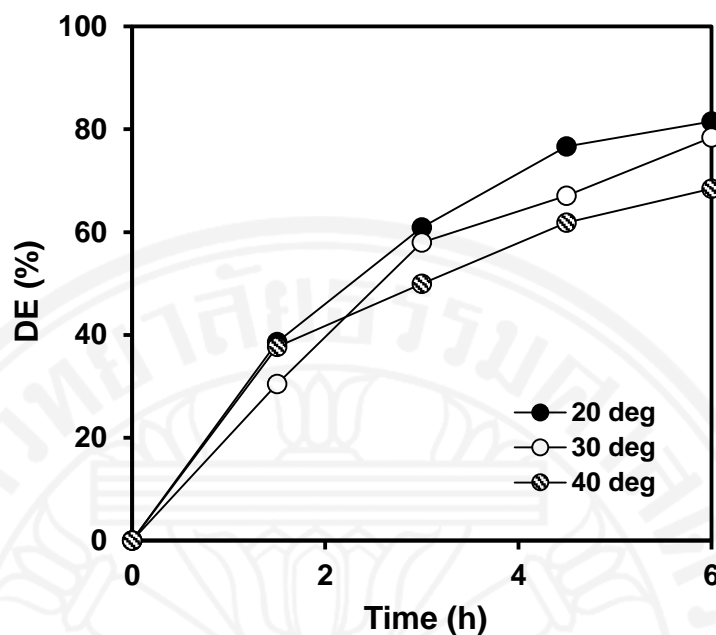
Figure 5.20 Photocatalytic degradation of AM by N-ZnO@PF at different inclination angles (C_0 = 10 mg/L, pH = 7, v = 80 mL/min).

5.2.2.5 Effect of salinity

Figure 5.21 shows the effect of salinity on the degradation of 10 mg/L of AM. DE decreases with increasing salinity. Within 6 h in the absence of NaCl, 83.3% of AM is degraded. Under identical experimental conditions in the presence of 1.2 and 4.8 g/L of NaCl, the efficiencies for the AM degradation are found to be 77.1 and 73.8%, respectively. The inhibition of the AM degradation in the presence of NaCl is probably because Cl$^-$ can displace the OH$^-$ ions bound on the N-ZnO surface (Wang et al., 2013a). As a result, the number of OH$^-$ ions available on the N-ZnO surface is reduced. Due to the fact that OH$^-$ is the source of •OH radical, the generation of •OH is ultimately reduced. Na$^+$ can also participate in the inhibition of the AM degradation due to the adsorption of Na$^+$ on the photoactive system surface. This prevents the AM molecules from accessing the active sites and thus reduces the absorption of the incoming light by the N-ZnO particles. Overall, high salinity of the suspension system is unfavorable for the AM degradation.
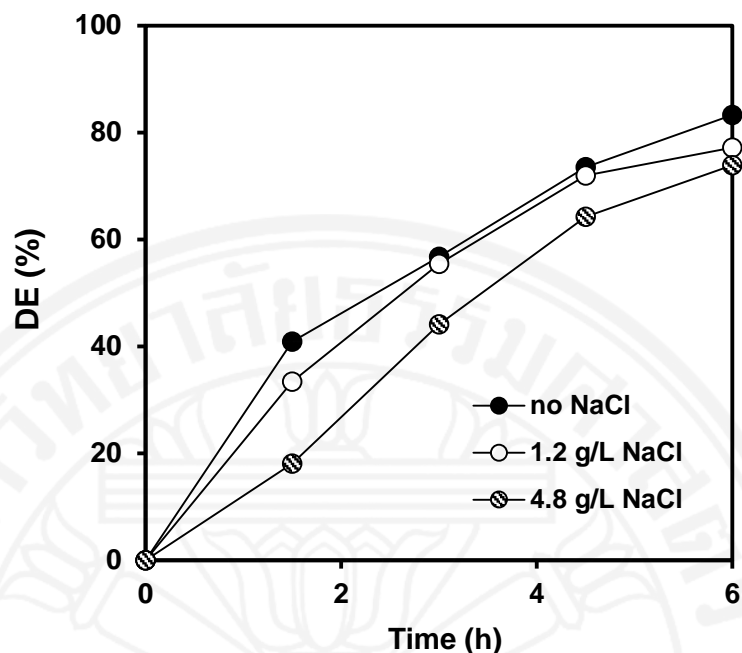
Figure 5.21 Photocatalytic degradation of AM by N-ZnO@PF at different salinity (C_0 = 10 mg/L, pH = 7, v = 80 mL/min, θ = 20º).

5.2.2.6 Effect of inorganic ions

For the degradation of AM by N-ZnO@PF, the inhibition order of inorganic ions based on k_{app} is Ca^{2+} (k_{app} 0.223 h^{-1}) > CO_3^{2-} (k_{app} 0.225 h^{-1}) > NO_3^- (k_{app} 0.251 h^{-1}) > SO_4^{2-} (k_{app} 0.275 h^{-1}). In the absence of inorganic ions, k_{app} is found to be 0.284 h^{-1}. As seen in Figure 5.22, Ca^{2+} inhibits the AM degradation. This is possibly because Ca^{2+} is reduced by the photogenerated electron and is subsequently deposited on the N-ZnO surface. The Ca^0 deposition impedes the adsorption of AM and the absorption of incoming light by the N-ZnO particles. Addition of CO_3^{2-} and NO_3^- also results in decreases of reaction rate, most likely due to the quenching of •OH by CO_3^{2-} (Eq. 4.5) (Guillard et al., 2003a) and the reduction of the generation of •OH as a result of displacement of the surface bound OH$^-$ by NO_3^-. Moreover, SO_4^{2-} insignificantly inhibits the AM degradation because it can form sulfate radical anion (•SO$_4^-$) which further reacts with H_2O producing •OH. The •SO$_4^-$ and •OH can then contribute to the AM degradation.

119
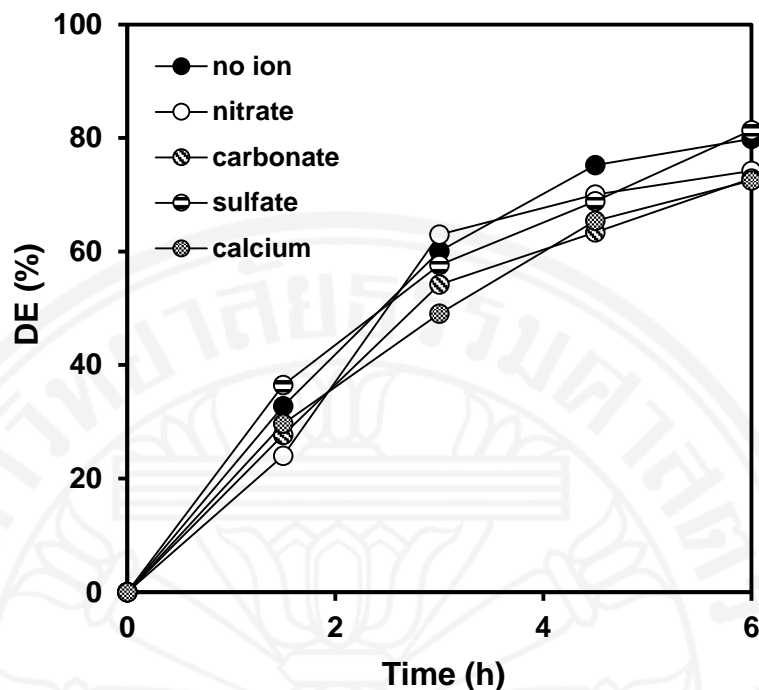
Figure 5.22 Photocatalytic degradation of AM by N-ZnO@PF in the presence of inorganic ions ($C_0 = 10$ mg/L, pH = 7, $v = 80$ mL/min, $\theta = 20^\circ$, ion concentration = 0.05 M).

5.2.3 Reusability of N-ZnO@PF

As shown in Figure 5.23, at solar irradiation of 6 h, DE reaches 78.6%. The DE can be maintained up to 6 runs and then decreases to 52.5% after 12 runs. The results can be explained based on two factors. The first factor is due to the decrease in the capability of the photoactive system to absorb light, as shown in the DRS spectra. The second factor is due to the decreased stability of the surface-loaded N-ZnO particles over time as a result of PF strength reduction. This is indicated by the SEM analysis. The reduction of PF strength is most likely due to reactive radical attack upon irradiation, which makes the coated N-ZnO particles susceptible to leaching out.
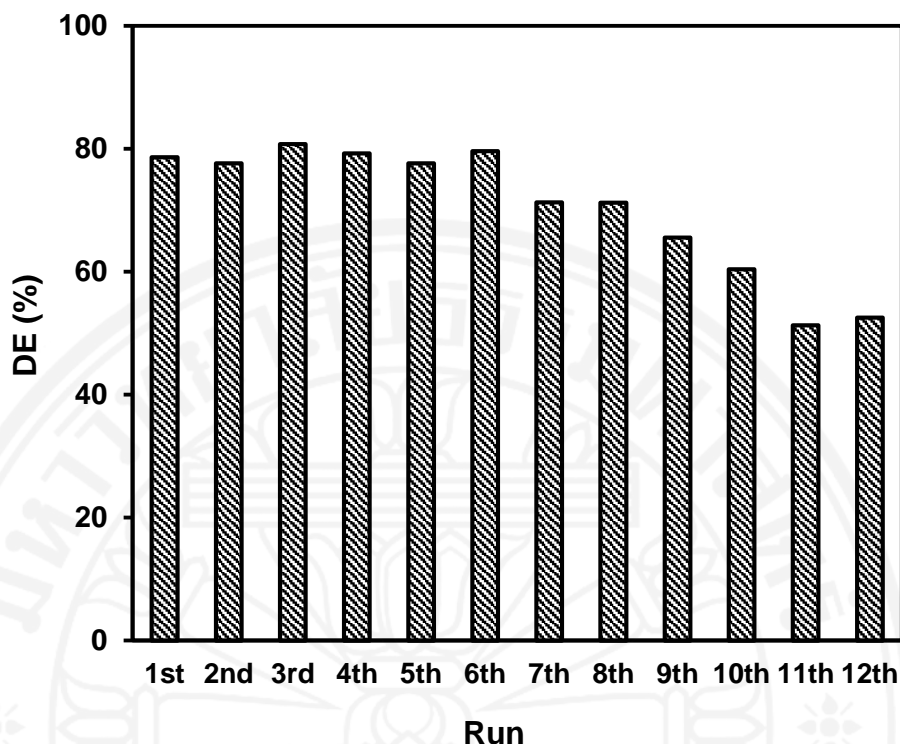
Figure 5.23 Cycling runs of photocatalytic degradation of AM by N-ZnO@PF under different light source (t = 6 h, C_0 = 10 mg/L, pH = 7, v = 80 mL/min, θ = 20º).

5.2.4 IUPAC figures-of-merit

The A_{CO} and A_{CM} for the AM degradation by N-ZnO@PF in a TFFBR are 10.8 $m^2/(m^3$ order) and 0.982 m^2/g, respectively. For comparison, A_{CO} and A_{CM} for organic compound degradation by some existing photoactive systems are shown in Table 5.1. The A_{CM} and A_{CO} for the degradation of AM by N-ZnO@PF in a TFFBR is found to be comparable to those for degradation of organic compounds by some existing solar photoactive systems (Bandala & Estrada, 2007; Bandala et al., 2008; Rao et al., 2012), implying that the proposed photoactive system N-ZnO@PF in a TFFBR shows a comparable performance. Additionally, N-ZnO@PF in a TFFBR features simple construction and maintenance, and low investment costs.

5.3 Dye wastewater treatment with photocatalysis

The dye wastewater from textile industry typically features high concentration of organics, salts and metals, and strong color. In this view, effective treatment of dye wastewater cannot be realized solely by photocatalysis. It needs to be coupled with some processes. Figure 5.24 shows a proposed layout of the treatment of dye wastewater involving photocatalysis. The objective is to convert recalcitrant organic compounds (dyes, surfactants, solvents, lubricants, etc.) into innocuous compounds under ambient conditions. Therefore, those recalcitrant organic compounds are not merely transferred from one phase to another. They are converted to harmless compounds without the formation of any harmful compounds as secondary pollutants.
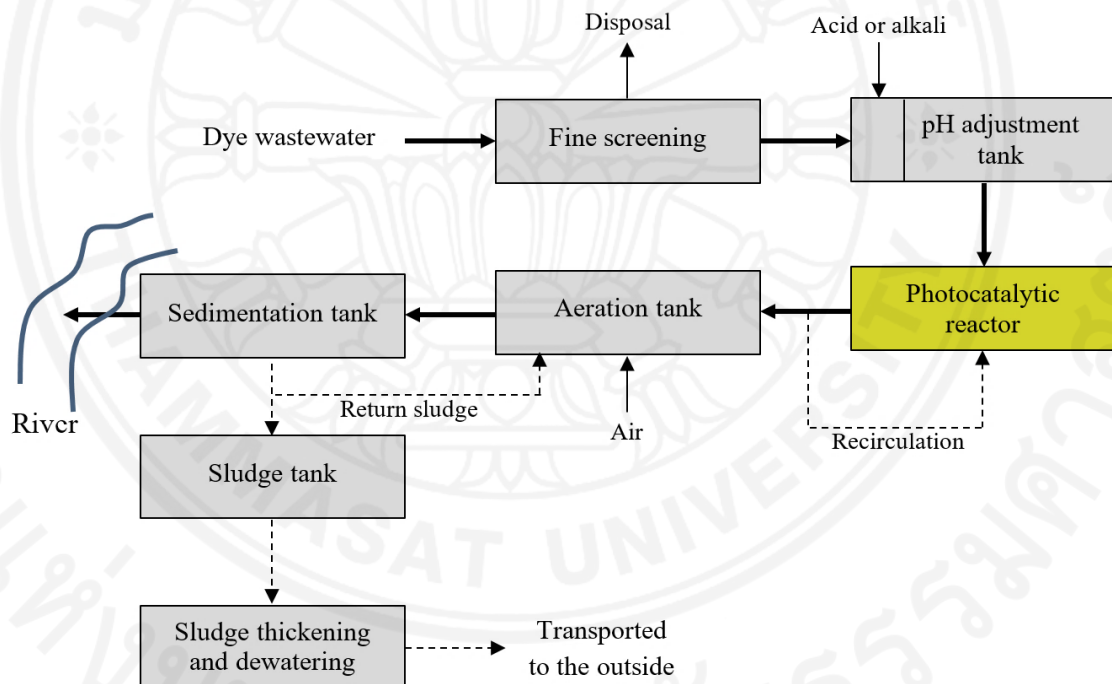
Figure 5.24 Proposed layout of a dye wastewater treatment involving photocatalysis.

As it is known that the prerequisite for effective photocatalytic reaction is the transparency of wastewater. This is to ensure the transmission of incoming light which is used for initiating photocatalytic reaction. For this purpose, additional processes before photocatalysis need to be installed. Fine screening can be the first process. Fine screens with openings of less than 3 mm are able to remove suspended

122

solids and therefore turbidity of the wastewater can be reduced. Reduction of turbidity is furthermore undertaken by pH adjustment to induce precipitation of soluble solids. Metals can also be precipitated by adjusting pH, in which dissolved metals are made insoluble as metal hydroxides or other forms. After considerable turbidity reduction, photocatalysis can now be used to improve biodegradability of dye wastewater for a better efficiency of subsequent biological oxidization. The photocatalysis can be done with a TFFBR consisting of catalyst particles immobilized on a stationary, solid support. The wastewater flows as a thin film which allows effective oxygen transfer. Thus, no additional oxygen supply is required. Finally, biological oxidation is employed after photocatalysis to degrade the remaining small organic compounds. Sedimentation process then follows to separate the sludge. The obtained sludge is partially delivered to sludge tank for further processing. The sludge would also be relatively safe for direct discharge due to the absence of recalcitrant and toxic compounds.

Chapter 6
Conclusions and Recommendations

6.1 Conclusions

Based on the study conducted, the following conclusions can be drawn.

6.1.1 Dye degradation in batch slurry system

- A series of nitrogen-doped metal oxide catalysts namely N-ZnO, N-ZrO$_2$, and N-WO$_3$ with visible light activity can be synthesized by mechanochemically assisted thermal decomposition method.

- Characterization of the N-doped catalysts reveals (i) the presence of N in both interstitial and substitutional sites, (ii) good crystallinity with single phase, (iii) primary particle sizes in the range of 30-60 nm, (iii) significantly increased light absorption in the visible and even up to NIR region, and (iv) increased specific surface area.

- The photocatalytic activities of the N-doped catalysts for the dye degradation are higher compared to those of the pristine catalysts. The amount of urea used for the nitrogen doping greatly affects the photocatalytic activity of the N-doped catalysts. Increasing the amount of urea generally increases the photocatalytic activity.

- The photocatalytic activity order of the N-doped catalysts for the dye degradation is N-WO$_3$ > N-ZnO > N-ZrO$_2$. At the chosen experimental conditions (catalyst concentration of 1 g/L, AM concentration of 10 mg/L, and pH 7), the efficiencies of AM degradation within 2 h by N-WO$_3$, N-ZnO, and N-ZrO$_2$ under visible light of 16.5 W/m^2 are 100, 88.5, and 26.4%, respectively.

- The dye degradation efficiency highly depends on the operating parameters namely initial dye concentration, catalyst concentration, pH, and salinity. The dye degradation efficiency generally increases with increase in catalyst concentration and pH up to a limiting value and with decrease in initial dye concentration and salinity. The dye degradation is favorable in the presence of H$_2$O$_2$.

- The presence of inorganic ions affects the AM degradation at various extents. NO_3^- and NH_4^+ have the least impact, while CO_3^{2-} and Ca^{2+} have the most adverse effect.

- The radiation source and the catalyst used affect the reactive species produced. Superoxide radical and singlet oxygen are the major reactive species in the R6G degradation by N-ZnO and N-ZrO$_2$ under visible light, whereas hydroxyl radicals are shown to be the predominant reactive species under UV light. In the AM degradation by N-WO$_3$ under both visible and UV light, hydroxyl radicals and holes play a main role.

- The photocatalytic activities of the N-doped catalysts can be maintained for six successive runs of the dye degradation, indicating their appreciable stability. Leaching of N dopant is also not observed.

- Although the by-products of the dye degradation are not identified, the photocatalytically treated dye solution are not toxic to the test organisms of *Bacillus cereus*, an agriculturally important soil microorganism. This further proves that the proposed photocatalytic systems are able to convert recalcitrant compounds into innocuous compounds without creating any harmful by-products.

6.1.2 Dye degradation in continuous flow system

- The N-WO$_3$ and N-ZnO particles can be immobilized on the polyester fabric by heat attachment method, forming two photoactive systems.

- Characterization of the photoactive systems reveals (i) formation of a uniform film of the catalyst particles on the fiber surface, (ii) good crystallinity even after being used 12 times, and (iii) remarkable spectral response up to NIR region.

- The photocatalytic activity of N-WO$_3$@PF is higher than that of N-ZnO@PF. At the selected experimental conditions (irradiation time of 4 h, AM concentration of 10 mg/L, pH 7, recirculation rate of 80 mL/min, and inclination angle of 20º), the AM degradation efficiencies by N-WO$_3$@PF and N-ZnO@PF reach 93.1 and 63.4%, respectively.

- UVA and visible light can be used as light sources for the AM degradation by N-WO$_3$@PF in a TFFBR. At the chosen experimental conditions (irradiation time of

4 h, AM concentration of 10 mg/L, pH 7, recirculation rate of 80 mL/min, and inclination angle of 20º), AM degradation efficiencies by N-WO$_3$@PF under solar, UVA, and visible light are found to be 98.2, 63.5, and 56.7%, respectively.

- The AM degradation increases with decreasing initial dye concentration, recirculation rate, reactor inclination, and salinity and is favorable at neutral conditions.

- Inorganic ions inhibitions of the AM degradation by N-WO$_3$@PF and N-ZnO@PF are in the order of Ca^{2+} > CO$_3^{2-}$ > SO$_4^{2-}$ > NO$_3^-$ and Ca^{2+} > CO$_3^{2-}$ > NO$_3^-$ > SO$_4^{2-}$, respectively.

- Photocatalytic activity can still be maintained after successive runs. Small decreases of the photocatalytic activity, especially for N-ZnO@PF, is due to reduced stability of the catalyst particles on the PF surface.

- Based on IUPAC figures-of-merit, the photocatalytic performances of the photoactive systems for the AM degradation in a TFFBR are higher (for NWO$_3$@PF) than or comparable (for N-ZnO@PF) to those of some existing photoactive systems for organic pollutant degradation. Additionally, the proposed photoactive systems feature simple construction, easy maintenance, and low costs of investment and therefore are promising for photocatalysis in a real setting under solar light.

6.2 Recommendations

The following recommendations are proposed based on this study.

- Synthesis parameters other than the amount of N source, such as type of N source, grinding time, calcination time, and calcination temperature, could be investigated to achieve a higher photocatalytic activity. By carrying out these protocols, the dependency of synthesis parameters on the photocatalytic activity could be established. Moreover, grinding of urea-metal precursor mixture could also be replaced by milling. This may result in a more uniform mixture.

- Characterization of the used catalyst particles could be undertaken to understand the effect of photocatalytic operation on the catalyst properties, specifically due to the presence of reactive species and dye degradation products during photocatalytic operation which can lead to catalyst poisoning.

- The range of the operating parameters studied, such as initial dye concentration, salinity, and type of inorganic ions, could be set wider. Thus, more comprehensive results could be obtained.

- To investigate the practical applicability, evaluation of the photocatalytic performance could be done with real textile effluent containing dyes, auxiliary chemicals, and other pollutant matrix.

- Measuring total organic carbon and/or chemical oxygen demand of the photocatalytically treated dye solution would be useful to assess the mineralization extent of parent dyes and intermediate compounds.

- Taking into account the current results, PF is found to be a promising catalyst support. However, some losses of catalyst particles are likely to occur during photocatalytic operation. It might be possible to avoid liberation of catalyst particles by introducing protective layer and/or binder on the photoactive system. These additional compounds might protect the immobilized catalyst particles from reactive species attack during irradiation and from leaching out due to flow of liquid film. The disadvantages would be reduced surface area of the catalyst particles exposed to incoming light and the binder itself might be degraded by the reactive species. Finding suitable protective layer and binder as well as effective method for their incorporation to the photoactive system would be critical.

References

Aftab, U., Khan, M.R., Mahfooz, M., Ali, M., Aslam, S.H., Rehman, A. 2011. Decolourization and degradation of textile azo dyes by Corynebacterium sp. isolated from industrial effluent. *Pakistan Journal of Zoology*, 43(1), 1-8.

Ahmed, M., Idris, A., Adam, A. 2007. Combined anaerobic-aerobic system for treatment of textile wastewater. *Journal of Engineering Science and Technology*, 2(1), 55-69.

Aimable, A., Buscaglia, M.T., Buscaglia, V., Bowen, P. 2010. Polymer-assisted precipitation of ZnO nanoparticles with narrow particle size distribution. *Journal of the European Ceramic Society*, 30(2), 591-598.

Akpan, U., Hameed, B. 2009. Parameters affecting the photocatalytic degradation of dyes using TiO_2-based photocatalysts: a review. *Journal of Hazardous Materials*, 170(2), 520-529.

Alventosa-deLara, E., Barredo-Damas, S., Alcaina-Miranda, M., Iborra-Clar, M. 2012. Ultrafiltration technology with a ceramic membrane for reactive dye removal: Optimization of membrane performance. *Journal of Hazardous Materials*, 209, 492-500.

Antonopoulou, M., Giannakas, A., Deligiannakis, Y., Konstantinou, I. 2013. Kinetic and mechanistic investigation of photocatalytic degradation of the N, N-diethyl-m-toluamide. *Chemical Engineering Journal*, 231, 314-325.

Aouni, A., Fersi, C., Cuartas-Uribe, B., Bes-Pia, A., Alcaina-Miranda, M., Dhahbi, M. 2012. Reactive dyes rejection and textile effluent treatment study using ultrafiltration and nanofiltration processes. *Desalination*, 297, 87-96.

Arabatzis, I., Stergiopoulos, T., Andreeva, D., Kitova, S., Neophytides, S., Falaras, P. 2003. Characterization and photocatalytic activity of Au/TiO_2 thin films for azo-dye degradation. *Journal of Catalysis*, 220(1), 127-135.

Arai, T., Horiguchi, M., Yanagida, M., Gunji, T., Sugihara, H., Sayama, K. 2009. Reaction mechanism and activity of WO$_3$-catalyzed photodegradation of organic substances promoted by a CuO cocatalyst. *The Journal of Physical Chemistry C*, 113(16), 6602-6609.

Asahi, R., Morikawa, T., Irie, H., Ohwaki, T. 2014. Nitrogen-doped titanium dioxide as visible-light-sensitive photocatalyst: Designs, developments, and prospects. *Chemical Reviews*, 114(19), 9824-9852.

Attar, H.M., Rezaee, R. 2006. Investigating the efficiency of advanced photochemical oxidation (APO) technology in degradation of direct azo dye by UV/H$_2$O$_2$ Process. *Journal of Water and Wastewater*, 59, 75-83.

Azbar, N., Yonar, T., Kestioglu, K. 2004. Comparison of various advanced oxidation processes and chemical treatment methods for COD and color removal from a polyester and acetate fiber dyeing effluent. *Chemosphere*, 55(1), 35-43.

Bahnemann, D. 2004. Photocatalytic water treatment: solar energy applications. *Solar Energy*, 77(5), 445-459.

Bahnemann, D.W., Kormann, C., Hoffmann, M.R. 1987. Preparation and characterization of quantum size zinc oxide: a detailed spectroscopic study. *Journal of Physical Chemistry*, 91(14), 3789-3798.

Bandala, E.R., Estrada, C. 2007. Comparison of solar collection geometries for application to photocatalytic degradation of organic contaminants. *Journal of Solar Energy Engineering*, 129(1), 22-26.

Bandala, E.R., Peláez, M.A., García-López, A.J., Salgado, M.d.J., Moeller, G. 2008. Photocatalytic decolourisation of synthetic and real textile wastewater containing benzidine-based azo dyes. *Chemical Engineering and Processing: Process Intensification*, 47(2), 169-176.

Banerjee, S., Pillai, S.C., Falaras, P., O'shea, K.E., Byrne, J.A., Dionysiou, D.D. 2014. New insights into the mechanism of visible light photocatalysis. *The Journal of Physical Chemistry Letters*, 5(15), 2543-2554.

Behnajady, M., Modirshahla, N., Hamzavi, R. 2006. Kinetic study on photocatalytic degradation of CI Acid Yellow 23 by ZnO photocatalyst. *Journal of Hazardous Materials*, 133(1), 226-232.

Behnajady, M.A., Modirshahla, N., Mirzamohammady, M., Vahid, B., Behnajady, B. 2008. Increasing photoactivity of titanium dioxide immobilized on glass plate with optimization of heat attachment method parameters. *Journal of Hazardous Materials*, 160(2), 508-513.

Bessekhouad, Y., Robert, D., Weber, J.-V., Chaoui, N. 2004. Effect of alkaline-doped TiO_2 on photocatalytic efficiency. *Journal of Photochemistry and Photobiology A: Chemistry*, 167(1), 49-57.

Bhattacharyya, K.G., Sharma, A. 2004. Azadirachta indica leaf powder as an effective biosorbent for dyes: a case study with aqueous Congo Red solutions. *Journal of Environmental Management*, 71(3), 217-229.

Bolton, J.R., Bircher, K.G., Tumas, W., Tolman, C.A. 2001. Figures-of-merit for the technical development and application of advanced oxidation technologies for both electric-and solar-driven systems (IUPAC Technical Report). *Pure and Applied Chemistry*, 73(4), 627-637.

Braham, R.J., Harris, A.T. 2009. Review of major design and scale-up considerations for solar photocatalytic reactors. *Industrial & Engineering Chemistry Research*, 48(19), 8890-8905.

Burns, R.A., Crittenden, J.C., Hand, D.W., Selzer, V.H., Sutter, L.L., Salman, S.R. 1999. Effect of inorganic ions in heterogeneous photocatalysis of TCE. *Journal of Environmental Engineering*, 125(1), 77-85.

Champagne, P.-P., Ramsay, J. 2010. Dye decolorization and detoxification by laccase immobilized on porous glass beads. *Bioresource Technology*, 101(7), 2230-2235.

Chan, A.H., Chan, C.K., Barford, J.P., Porter, J.F. 2003. Solar photocatalytic thin film cascade reactor for treatment of benzoic acid containing wastewater. *Water Research*, 37(5), 1125-1135.

Charanpahari, A., Umare, S., Sasikala, R. 2013. Visible light active N doped GeO_2 for the photodegradation of both anionic and cationic dyes. *Catalysis Communications*, 40, 9-12.

Chen, F., Zou, W., Qu, W., Zhang, J. 2009. Photocatalytic performance of a visible light TiO_2 photocatalyst prepared by a surface chemical modification process. *Catalysis Communications*, 10(11), 1510-1513.

Cheryan, M., Rajagopalan, N. 1998. Membrane processing of oily streams. Wastewater treatment and waste reduction. *Journal of Membrane Science*, 151(1), 13-28.

Chong, M.N., Jin, B., Chow, C.W., Saint, C. 2010. Recent developments in photocatalytic water treatment technology: a review. *Water Research*, 44(10), 2997-3027.

Chu, W., Wong, C. 2004. The photocatalytic degradation of dicamba in TiO_2 suspensions with the help of hydrogen peroxide by different near UV irradiations. *Water Research*, 38(4), 1037-1043.

Daneshvar, N., Salari, D., Khataee, A. 2003. Photocatalytic degradation of azo dye acid red 14 in water: investigation of the effect of operational parameters. *Journal of Photochemistry and Photobiology A: Chemistry*, 157(1), 111-116.

Dawood, S., Sen, T.K. 2012. Removal of anionic dye congo red from aqueous solution by raw pine and acid-treated pine cone powder as adsorbent: Equilibrium, thermodynamic, kinetics, mechanism and process design. *Water Research*, 46(6), 1933-1946.

De Lasa, H.I., Serrano, B., Salaices, M. 2005. *Photocatalytic reaction engineering*. Springer, New York.

De Oliveira, R.L., Anderson, M.A., Umbuzeiro, G.D.A., Zocolo, G.J., Zanoni, M.V.B. 2012. Assessment of by-products of chlorination and photoelectrocatalytic chlorination of an azo dye. *Journal of Hazardous Materials*, 205, 1-9.

Di Valentin, C., Finazzi, E., Pacchioni, G., Selloni, A., Livraghi, S., Paganini, M.C., Giamello, E. 2007. N-doped TiO_2: theory and experiment. *Chemical Physics*, 339(1), 44-56.

Dijkstra, M., Buwalda, H., De Jong, A., Michorius, A., Winkelman, J., Beenackers, A. 2001. Experimental comparison of three reactor designs for photocatalytic water purification. *Chemical Engineering Science*, 56(2), 547-555.

Dijkstra, M., Koerts, E., Beenackers, A., Wesselingh, J. 2003. Performance of immobilized photocatalytic reactors in continuous mode. *AIChE Journal*, 49(3), 734-744.

Dionysiou, D.D., Balasubramanian, G., Suidan, M.T., Khodadoust, A.P., Baudin, I., Laîné, J.-M. 2000a. Rotating disk photocatalytic reactor: development, characterization, and evaluation for the destruction of organic pollutants in water. *Water Research*, 34(11), 2927-2940.

Dionysiou, D.D., Suidan, M.T., Bekou, E., Baudin, I., Laîné, J.-M. 2000b. Effect of ionic strength and hydrogen peroxide on the photocatalytic degradation of 4-chlorobenzoic acid in water. *Applied Catalysis B: Environmental*, 26(3), 153-171.

Donelli, I., Freddi, G., Nierstrasz, V.A., Taddei, P. 2010. Surface structure and properties of poly-(ethylene terephthalate) hydrolyzed by alkali and cutinase. *Polymer Degradation and Stability*, 95(9), 1542-1550.

Dong, Y., Bai, Z., Liu, R., Zhu, T. 2007. Preparation of fibrous TiO_2 photocatalyst and its optimization towards the decomposition of indoor ammonia under illumination. *Catalysis Today*, 126(3), 320-327.

Doong, R.-A., Chang, W.-H. 1998. Photodegradation of parathion in aqueous titanium dioxide and zero valent iron solutions in the presence of hydrogen peroxide. *Journal of Photochemistry and Photobiology A: Chemistry*, 116(3), 221-228.

Eskizeybek, V., Sari, F., Gülce, H., Gülce, A., Avci, A. 2012. Preparation of the new polyaniline/ZnO nanocomposite and its photocatalytic activity for degradation of methylene blue and malachite green dyes under UV and natural sun lights irradiations. *Applied Catalysis B: Environmental*, 119, 197-206.

Fang, R., Cheng, X., Xu, X. 2010. Synthesis of lignin-base cationic flocculant and its application in removing anionic azo-dyes from simulated wastewater. *Bioresource Technology*, 101(19), 7323-7329.

Fu, H., Xu, T., Zhu, S., Zhu, Y. 2008. Photocorrosion inhibition and enhancement of photocatalytic activity for ZnO via hybridization with C_{60}. *Environmental Science & Technology*, 42(21), 8064-8069.

Garcia, J., Oliveira, J., Silva, A., Oliveira, C., Nozaki, J., De Souza, N. 2007. Comparative study of the degradation of real textile effluents by photocatalytic reactions involving $UV/TiO_2/H_2O_2$ and $UV/Fe^{2+}/H_2O_2$ systems. *Journal of Hazardous Materials*, 147(1), 105-110.

Guillard, C., Lachheb, H., Houas, A., Ksibi, M., Elaloui, E., Herrmann, J.-M. 2003a. Influence of chemical structure of dyes, of pH and of inorganic salts on their photocatalytic degradation by TiO_2 comparison of the efficiency of powder and supported TiO_2. *Journal of Photochemistry and Photobiology A: Chemistry*, 158(1), 27-36.

Guillard, C., Lachheb, H., Houas, A., Ksibi, M., Elaloui, E., Herrmann, J.-M. 2003b. Influence of chemical structure of dyes, of pH and of inorganic salts on their photocatalytic degradation by TiO_2 comparison of the efficiency of powder and supported TiO_2. *Journal of Photochemistry and Photobiology A: Chemistry*, 158(1), 27-36.

Gupta, V.K., Jain, R., Varshney, S. 2007. Electrochemical removal of the hazardous dye Reactofix Red 3 BFN from industrial effluents. *Journal of Colloid and Interface Science*, 312(2), 292-296.

Haghighatkish, M., Yousefi, M. 1992. Alkaline hydrolysis of polyester fibers-structural effects. *Iranian Journal of Polymer Science and Technology*, 1(2), 56-61.

Han, Z., Chang, V.W., Zhang, L., Tse, M.S., Tan, O.K., Hildemann, L.M. 2012. Preparation of TiO_2-coated polyester fiber filter by spray-coating and its photocatalytic degradation of gaseous formaldehyde. *Aerosol and Air Quality Research*, 12, 1327-1335.

Hashemizad, S., Montazer, M., Rashidi, A. 2012. Influence of the surface hydrolysis on the functionality of poly (ethylene terephthalate) fabric treated with nanotitanium dioxide. *Journal of Applied Polymer Science*, 125(2), 1176-1184.

Hirakawa, T., Nosaka, Y. 2002. Properties of O_2-and OH formed in TiO_2 aqueous suspensions by photocatalytic reaction and the influence of H_2O_2 and some ions. *Langmuir*, 18(8), 3247-3254.

Hosseini, S., Borghei, S., Vossoughi, M., Taghavinia, N. 2007. Immobilization of TiO_2 on perlite granules for photocatalytic degradation of phenol. *Applied Catalysis B: Environmental*, 74(1), 53-62.

133

Jaimes-Ramírez, R., Vergara-Sánchez, J., Silva Martinez, S. 2012. Solar assisted degradation of acid orange 7 textile dye in aqueous solutions by Ce-doped TiO$_2$. *Mexican Journal of Scientific Research*, 1(1), 42-55.

Jiang, D., Xu, Y., Wu, D., Sun, Y. 2008. Visible-light responsive dye-modified TiO$_2$ photocatalyst. *Journal of Solid State Chemistry*, 181(3), 593-602.

Joseph, J.M., Destaillats, H., Hung, H.-M., Hoffmann, M.R. 2000. The sonochemical degradation of azobenzene and related azo dyes: rate enhancements via Fenton's reactions. *The Journal of Physical Chemistry A*, 104(2), 301-307.

Jung, S., Yong, K. 2011. Fabrication of CuO–ZnO nanowires on a stainless steel mesh for highly efficient photocatalytic applications. *Chemical Communications*, 47(9), 2643-2645.

Karadag, D., Tok, S., Akgul, E., Ulucan, K., Evden, H., Kaya, M.A. 2006. Combining adsorption and coagulation for the treatment of azo and anthraquinone dyes from aqueous solution. *Industrial & Engineering Chemistry Research*, 45(11), 3969-3973.

Karches, M., Morstein, M., Von Rohr, P.R., Pozzo, R.L., Giombi, J.L., Baltanás, M.A. 2002. Plasma-CVD-coated glass beads as photocatalyst for water decontamination. *Catalysis Today*, 72(3), 267-279.

Kasiri, M., Aleboyeh, H., Aleboyeh, A. 2008. Degradation of Acid Blue 74 using Fe-ZSM5 zeolite as a heterogeneous photo-Fenton catalyst. *Applied Catalysis B: Environmental*, 84(1), 9-15.

Kaur, S., Singh, V. 2007. Visible light induced sonophotocatalytic degradation of Reactive Red dye 198 using dye sensitized TiO$_2$. *Ultrasonics Sonochemistry*, 14(5), 531-537.

Kaushik, P., Malik, A. 2009. Fungal dye decolourization: recent advances and future potential. *Environment International*, 35(1), 127-141.

Khan, S.J., Reed, R.H., Rasul, M.G. 2012. Thin-film fixed-bed reactor (TFFBR) for solar photocatalytic inactivation of aquaculture pathogen Aeromonas hydrophila. *BMC Microbiology*, 12(1), 5.

Khataee, A., Pons, M.-N., Zahraa, O. 2009. Photocatalytic degradation of three azo dyes using immobilized TiO_2 nanoparticles on glass plates activated by UV light irradiation: influence of dye molecular structure. *Journal of Hazardous Materials*, 168(1), 451-457.

Khouni, I., Marrot, B., Moulin, P., Amar, R.B. 2011. Decolourization of the reconstituted textile effluent by different process treatments: Enzymatic catalysis, coagulation/flocculation and nanofiltration processes. *Desalination*, 268(1), 27-37.

Kim, S.-H. 2006. *Functional dyes*. Elsevier Science, Amsterdam, The Netherlands.

Kim, T.-H., Park, C., Shin, E.-B., Kim, S. 2002. Decolorization of disperse and reactive dyes by continuous electrocoagulation process. *Desalination*, 150(2), 165-175.

Konstantinou, I.K., Albanis, T.A. 2004a. TiO_2-assisted photocatalytic degradation of azo dyes in aqueous solution: kinetic and mechanistic investigations: a review. *Applied Catalysis B: Environmental*, 49(1), 1-14.

Konstantinou, I.K., Albanis, T.A. 2004b. TiO_2-assisted photocatalytic degradation of azo dyes in aqueous solution: kinetic and mechanistic investigations: A review. *Applied Catalysis B: Environmental*, 49(1), 1-14.

Le-Clech, P., Chen, V., Fane, T.A. 2006. Fouling in membrane bioreactors used in wastewater treatment. *Journal of Membrane Science*, 284(1), 17-53.

Lee, J.-W., Choi, S.-P., Thiruvenkatachari, R., Shim, W.-G., Moon, H. 2006. Evaluation of the performance of adsorption and coagulation processes for the maximum removal of reactive dyes. *Dyes and Pigments*, 69(3), 196-203.

Li, X., Chen, C., Zhao, J. 2001. Mechanism of photodecomposition of H_2O_2 on TiO_2 surfaces under visible light irradiation. *Langmuir*, 17(13), 4118-4122.

Li, X., Xiao, W., He, G., Zheng, W., Yu, N., Tan, M. 2012. Pore size and surface area control of MgO nanostructures using a surfactant-templated hydrothermal process: High adsorption capability to azo dyes. *Colloids and Surfaces A: Physicochemical and Engineering Aspects*, 408, 79-86.

Lin, C.-C., Chiang, Y.-J. 2012. Feasibility of using a rotating packed bed in preparing coupled ZnO/SnO_2 photocatalysts. *Journal of Industrial and Engineering Chemistry*, 18(4), 1233-1236.

135

Liu, G., Wang, L., Yang, H.G., Cheng, H.-M., Lu, G.Q.M. 2010. Titania-based photocatalysts-crystal growth, doping and heterostructuring. *Journal of Materials Chemistry*, 20(5), 831-843.

Liu, Y., Li, Y., Li, W., Han, S., Liu, C. 2012. Photoelectrochemical properties and photocatalytic activity of nitrogen-doped nanoporous WO_3 photoelectrodes under visible light. *Applied Surface Science*, 258(12), 5038-5045.

Ma, C., Xu, J., Liu, X. 2006. Decomposition of an azo dye in aqueous solution by combination of ultrasound and visible light. *Ultrasonics*, 44, 375-378.

Marandi, R., Olya, M.E., Vahid, B., Khosravi, M., Hatami, M. 2012. Kinetic modeling of photocatalytic degradation of an azo dye using nano-TiO_2/polyester. *Environmental Engineering Science*, 29(10), 957-963.

Matos, J., Júnior, F.A., Cavalcante, L., Santos, V., Leal, S., Júnior, L.S., Santos, M., Longo, E. 2009. Reflux synthesis and hydrothermal processing of ZrO_2 nanopowders at low temperature. *Materials Chemistry and Physics*, 117(2), 455-459.

Mejía, M., Marín, J., Restrepo, G., Pulgarín, C., Kiwi, J. 2011. Photocatalytic evaluation of TiO_2/nylon systems prepared at different impregnation times. *Catalysis Today*, 161(1), 15-22.

Mejia, M., Marin, J., Restrepo, G., Pulgarin, C., Mielczarski, E., Mielczarski, J., Arroyo, Y., Lavanchy, J.-C., Kiwi, J. 2009. Self-cleaning modified TiO_2–cotton pretreated by UVC-light (185nm) and RF-plasma in vacuum and also under atmospheric pressure. *Applied Catalysis B: Environmental*, 91(1), 481-488.

Mejia, M., Marin, J., Restrepo, G., Rios, L., Pulgarin, C., Kiwi, J. 2010. Preparation, testing and performance of a TiO_2/polyester photocatalyst for the degradation of gaseous methanol. *Applied Catalysis B: Environmental*, 94(1), 166-172.

Milošev, I., Strehblow, H.-H., Navinšek, B. 1997. Comparison of TiN, ZrN and CrN hard nitride coatings: Electrochemical and thermal oxidation. *Thin Solid Films*, 303(1), 246-254.

Milošev, I., Strehblow, H.H., Gaberšček, M., Navinšek, B. 1996. Electrochemical oxidation of ZrN hard (PVD) coatings studied by XPS. *Surface and Interface Analysis*, 24(7), 448-458.

Moafi, H.F., Shojaie, A.F., Zanjanchi, M.A. 2010. The comparison of photocatalytic activity of synthesized TiO_2 and ZrO_2 nanosize onto wool fibers. *Applied Surface Science*, 256(13), 4310-4316.

Mozia, S. 2010. Photocatalytic membrane reactors (PMRs) in water and wastewater treatment. A review. *Separation and Purification Technology*, 73(2), 71-91.

Naik, G.K., Mishra, P.M., Parida, K. 2013. Green synthesis of Au/TiO_2 for effective dye degradation in aqueous system. *Chemical Engineering Journal*, 229, 492-497.

Nakajima, H., Tong-on, A., Sumano, N., Sittisard, K., Rattanasuporn, S., Euaruksakul, C., Supruangnet, R., Jearanaikoon, N., Photongkam, P., Chanlek, N. 2013. Photoemission spectroscopy and photoemission electron microscopy beamline at the Siam Photon Laboratory. *Journal of Physics: Conference Series*. IOP Publishing. pp. 132020.

Nataraj, S., Hosamani, K., Aminabhavi, T. 2009. Nanofiltration and reverse osmosis thin film composite membrane module for the removal of dye and salts from the simulated mixtures. *Desalination*, 249(1), 12-17.

Natarajan, S., Jeyakodi Moses, J. 2012. Surface modification of polyester fabric using polyvinyl alcohol in alkaline medium. *Indian Journal of Fibre and Textile Research*, 37(3), 287.

Navio, J., Hidalgo, M., Colon, G., Botta, S., Litter, M. 2001. Preparation and physicochemical properties of ZrO_2 and Fe/ZrO_2 prepared by a sol-gel technique. *Langmuir*, 17(1), 202-210.

Nogueira, H.I., Cavaleiro, A.M., Rocha, J., Trindade, T., de Jesus, J.D.P. 2004. Synthesis and characterization of tungsten trioxide powders prepared from tungstic acids. *Materials Research Bulletin*, 39(4), 683-693.

Noorjahan, M., Kumari, V.D., Subrahmanyam, M., Boule, P. 2004. A novel and efficient photocatalyst: TiO_2-HZSM-5 combinate thin film. *Applied Catalysis B: Environmental*, 47(3), 209-213.

Noorjahan, M., Reddy, M.P., Kumari, V.D., Lavedrine, B., Boule, P., Subrahmanyam, M. 2003. Photocatalytic degradation of H-acid over a novel TiO_2 thin film fixed bed reactor and in aqueous suspensions. *Journal of Photochemistry and Photobiology A: Chemistry*, 156(1), 179-187.

Ntwaeaborwa, O.M., Holloway, P. 2005. Enhanced photoluminescence of Ce^{3+} induced by an energy transfer from ZnO nanoparticles encapsulated in SiO_2. *Nanotechnology*, 16(6), 865.

Oliveira, F.H., Osugi, M.E., Paschoal, F.M., Profeti, D., Olivi, P., Zanoni, M.V.B. 2007. Electrochemical oxidation of an acid dye by active chlorine generated using $Ti/Sn_{(1-x)}Ir_xO_2$ electrodes. *Journal of Applied Electrochemistry*, 37(5), 583-592.

Ollis, D.F., Pelizzetti, E., Serpone, N. 1991. Photocatalyzed destruction of water contaminants. *Environmental Science & Technology*, 25(9), 1522-1529.

Palomino, J.-C., Martin, A., Camacho, M., Guerra, H., Swings, J., Portaels, F. 2002. Resazurin microtiter assay plate: simple and inexpensive method for detection of drug resistance in Mycobacterium tuberculosis. *Antimicrobial Agents and Chemotherapy*, 46(8), 2720-2722.

Patil, A.B., Patil, K.R., Pardeshi, S.K. 2010. Ecofriendly synthesis and solar photocatalytic activity of S-doped ZnO. *Journal of Hazardous Materials*, 183(1), 315-323.

Patil, A.B., Patil, K.R., Pardeshi, S.K. 2011. Enhancement of oxygen vacancies and solar photocatalytic activity of zinc oxide by incorporation of nonmetal. *Journal of Solid State Chemistry*, 184(12), 3273-3279.

Pelaez, M., Nolan, N.T., Pillai, S.C., Seery, M.K., Falaras, P., Kontos, A.G., Dunlop, P.S., Hamilton, J.W., Byrne, J.A., O'Shea, K. 2012. A review on the visible light active titanium dioxide photocatalysts for environmental applications. *Applied Catalysis B: Environmental*, 125, 331-349.

Pfeifer, J., Guifang, C., Tekula-Buxbaum, P., Kiss, B., Farkas-Jahnke, M., Vadasdi, K. 1995. A reinvestigation of the preparation of tungsten oxide hydrate WO_3, $1/3H_2O$. *Journal of Solid State Chemistry*, 119(1), 90-97.

Pucher, P., Benmami, M., Azouani, R., Krammer, G., Chhor, K., Bocquet, J.-F., Kanaev, A. 2007. Nano-TiO_2 sols immobilized on porous silica as new efficient photocatalyst. *Applied Catalysis A: General*, 332(2), 297-303.

Qin, H., Li, W., Xia, Y., He, T. 2011. Photocatalytic activity of heterostructures based on ZnO and N-doped ZnO. *ACS Applied Materials & Interfaces*, 3(8), 3152-3156.

138

Quesada-Cabrera, R., Sotelo-Vazquez, C., Darr, J.A., Parkin, I.P. 2014. Critical influence of surface nitrogen species on the activity of N-doped TiO_2 thin-films during photodegradation of stearic acid under UV light irradiation. *Applied Catalysis B: Environmental*, 160, 582-588.

Rahal, R., Pigot, T., Foix, D., Lacombe, S. 2011. Photocatalytic efficiency and self-cleaning properties under visible light of cotton fabrics coated with sensitized TiO_2. *Applied Catalysis B: Environmental*, 104(3), 361-372.

Rao, K.V.S., Rachel, A., Subrahmanyam, M., Boule, P. 2003. Immobilization of TiO_2 on pumice stone for the photocatalytic degradation of dyes and dye industry pollutants. *Applied Catalysis B: Environmental*, 46(1), 77-85.

Rao, M., Rajeshwar, K., Verneker, V.P., DuBow, J. 1980. Photosynthetic production of hydrogen and hydrogen peroxide on semiconducting oxide grains in aqueous solutions. *The Journal of Physical Chemistry*, 84(15), 1987-1991.

Rao, N.N., Chaturvedi, V., Puma, G.L. 2012. Novel pebble bed photocatalytic reactor for solar treatment of textile wastewater. *Chemical Engineering Journal*, 184, 90-97.

Reddy, S., Sivaramakrishna, L., Varada Reddy, A. 2012. The use of an agricultural waste material, Jujuba seeds for the removal of anionic dye (Congo red) from aqueous medium. *Journal of Hazardous Materials*, 203, 118-127.

Rehman, S., Ullah, R., Butt, A., Gohar, N. 2009. Strategies of making TiO_2 and ZnO visible light active. *Journal of Hazardous Materials*, 170(2), 560-569.

Ren, X. 2000. Development of environmental performance indicators for textile process and product. *Journal of Cleaner Production*, 8(6), 473-481.

Rieger, P.-G., Meier, H.-M., Gerle, M., Vogt, U., Groth, T., Knackmuss, H.-J. 2002. Xenobiotics in the environment: present and future strategies to obviate the problem of biological persistence. *Journal of Biotechnology*, 94(1), 101-123.

Robinson, T., McMullan, G., Marchant, R., Nigam, P. 2001. Remediation of dyes in textile effluent: a critical review on current treatment technologies with a proposed alternative. *Bioresource Technology*, 77(3), 247-255.

Sani, R.K., Banerjee, U.C. 1999. Decolorization of triphenylmethane dyes and textile and dye-stuff effluent by *Kurthia sp*. *Enzyme and Microbial Technology*, 24(7), 433-437.

Shanthi, M., Kuzhalosai, V. 2012. Photocatalytic degradation of an azo dye, Acid Red 27, in aqueous solution using nano ZnO. *Indian Journal of Chemistry A*, 51(3), 428.

Shifu, C., Wei, Z., Sujuan, Z., Wei, L. 2009. Preparation, characterization and photocatalytic activity of N-containing ZnO powder. *Chemical Engineering Journal*, 148(2), 263-269.

Shu, H.-Y., Chang, M.-C., Fan, H.-J. 2004. Decolorization of azo dye acid black 1 by the UV/H_2O_2 process and optimization of operating parameters. *Journal of Hazardous Materials*, 113(1), 201-208.

Silva, A.C., Pic, J.S., Sant'Anna, G.L., Dezotti, M. 2009. Ozonation of azo dyes (Orange II and Acid Red 27) in saline media. *Journal of Hazardous Materials*, 169(1), 965-971.

Stefan, M.I., Hoy, A.R., Bolton, J.R. 1996. Kinetics and mechanism of the degradation and mineralization of acetone in dilute aqueous solution sensitized by the UV photolysis of hydrogen peroxide. *Environmental Science & Technology*, 30(7), 2382-2390.

Sun, J., Qiao, L., Sun, S., Wang, G. 2008. Photocatalytic degradation of Orange G on nitrogen-doped TiO_2 catalysts under visible light and sunlight irradiation. *Journal of Hazardous Materials*, 155(1), 312-319.

Tauber, M.M., Gübitz, G.M., Rehorek, A. 2008. Degradation of azo dyes by oxidative processes–Laccase and ultrasound treatment. *Bioresource Technology*, 99(10), 4213-4220.

Thio, B.J.R., Montes, M.O., Mahmoud, M.A., Lee, D.-W., Zhou, D., Keller, A.A. 2011. Mobility of capped silver nanoparticles under environmentally relevant conditions. *Environmental Science & Technology*, 46(13), 6985-6991.

Uddin, M., Hasnat, M., Samed, A., Majumdar, R. 2007. Influence of TiO_2 and ZnO photocatalysts on adsorption and degradation behaviour of Erythrosine. *Dyes and Pigments*, 75(1), 207-212.

Vajnhandl, S., Le Marechal, A.M. 2007. Case study of the sonochemical decolouration of textile azo dye Reactive Black 5. *Journal of Hazardous Materials*, 141(1), 329-335.

Van der Bruggen, B., Curcio, E., Drioli, E. 2004. Process intensification in the textile industry: the role of membrane technology. *Journal of Environmental Management*, 73(3), 267-274.

Wang, D., Li, Y., Li, G., Wang, C., Zhang, W., Wang, Q. 2013a. Modeling of quantitative effects of water components on the photocatalytic degradation of 17α-ethynylestradiol in a modified flat plate serpentine reactor. *Journal of Hazardous Materials*, 254, 64-71.

Wang, D., Zhang, J., Luo, Q., Li, X., Duan, Y., An, J. 2009. Characterization and photocatalytic activity of poly (3-hexylthiophene)-modified TiO_2 for degradation of methyl orange under visible light. *Journal of Hazardous Materials*, 169(1), 546-550.

Wang, H.-D., Yang, Q., Niu, C.H., Badea, I. 2012. Adsorption of azo dye onto nanodiamond surface. *Diamond and Related Materials*, 26, 1-6.

Wang, J., Liu, P., Fu, X., Li, Z., Han, W., Wang, X. 2008. Relationship between oxygen defects and the photocatalytic property of ZnO nanocrystals in nafion membranes. *Langmuir*, 25(2), 1218-1223.

Wang, Y., Feng, C., Zhang, M., Yang, J., Zhang, Z. 2011a. Visible light active N-doped TiO_2 prepared from different precursors: origin of the visible light absorption and photoactivity. *Applied Catalysis B: Environmental*, 104(3), 268-274.

Wang, Z., Xuan, J., Liu, B., He, J. 2013b. Photocatalytic degradation of CI reactive blue 19 by using novel nano $BiVO_4$-coated cotton fabric. *Journal of Industrial Textiles*, 1528083713518088.

Wang, Z., Yuan, R., Guo, Y., Xu, L., Liu, J. 2011b. Effects of chloride ions on bleaching of azo dyes by Co^{2+}/oxone regent: Kinetic analysis. *Journal of Hazardous Materials*, 190(1), 1083-1087.

Wu, C., Shen, L., Huang, Q., Zhang, Y.-C. 2011. Hydrothermal synthesis and characterization of Bi_2O_3 nanowires. *Materials Letters*, 65(7), 1134-1136.

Wu, J., Wang, T. 2001. Ozonation of aqueous azo dye in a semi-batch reactor. *Water Research*, 35(4), 1093-1099.

Wu, W., Jiang, C., Roy, V.A. 2015. Recent progress in magnetic iron oxide–semiconductor composite nanomaterials as promising photocatalysts. *Nanoscale*, 7(1), 38-58.

Yang, S.-Y., Chen, Y.-X., Lou, L.-P., Wu, X.-N. 2005. Involvement of chloride anion in photocatalytic process. *Journal of Environmental Sciences*, 17(5), 761-765.

Yin, M., Li, Z., Kou, J., Zou, Z. 2009. Mechanism investigation of visible light-induced degradation in a heterogeneous TiO_2/Eosin Y/Rhodamine B system. *Environmental Science & Technology*, 43(21), 8361-8366.

Yuan, R., Ramjaun, S.N., Wang, Z., Liu, J. 2011. Effects of chloride ion on degradation of Acid Orange 7 by sulfate radical-based advanced oxidation process: Implications for formation of chlorinated aromatic compounds. *Journal of Hazardous Materials*, 196, 173-179.

Yuan, R., Ramjaun, S.N., Wang, Z., Liu, J. 2012. Photocatalytic degradation and chlorination of azo dye in saline wastewater: kinetics and AOX formation. *Chemical Engineering Journal*, 192, 171-178.

Yuranova, T., Laub, D., Kiwi, J. 2007. Synthesis, activity and characterization of textiles showing self-cleaning activity under daylight irradiation. *Catalysis Today*, 122(1), 109-117.

Zayani, G., Bousselmi, L., Mhenni, F., Ghrabi, A. 2009. Solar photocatalytic degradation of commercial textile azo dyes: Performance of pilot plant scale thin film fixed-bed reactor. *Desalination*, 246(1), 344-352.

Zeronian, S.H., Collins, M.J. 1989. Surface modification of polyester by alkaline treatments. *Textile Progress*, 20(2), 1-26.

Zhang, H., Wang, D., Huang, N. 1999. The effect of nitrogen ion implantation on tungsten surfaces. *Applied Surface Science*, 150(1), 34-38.

Zhang, X., Wang, Y., Li, G. 2005. Effect of operating parameters on microwave assisted photocatalytic degradation of azo dye X-3B with grain TiO_2 catalyst. *Journal of Molecular Catalysis A: Chemical*, 237(1), 199-205.

Zheng, Y., Chen, C., Zhan, Y., Lin, X., Zheng, Q., Wei, K., Zhu, J., Zhu, Y. 2007. Luminescence and photocatalytic activity of ZnO nanocrystals: correlation between structure and property. *Inorganic Chemistry*, 46(16), 6675-6682.

Zyoud, A., Zaatar, N., Saadeddin, I., Helal, M.H., Campet, G., Hakim, M., Park, D., Hilal, H.S. 2011. Alternative natural dyes in water purification: anthocyanin as TiO$_2$-sensitizer in methyl orange photo-degradation. *Solid State Sciences*, 13(6), 1268-1275.
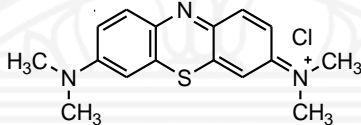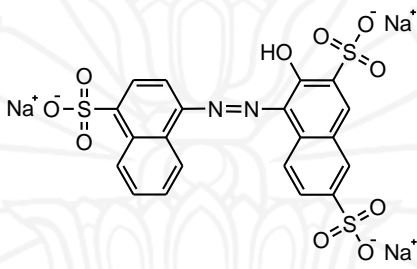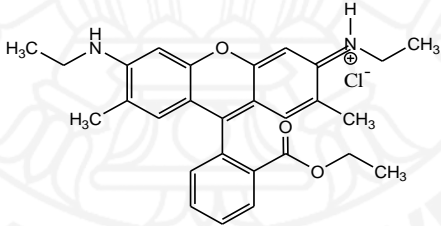
Appendices

Appendix A

Molecular structures of dyes

Table A1 Molecular structures of MB, AM, and R6G.

Dye	λ_{max} (nm)	Structure	Hydrogen bond donor	Hydrogen bond acceptor
Methylene blue	664		0	4
Amaranth	521		1	12
Rhodamine 6G	528		2	5

Appendix B

Calibration curves of dye solutions

Table B1 MB standard solution and absorbance at λ_{max} of 664 nm.

Standard No.	MB concentration (mg/L)	Absorbance
1	2	0.387
2	4	0.761
3	6	1.134
4	8	1.495
5	10	1.883
6	15	2.807
7	25	4.621
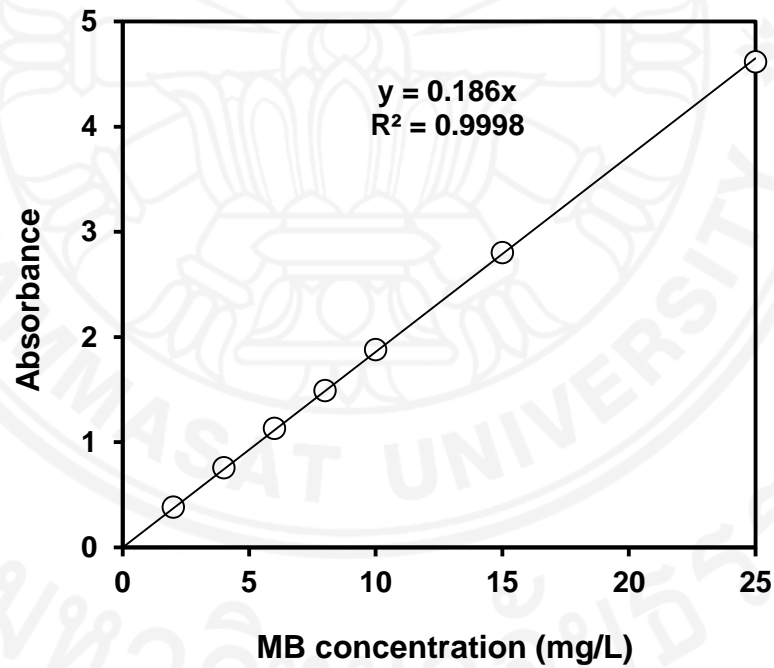
Figure B1 Calibration curve of MB (λ_{max} = 664 nm).

Table B2 AM standard solution and absorbance at λ_{max} of 521 nm.

Standard No.	AM concentration (mg/L)	Absorbance
1	2	0.073
2	4	0.163
3	6	0.228
4	8	0.295
5	10	0.381
6	15	0.573
7	25	0.955
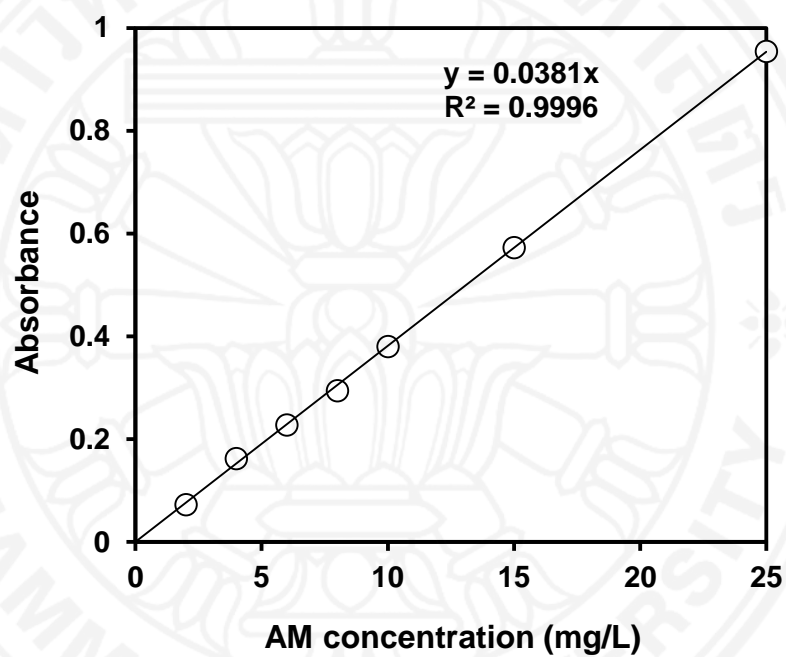
Figure B2 Calibration curve of AM (λ_{max} = 521 nm).

Table B3 R6G standard solution and absorbance at λ_{max} of 528 nm.

Standard No.	R6G concentration (mg/L)	Absorbance
1	2	0.223
2	4	0.516
3	6	0.749
4	8	1.025
5	10	1.255
6	15	1.855
7	25	3.171
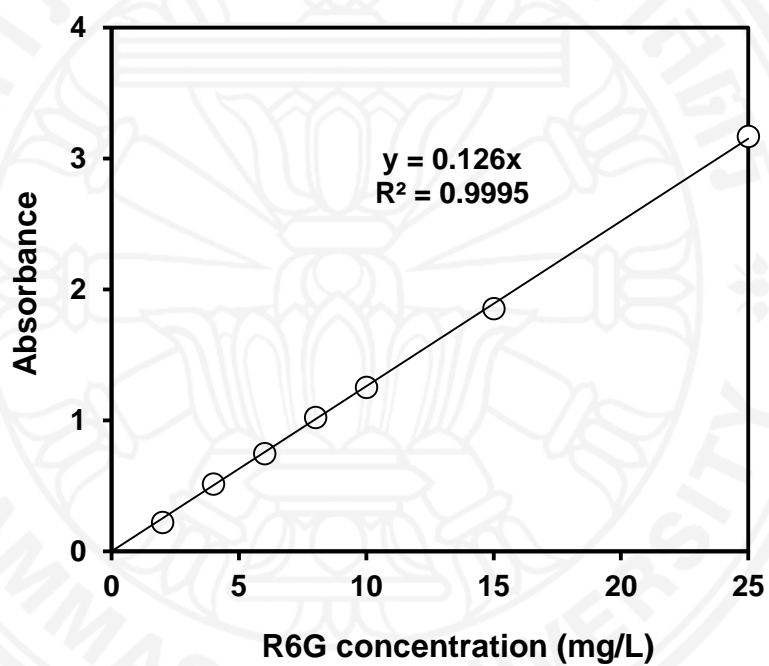
Figure B3 Calibration curve of R6G (λ_{max} = 528 nm).

Appendix C

Calibration curve of potassium nitrate solution

Table C1 KNO$_3$ standard solution.

Standard No.	TN standard (mg/L)	Area
1	0.1	6.81
2	0.2	14.76
3	0.5	35.36
4	1	73.49
5	2	145.85
6	5	353.90
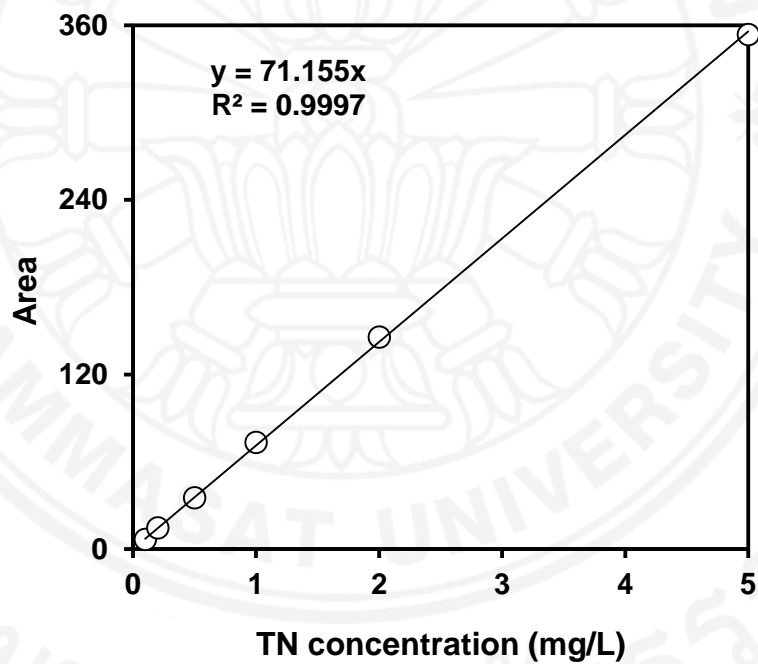
Figure C1 Calibration curve of KNO$_3$ solution.

Table C2 TN concentrations in the solutions after catalyst separation.

Sample		Area	TN (mg/L)
Milli-Q water		0.5518	0.00775
N-ZrO$_2$	Sample 1	0.5639	0.00792
	Sample 2	0.5625	0.00790
N-ZnO	Sample 1	0.5521	0.00776
	Sample 2	0.5575	0.00783
N-WO$_3$	Sample 1	0.5602	0.00787
	Sample 2	0.6057	0.00851
Milli-Q water		0.5584	0.00784

Appendix D

High-energy resolution N *K*-edge spectra of N$_2$
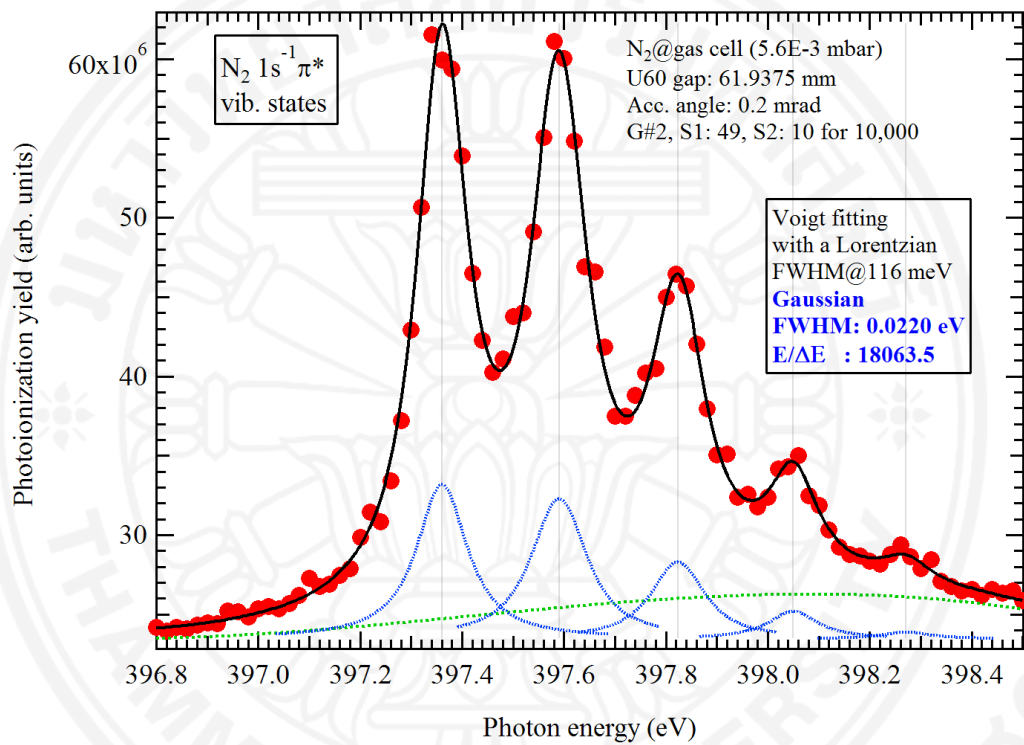
Figure D1 High-energy resolution N *K*-edge spectra recorded on N$_2$ gas at Beamline 3.2a of the Synchrotron Light Research Institute (Public Organization), Thailand (Nakajima et al., 2013).

Appendix E

Photolyses of dye solutions
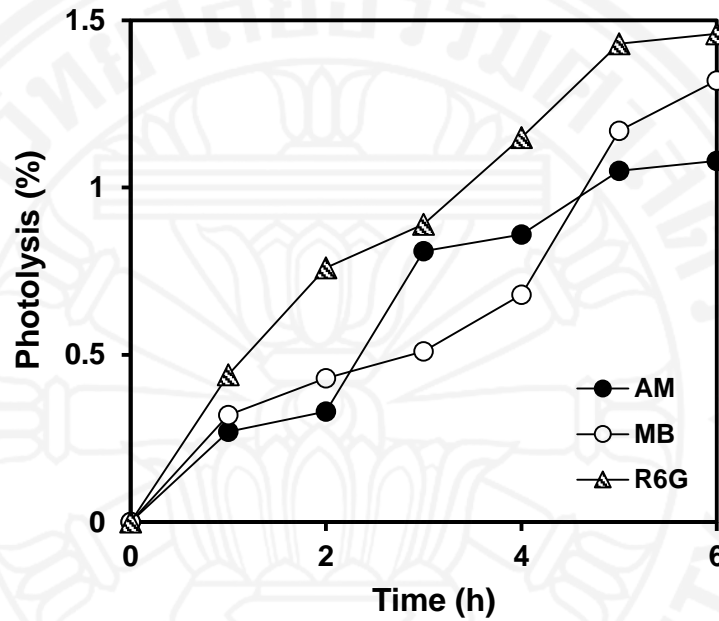
Figure E1 Photolysis of the dyes under visible light (C_0 = 10 mg/L, pH = 7, t = 6 h, I_{vis} = 16.5 W/m^2).
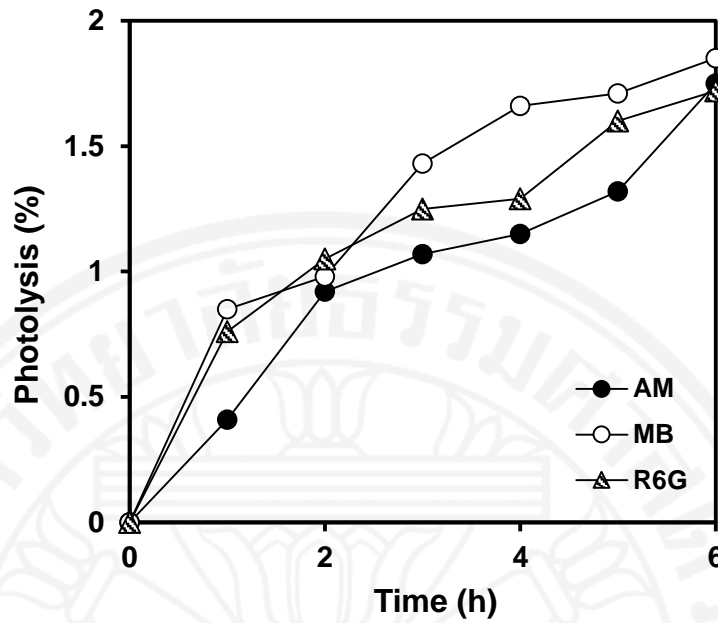
Figure E2 Photolysis of the dyes under visible light (C_0 = 10 mg/L, pH = 7, t = 6 h, I_{vis} = 144.7 W/m^2).
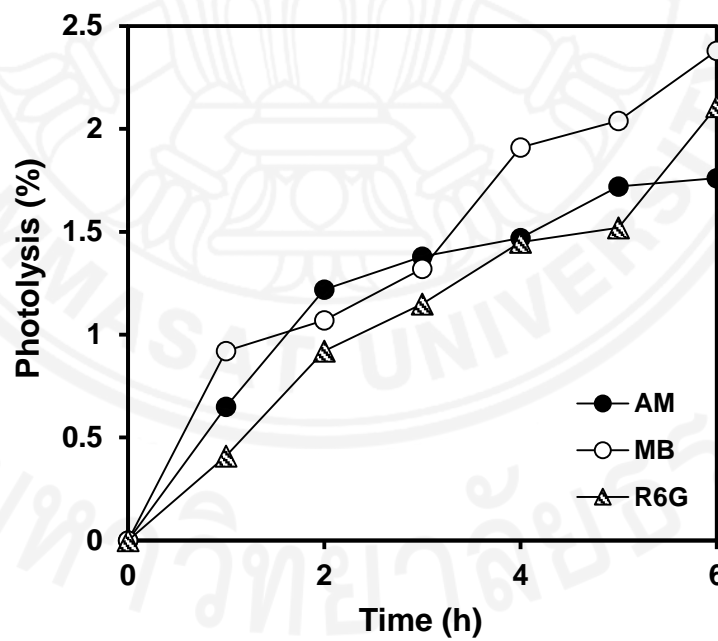
Figure E3 Photolysis of the dyes under UVC light (C_0 = 10 mg/L, pH = 7, t = 6 h, I_{UVC} = 3.5 W/m^2).
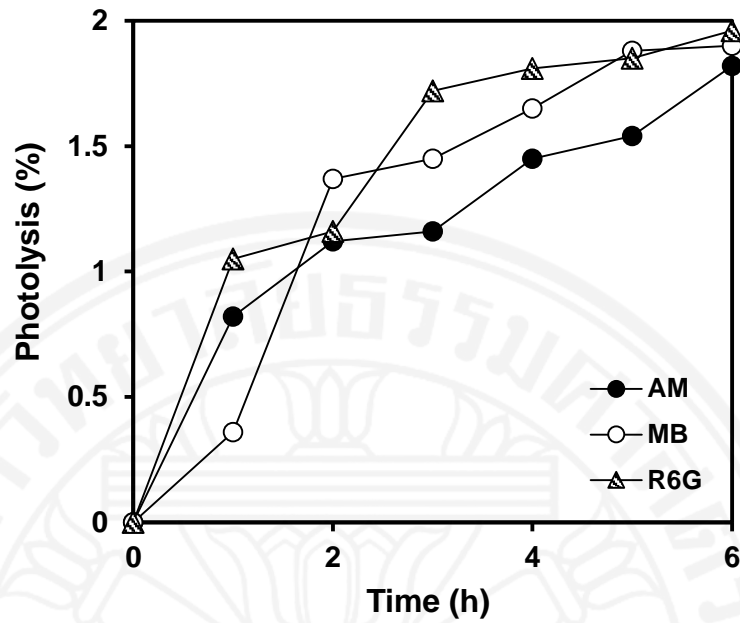
Figure E4 Photolysis of the dyes under UVA light (C_0 = 10 mg/L, pH = 7, t = 6 h, I_{UVA} = 3.5 W/m^2).
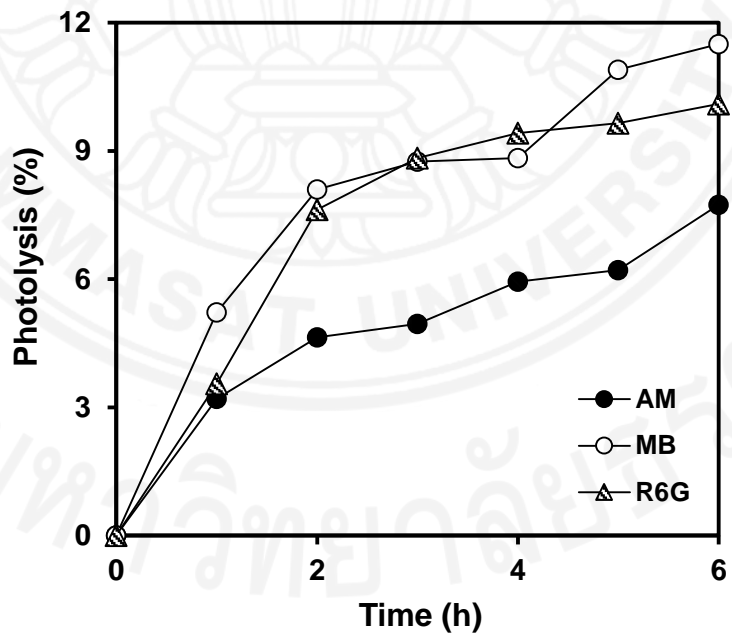
Figure E5 Photolysis of the dyes under solar light (C_0 = 10 mg/L, pH = 7, t = 6 h, I_{solar} = 601.2 W/m^2).